January 2013

Nano-Magnetic Devices for Computation

Dinuka Karunaratne
University of South Florida, dkkarunaratne@gmail.com

Nano-Magnetic Devices for Computation

by

D. K. Karunaratne

A dissertation submitted in partial fulfillment
of the requirements for the degree of
Doctor of Philosophy
Department of Electrical Engineering
College of Engineering
University of South Florida

Major Professor: Sanjukta Bhanja, Ph.D.
Sudeep Sarkar, Ph.D.
Paris H. Wiley, Ph.D.
Wilfrido A. Moreno, Ph.D.
Karthikeyan Lingasubramanian, Ph.D.

Date of Approval:
April 3, 2013

Keywords: Emerging devices, nanofabrication, multilayer, Boolean logic, energy minimization

Dedication

To my Family and Friends

Acknowledgments

I take this opportunity to express my profound appreciation to my Ph.D. supervisor Dr. Sanjukta Bhanja, who has guided, supported, suggested, encouraged and helped me in all my research. I am extremely thankful to her for patiently explaining and answering to all my questions.

My sincere thanks go to Dr. Sudeep Sarkar, Dr. Paris Wiley, Dr. Wilfrido Moreno, and Dr. Karthikeyan Lingasubramanian for serving in my committee. I would like to thank them all for their valuable support and advice and most importantly for taking the time to evaluate this work.

I would like to sincerely thank the Assistant Director of Nanotechnology Research and Education Center (NREC), Robert Tufts and his staff for their help. I would also like to acknowledge the National Science Foundation (NSF), whose financial support made this research possible.

Furthermore, I would like to thank all faculty members and administrative staff of the Department of Electrical Engineering and College of Engineering, USF. I would also like to especially thank Mr. Bernard Batson for his support.

Finally, I would like to thank all my fellow students in the Nano-Computing Research Group for their support.

Table of Contents

List of Tables

List of Figures

Abstract

The continuous scaling down of the metal-oxide-semiconductor field-effect transistor (MOSFET) has improved the performance of electronic appliances. Unfortunately, it has come to a stage where further scaling of the MOSFET is no longer possible due to the physical and the fabrication limitations. This has motivated researchers towards designing and fabricating novel devices that can replace MOSFET technology. Carbon Nanotube Field-Effect Transistors, Single Electron Tunneling Junctions, Nano-Magnetic Devices, and Spin Field-Effect Transistors are some prospective candidates that could replace MOSFET devices. In this dissertation, we have studied the computational performance of Nano−Magnetic Devices due to their attractive features such as room temperature operation, high density, robustness towards thermal noise, radiation hardened nature and low static power dissipation.

In this work, we have established that data can be propagated in a causal fashion from a driver cell to the driven cells. We have fabricated a ferromagnetic wire architecture and used a magnetic force microscopy (MFM) tip to provide localized magnetic inputs. This experiment validated two important phenomena; (1) a clocking field is essential to propagate data and (2) upon removal of the clocking field data can be propagated according to the input data.

Next, we have fabricated and captured MFM images of a nano-magnetic logic architecture that has computed the majority of seven binary variables. The architecture was designed by interconnecting three three-input majority logic gates with ferromagnetic and antiferromagnetic wire architectures. This seven input majority logic architecture can potentially implement eight different logic functions that could be configured in real-time. All eight functions could be configured by three control parameters in real-time (by writing logic one or zero to them).

Even though we observed error-free operations in nano-magnetic logic architectures, it became clear that we needed better control (write/read/clock) over individual single layer nano-magnetic devices for successful long-term operation. To address the write/clock/read problems, we designed and fabricated a multilayer nano-magnetic device. We fabricated and performed a set of experiments with patterned multilayer stacks of Co/Cu/$Ni_{80}Fe_{20}$ with a bottom layer having a perpendicular magnetization to realize neighbor interactions between adjacent top layers of devices. Based on the MFM images, we conclude that dipolar coupling between the top layers of the neighboring devices can be exploited to construct three-input majority logic gates, antiferromagnetic and ferromagnetic wire architectures.

Finally, we have experimentally demonstrated a magnetic system that could be used to solve quadratic optimization problems that arise in computer vision applications. We have harnessed the energy minimization nature of a magnetic system to directly solve a quadratic optimization process. We have fabricated a magnetic system corresponding to a real world image and have identified salient features with true positive rate more than 85%. These experimental results feature the potentiality of this unconventional computing method to develop a magnetic processor which solves such complex problems in few clock cycles.

Chapter 1: Introduction

1.1 Motivation

Technological advancements from the past couple of decades have revolutionized the life style of humans. Smartphones have brought information to our fingertips; advancements in gaming consoles have incorporated movements and gestures into the virtual world; advance safety features in automobiles have saved many human lives; global positioning systems have eased our transportation by giving us turn-by-turn directions. All of these innovations were made possible by the rapid evolution of the metal-oxide-semiconductor field-effect transistor (MOSFET).

Since their invention, MOSFETs have been scaled down in size to improve their performance [13, 83] and today their dimensions are in the nanometer range. Unfortunately further scaling of the MOSFET is no longer possible due to physical, material and thermal limitations [29]. Reducing the gate dielectric thickness has given rise to quantum tunneling and has caused unwanted leakage currents [109]. Shortening the gate length has caused high off-state leakage current between source and drain when the device is switched off [60]. Lowering the threshold voltage has made the device susceptible to noise and has reduced the reliability of the device [24]. In order to control short channel effects the doping concentration has been increased. Increasing dopant concentration introduces effects on carrier mobility and band to band tunneling ultimately causing a negative impact on the device performance [25]. It is a well-known fact that properties such as relative dielectric constant, carrier saturation velocity, carrier mobility, breakdown field strength and conductivity of a material change as the dimensions are scaled from micro to nanoranges [115]. It has come to the point where the materials used in MOSFETs have reached their physical limits and the device cannot produce the required characteristics for reliable performance. Furthermore, the power

dissipation in a MOSFET has not scaled down with the size, but rather has increased [79]. When the device is switched on, dynamic power is dissipated and when it is switched off, static power is dissipated resulting in wasteful heat energy generation. Due to these (and many more) drawbacks of MOSFETs, and to continue advancing technology, researchers and engineers are exploring novel devices and computing paradigms [7, 12, 26, 30, 39, 123, 124]. Carbon Nanotube Field-Effect Transistors (CNT-FETs), Nanowire Field-Effect Transistors (NW-FETs), Single Electron Tunneling Junctions (SETJs), Electrical Quantum-dot Cellular Automata (EQCA), Molecular Switches, Spin Field-Effect Transistors (SpinFETs) and Nano-Magnetic Devices are some prospective candidates to take over the functionality of MOSFETs.

A CNT-FET is a three terminal device similar to a MOSFET. The only difference is that the source and drain are connected with a carbon nanotube instead of the bulk substrate. Carbon nanotubes have the capability of traversing electrons from one end of the chanel to the other without encountering any scattering events [125]. This is known as ballistic transportation [34]. Carbon nanotubes also have a high thermal stability [107] and are capable of carrying a high current density [117]. These properties make a strong case for carbon nanotubes to be used as the channel between the source and drain in a field effect transistor [68, 120]. However, placing the carbon nanotube between the source and drain and controlling the chirality formation (metal or semiconductor) are a few challenging tasks with respect to fabricating CNT-FETs [31]. A NW-FET has a similar structure to a CNT-FET but utilizes a semiconductor nanowire instead of a carbon nanotube as for the channel. Semiconductor nanowires have similar properties to carbon nanotubes, thus making them an intuitive candidate to function as a channel between the source and drain in a field effect transistor [46, 80]. They also have the ability to be doped with a p-type or n-type material which allows for the assembly of p-type and n-type NW-FETs [38]. However, the inability to control size of a nanowire and to place the nanowire between the source and drain are a couple of the drawbacks with this device [31].

SETs have also been studied by many in [21, 28, 47, 49, 52, 53, 74, 92] as a replacement for MOSFETs. The working principle of a SET is the diffusion of a single electron through a barrier. The SET is constructed by sandwiching a thin insulator between two conductors. The two

conductors act as the source and drain. When an adequate amount of voltage is biased with the source terminal it is possible for the electrons in the source region to tunnel through the barrier layer and enter into the drain region. The prevention of additional electrons tunneling through is known as Coulomb blockade [36]. By allowing a single electron to tunnel through the barrier it is possible to switch on and off the device. Even though SETs consume less power and operate at fast speeds they are susceptible to noise. This makes the SET an unreliable device for long-term successful operation [124].

EQCA is another emerging computational device [57, 77, 89, 103]. These devices utilize electrostatic forces between electrons to process and propagate information. An EQCA is shaped like a square and has a quantum dot in each corner. In each EQCA cell there are two mobile electrons that can only traverse between the quantum dots within the cell. The two electrons in a cell will always arrange themselves to an energetically favorable configuration. Based on these configurations we can represent Boolean logic 1 and 0. If two EQCA cells are brought close enough for Coulombic interactions to take place between the electrons of different cells then it is possible to process information. Arranging EQCA cells in different formations allows the realization of different logic functions. EQCA shows a promise in ultralow power consumption, non-volatility and reconfigurability, but unfortunately it only functions properly in very low temperatures.

A molecular switch is another emerging device that can be used to realize Boolean logic [14, 32, 33, 91, 100]. Molecules that can be reversibly configured into two states by a change in the external environment are used for molecular switches. Based on the configuration of the molecule these devices will have a one-way flow of current [69, 100] or no flow at all. The key advantage of these devices is that they can be self-assembled. Unfortunately, interconnecting the molecules to electrodes is a challenging task.

SpinFETs are also three terminal devices similar to MOSFETs. Unlike in the MOSEFT, the source and drain in a SpinFET are made of ferromagnetic materials that have the same fixed magnetization. The electrons that are injected into the substrate (dilute magnetic semiconductor) by the source have definite spin direction. If the spin direction changes then the electron cannot enter the drain. The spin direction of the electron can be changed by the gate voltage induced

magnetic field. Based on the spin directions of the electrons a current will flow through the device switching it on or otherwise switching it off [23, 106]. These devices have low power consumption, good noise margins and operate at high speeds. Unfortunately, it has become a challenging task to inject electrons with a unidirectional spin into the substrate.

Nano-magnetic devices have also harnessed the spin property of an electron to compute data [6, 11, 17, 18, 76, 88]. The fundamental computing element of a nano-magnetic device is a single domain magnet with dimensions in the nano regime. These devices process data through magnetic field interactions with their nearest neighbors and they store data in their magnetization states. Based on the arrangement of the nano-magnetic devices it is possible to implement complex computation [40, 78, 87, 111]. Nano-magnetic devices have many attractive features. Nano-magnetic devices operate in room temperature, unlike other devices which operate in very low temperatures. These devices require very low static power, which reduces the power consumption and increases the on time of the appliance. Since these devices can be scaled to small dimensions, the device density increases and the size and weight of the electronic appliance decreases. Radiation hardness is another major advantage of nano-magnetic devices over other emerging devices. Reliable computation under the influence of radiation (extreme environments) is very important for satellites and other space equipment. Nano-magnetic devices are also robust towards thermal noise. Many emerging devices are hard to fabricate but nano-magnetic devices are defect tolerant and can be easily fabricated with a lithography process. Due to these and many other promising features, we have focused the research in this dissertation towards the development of nano-magnetic devices as a long-term successful computational element.

Cowburn *et al.* [17] were the first to demonstrate the propagation of information along magnetic wire in room temperature. They used a clock scheme to propagate a magnetic soliton. A soliton occurs when two closely placed single domain magnets have anti-parallel magnetization, and moves along the array through a sequential magnetization reversal. The single domain magnets used in this experiment were cylindrical and had no shape anisotropy. Bernstein *et al.* [6] experimented with single domain magnets that were fabricated into a rectangular prism shape. This introduced shape anisotropy and was able to enumerate logic 0 and logic 1 along the magnetic easy axis.

Bernstein *et al.* [6] reported a perfect antiferromagnetic ordering along a 64 magnet-long chain. The first functioning magnetic majority gate was demonstrated by Imre *et al.* [40]. They presented magnetic force microscopy (MFM) images of all possible combinations of majority logic. Alam *et al.* [3] demonstrated an on-chip clocking system, which changes the magnetic moment of a magnet when 680 *mA* of current is passed through the copper wire which the magnets were fabricated on. Varga *et al.* [111] demonstrated the ability of a fan-out signal in nano-magnetic logic architectures and Pulecio *et al.* [87] demonstrated a coplanar crosswire system which has the ability to transfer data over an intersection without any data loss.

1.2 Contribution

In this research we have explored the viability of using nano-magnetic devices as computational elements. Even though nano-magnetic devices have major advantages over other emerging devices there are a few shortcomings which need to be addressed. Writing data on to the input device, clocking the devices at the correct sequence and reading data from the output device are a few issues that we have addressed. The contributions of the dissertation are:

- The first contribution was to establish that data can be propagated in a causal fashion from a driver cell to the driven cells. We experimented with a ferromagnetic wire having a pair of nano-magnetic devices which were 20 *nm* apart. We used a MFM tip, resulting in an 8 *mT* field, to switch the magnetization of one of the nano-magnetic devices. Even though the individual magnet switched its magnetization, the neighbor remained unchanged. This experimentally validates the observation made by Csaba *et al.* [18] that a clocking field is necessary for the neighbor interaction. Finally, we used a DC electromagnet with a field of 45 *mT*, to provide an out-of-plane clocking field. We observed two important phenomena; (1) the input field was reduced up to 2.5 *mT* to reverse the magnetization and (2) upon removal the hard axis field, the neighbor nano-magnetic device reversed its magnetization according to the input.

- The second contribution was to fabricate and capture MFM images of a nano-magnetic logic architecture that computed the majority of seven Boolean variables. The architecture has ferromagnetic and antiferromagnetic wires to propagate data and three three-input majority logic gates to process data. This seven input majority logic architecture can potentially implement eight different logic functions that could be configured in real-time. All eight functions could be configured by three control parameters in real-time (by writing logic one or zero in them). To this date this is the largest nano-magnetic logic architecture fabricated and has been reported with no magnetic frustrations.

- Even though we observed error-free operations in single layer nano-magnetic logic architectures, it became clear that we needed better control (write/read/clock) over individual single layer nano-magnetic devices in the system for successful long-term operation. To address this we moved from single layer nano-magnetic devices to multilayer nano-magnetic devices. The third contribution was to fabricate and perform a set of experiments with a multilayer stack of $Co_{\ t=0.4nm}/Cu_{\ t=4nm}/Ni_{80}Fe_{20\ t=5nm}$ with a perpendicular magnetic anisotropy bottom layer to realize neighbor interactions between adjacent free top layers of devices. Based on the MFM images we conclude that dipolar coupling between the free layers of the neighboring devices can be exploited to construct local elements like three-input majority logic gates, inverters and interconnects.

- The final contribution of this dissertation was to harness the energy minimization nature of a magnetic system to solve a quadratic optimization problem, especially those arising in computer vision applications. We have fabricated a magnetic system corresponding to an image and have identified the salient features in the image with a true positive rate of more than 85%. These experimental results display the potentiality of this unconventional computing method to develop a magnetic processor which can solve such complex problems in few clock cycles.

1.3 Outline of the Dissertation

The outline of this dissertation is as follows:

- Chapter 2 provides a summary of magnetic materials and magnetism at nanoscale.
- Chapter 3 provides the fabrication and characterization methodology of nano-magnetic devices.
- Chapter 4 shows the experimental demonstration of data propagation in a ferromagnetic wire architecture.
- Chapter 5 shows the design, fabrication and experimental observation of seven-input majority logic architecture.
- Chapter 6 shows a multilayer nano-magnetic device that can address the write, clock and read problems in this technology.
- Chapter 7 provides an experimental demonstration of harnessing the energy minimization nature of magnetic systems to solve complex quadratic optimization problems that arise in computer vision applications.
- Chapter 8 provides the conclusion of this dissertation.

Chapter 2: Magnetic Materials and Magnetism

This may sound surprising, but all matter possesses magnetic properties. The most appropriate way to categorize magnetic properties of materials is by comparing their magnetic response in the presence of an external magnetic field. The properties of a magnetic structure are also affected at different length scales. The magnetic properties at macroscale are quite different from that of the nanoscale. In this chapter we discuss a summary of each magnetic class and magnetism at the nanoscale.

2.1 Classes of Magnetic Material

The electron is an elementary particle that holds an orbital motion around a nucleus and a spin motion around its own axis. These rotational motions of an electron and how electrons interact with one another are the primary cause for magnetism in all materials. However, magnetic properties change from one material to another due to the collective behavior of atoms.

Materials are classified into five classes of magnetic materials according to their magnetic response in the presence of an external magnetic field. Experiments have demonstrated that when a material is placed in the presence of an external magnetic field it experiences a magnetic moment. If the external magnetic field is represented by a vector $\boldsymbol{H}$ and the magnetization (magnetic moment per unit volume) is represented with the vector $\boldsymbol{M}$, then for most materials the relation between these two vectors is expressed as:

$$\boldsymbol{M} = \chi \boldsymbol{H} \tag{2.1}$$

where χ is the magnetic susceptibility of a material [4, 105]. If the magnetic induction is denoted by the vector $\boldsymbol{B}$ then Maxwells equation in International System (SI) of units is expressed as:

$$\boldsymbol{B} = \mu_0(\boldsymbol{H} + \boldsymbol{M}) \tag{2.2}$$

$$\boldsymbol{B} = \mu \boldsymbol{H} \tag{2.3}$$

where

$$\mu = \mu_0(1 + \chi) \tag{2.4}$$

and μ is the magnetic permeability [4, 105].

Materials that fit to the relation in Eqn. 2.1 are categorized into two classes. They are diamagnetic materials and paramagnetic materials. Diamagnetic materials have no net magnetization in the absence of an external magnetic field and have a negative magnetic susceptibility. Paramagnetic materials also have no net magnetization in the absence of an external magnetic field but they have a positive magnetic susceptibility. Materials that do not fit to the relation in Eqn. 2.1 are categorized into three classes. They are ferromagnetic materials, ferrimagnetic materials and antiferromagnetic material. These materials have a more complicated relation between magnetization and applied field. In fact the magnetization is dependent on the history of the applied magnetic field. Materials that fall in the ferromagnetic class have a net magnetization and a positive magnetization in the absence and presence of an external magnetic field, respectively. Ferrimagnetic materials have antiparallel magnetization in the sublattices with dissimilar magnitudes causing a small net magnetization in the absence of an external magnetic field and a positive magnetization in the presence of an external magnetic field. The materials that have antiparallel and similar magnitudes of magnetization in the sublattices fall in the antiferromagnetic class.

2.1.1 Diamagnetism

The phenomenon of having a magnetization in the opposite direction to an applied external magnetic field caused by the material is known as diamagnetism. This effect is seen in all materials but the ones that do not have any other magnetic behavior are categorized as diamagnetic materials. Diamagnetism occurs in materials that have atomic or molecular orbitals that are either filled or empty [104]. Noble gasses, water, calcite and quartz are examples of diamagnetic materials. Diamagnetic materials possess zero magnetization in the absence of an external magnetic field. The other magnetic property of diamagnetic materials is that their magnetic susceptibility is temperature independent and has a negative value causing then an opposing magnetization to the applied external magnetic field.

2.1.2 Paramagnetism

The phenomenon of having a magnetization in the same direction as to the applied external magnetic field caused by the material is known as paramagnetism. These materials are known as paramagnetic materials. In paramagnetic materials the individual magnetic moments have a non-zero value because of the unpaired electrons in the partially filled orbitals. However, these moments are weakly coupled with each other and thermal energy causes them to randomly align. This results in a zero net magnetization in the absence of an external magnetic field [104]. In the presence of an external magnetic field the magnetic moments align with the applied external magnetic field causing a net magnetization. In paramagnetic materials the magnetic susceptibility takes a positive value and is inversely proportional to the temperature. Montmorillonite, Nontronite, Biotite and Siderite are a few paramagnetic materials.

2.1.3 Ferromagnetism

The phenomenon of having a non-zero net magnetization in the absence of an external magnetic field is known as ferromagnetism. These materials are known as ferromagnetic materials. Ferromagnetic materials have 3d orbitals that are unfilled with electrons causing strong non-zero magnetic moments. These magnetic moments are strongly coupled with their neighbors causing a magnetic remanence or a spontaneous magnetization [104]. The strong coupling forces, known as exchange forces, extend to certain nanoscale distances and results in domain-like structures in the material. Ferromagnetic materials are also temperature dependent. If the temperature is increased such that the exchange forces are overcome by thermal energy, then the alignment of the magnetic moments would become random and cause a zero net magnetization. This temperature is called the Curie temperature. Ferromagnetic materials have another unique property. They have the ability to retain information of an applied external magnetic field. This behavior is called as hysteresis and has made the relation between magnetization and applied external magnetic field complicated. Cobalt, Iron and Permalloy are a few ferromagnetic materials. Researchers and engineers have taken advantage of the magnetic properties in ferromagnetic materials to construct electronic devices which store and compute information.

2.1.4 Ferrimagnetism

The phenomenon of ferrimagnetism arises in materials that have sublattices with an antiparallel alignment and dissimilar magnetic moments causing a net magnetization in the absence of an external magnetic field. This occurs because of dissimilar atoms or ions in the materials causing superexchange interactions between sublattices [104]. Materials with ferrimagnetic properties are known as ferrimagnetic materials. Similar to ferromagnetic materials, these materials also have remanence, hysteresis and a curie temperature. Magnetite and Barium Ferrite are a couple examples of ferrimagnetic materials.

2.1.5 Antiferromagnetism

Anitferromagnetism can be seen in materials that have sublattices with an antiparallel alignment and equal magnetic moments causing a zero net magnetization. Materials that demonstrate antiferromagnetism are known as antiferromagnetic materials. When the temperature of an antiferromagnetic material is increased above the Neel temperature, antiferromagnetism vanishes and the material behaves as paramagnetic material [104]. Hamatite, Chromium and Iron Manganese are a few antiferromagnetic materials.

2.2 Magnetism at the Nanoscale

Magnetism is a property of all materials that arises from the angular motion of the electrons in the material. The angular momentum of an electron is a combination of its intrinsic angular momentum, or spin and orbital angular momentum. In quantum mechanics the intrinsic angular momentum and the orbital angular momentum are defined with quantum numbers $\langle s \rangle$ and $\langle l \rangle$, respectively. The quantum number for the spin magnetic moment is expressed as:

$$\langle m_s \rangle = -g_s \frac{\mu_B}{\hbar} \langle s \rangle \tag{2.5}$$

$$\hbar = \frac{h}{2\pi} \tag{2.6}$$

where h is the Planck constant, μ_B is the Bohr magnetron and g_s is the Lande g-factor for the spin moment [4, 105]. The quantum number for the orbital magnetic moment is expressed as:

$$\langle m_o \rangle = -g_l \frac{\mu_B}{\hbar} \langle l \rangle \tag{2.7}$$

$$\bar{h} = \frac{h}{2\pi} \tag{2.8}$$

where h is the Planck constant, μ_B is the Bohr magnetron and g_l is the Lande g-factor for the orbital moment [4, 105]. The quantum number for the total magnetic moment is the addition of the spin magnetic moment and the orbital magnetic moment. It is expressed as:

$$\langle m_{total} \rangle = -\frac{\mu_B}{\bar{h}}(g_s \langle s \rangle + g_l \langle l \rangle) \tag{2.9}$$

In a material where there is a collection of electrons, the individual magnetic moments of the electrons would interact with each other to minimize the total magnetic energy in the material. Similarly in the presence of an applied external field the magnetic moments would interact to minimize the total energy in the system. In the remaining part of this section, we will discuss the different energies that contribute to the total magnetic energy in a material and the magnetic dynamics to reduce the magnetic energy.

2.2.1 Exchange Energy

Exchange energy arises due to the magnetic coupling, or the exchange interaction between the nearest neighboring magnetic moments. Exchange interaction is only seen in ferromagnetic, ferrimagnetic and antiferromagnetic materials. This is not seen in diamagnetic or paramagnetic materials. In ferromagnetic materials the exchange interaction takes a positive value causing the magnetic moments to align in a parallel configuration. In ferrimagnetic and antiferromagnetic materials the exchange interaction takes a negative value causing the magnetic moments to align in an antiparallel configuration. The exchange energy is proportional to the dot product between two magnetic moments and is expressed as:

$$E_{ex} = -J_{ex}\mathbf{m_i} \cdot \mathbf{m_j} \tag{2.10}$$

where J_{es} is the exchange interaction which is dependent of the temperature and the distance between the magnetic moments. $\mathbf{m_i}$ and $\mathbf{m_j}$ are the magnetic moments of two nearest neighbors. The magnetic moments would try to align with each other to minimize exchange energy.

2.2.2 Zeeman Energy

Zeeman energy arises when a magnetic moment is affected with an external magnetic field. The Zeeman energy is proportional to the dot product between the external magnetic field and the magnetic moment and is expressed as:

$$E_{Zeeman} = -\mathbf{m} \cdot \mathbf{H_{ext}} \tag{2.11}$$

where $\mathbf{m}$ is the magnetic moment and $\mathbf{H_{ext}}$ is the external magnetic field. When a magnetic moment experienceâĂŹs an external magnetic field it will try to align itself with the external magnetic field in order to minimize the Zeeman energy.

2.2.3 Magnetostatic Energy

Magnetostatic energy arises due to the interaction of the material with itself. Basically, a magnetic field is created inside the material opposing the magnetic field created by magnetic moments. This magnetic field is known as the demagnetizing field. The magentostatic energy is the volume integral of the dot product between a magnetic moment and the demagnetizing field and is expressed as:

$$E_{ms} = -\frac{1}{2}\int_V \mathbf{m} \cdot \mathbf{H_d}\, dV \tag{2.12}$$

where $\mathbf{m}$ is the magnetic moment, $\mathbf{H_d}$ is the demagnetizing field and V is the volume of the material.

2.2.4 Anisotropy Energy

The dependence of magnetization on the direction in which it is measured is known as magnetic anisotropy. The magnetic anisotropy of a material is dependent on the crystalline structure, shape, surface, growth procedure and strain. Based on sources of anisotropies in a material the magnetization would ease to a direction to minimize the magnetic energy. This axis is known as the easy axis. The anisotropy energy (E_{ae}) is a result of magnetic anisotropy.

2.2.5 Dynamics of Magnetization

The magnetization direction of a magnet would ease in such a way as to minimize the total magnetic energy in the system. The total magnetic energy is the summation of the exchange, Zeeman, magnetostatic and anisotropy energies. To understand how the magnetization would reach a position that would minimize the total magnetic energy, we need to look into the magnetization dynamics. The magnetization dynamics are described by Landau-Lifshitz-Gilbert equation and it is expressed as:

$$\frac{d\mathbf{M}}{dt} = \frac{-\gamma}{1+\alpha}(\mathbf{M}\times\mathbf{H_{eff}}) - \frac{\alpha\gamma}{M_s(1+\alpha^2)}[\mathbf{M}\times(\mathbf{M}\times\mathbf{H_{eff}})] \tag{2.13}$$

where $\mathbf{M}$ is the magnetization and $\mathbf{H_{eff}}$ is the effective magnetic field. α is the intrinsic damping constant and γ is the gyromagnetic ratio. The first term in Eqn. 2.13 causes the magnetization to precess around the effective field. The second term in Eqn. 2.13 force the magnetization to move towards the effective field. The effective field is derived from the total magnetic energy and is expressed as:

$$\mathbf{H_{eff}} = -\frac{1}{\mu_0}\frac{dE_{total}}{d\mathbf{M}} \tag{2.14}$$

where μ_0 is the magnetic permeability and E_{total} is the total magnetic energy. The total magnetic energy is the summation of all the different magnetic energies in a material.

$$E_{total} = E_{ex} + E_{Zeeman} + E_{ms} + E_{ae} \tag{2.15}$$

where E_{ex} is the exchange energy, E_{Zeeman} is the Zeeman energy, E_{ms} is the magnetostatic energy and E_{as} is the anisotropic energy.

Chapter 3: Fabrication and Characterization of Nano-Magnetic Devices

To fabricate nano-magnetic devices we have used an electron beam lithography process to pattern the devices, an electron beam evaporation process to deposit the soft ferromagnetic material and a liftoff process to remove the unwanted material. To identify defect free nano-magnetic devices we used a scanning electron microscope (SEM) and a scanning probe microscope in the atomic force microscope (AFM) mode for topological characterization. Once the defect free nano-magnetic devices were identified we used a scanning probe microscope in the magnetic force microscope (MFM) mode to take qualitative magnetic measurements.

3.1 Background

To address today′s sophisticated markets needs for better electronic appliances engineers and researchers have continuously miniaturized the metal-oxide-semiconductor field-effect transistor (MOSFET) transistor for better energy efficiency, higher speed, more reliability and lower the cost. Unfortunately it has reached its physical limitations and further miniaturizing is not possible. To overcome this problem researchers are looking into novel computing devices that could augment the existing MOSFET technology. Carbon Nanotube Field-Effect Transistors, Single Electron Tunneling Junctions, Nano-Magnetic Devices, and Spin Field-Effect Transistor are some prospective candidates to replace MOSFET devices. Due to the nonvolatile nature, low static power dissipation, radiation hardness and room temperature operation, nano-magnetic devices have high potential to replace or coexist with existing MOSFET technology.

Nano-magnetic device come in many shapes [41]. Cowburn *et al.* [17] have worked with circular nano-magnetic devices, Bernstein *et al.* [6] have worked with rectangular nano-magnetic devices and Lambson *et al.* [54] have worked with elliptical nano-magnetic device. The fabrication method of all these nano-magnetic devices is the same. In this dissertation we have worked with rectangular and circular nano-magnetic devices.

Rectangular nano-magnetic devices are magnets that have been shape engineered into rectangular prisms which have dimensions of 100 *nm* x 50 *nm* x 10 *nm* that exhibit a single magnetic domain. These devices preserve Boolean information in their two dominant magnetization states and compute information through magnetic field-coupled interactions with its nearest neighbors. For adequate magnetic field-coupling with its neighbors, these devices need to be placed close to each other such that the spacing between two devices should not be more than 20 *nm*. Due to the size of these nano-magnetic devices and their special arrangement it is not possible to use conventional optical lithography techniques [42, 67] to fabricate these devices. It is possible to pattern and fabricate nano structures with other alternative methods such as X-ray lithography [35], ion beam lithography [116] and electron beam lithography [112] which do not have the diffraction constrains as optical lithography. To pattern the nano-magnetic devices in this dissertation we have used the electron beam lithography method. Electron beam lithography has many advantages over the other methods. As the name implies it uses a focused beam of electrons as the exposure source and since electrons have a much smaller wavelength than photons it is possible to perform high resolution lithography. Another advantage is the large depth of focus.

To fabricate the nano-magnetic devices we have used a bottom up approach. To design the nano-magnetic devices and to configure their special arrangements (patterns), we have used a computer-aided design (CAD) software. As for the substrate we have used an n-type $<100>$ Silicon wafer primarily due to its lack of magnetic response and extremely smooth surface which facilitates uniform growth of magnetic thin films. To transfer the patterns of the nano-magnetic devices via electron beam lithography, we have coated the wafer with an electron sensitive resist. Electron sensitive resist can be categorized in to two main categories, which are positive resist and negative resist. Due to the nature of the pattern of the nano-magnetic devices we have used a positive

resist. There are many positive tone electron beam resists available commercially. We have used poly(methyl methacrylate) (PMMA) since it has good adhesion with the substrate surface, ultra-high resolution, high contrast, low swelling during development and gives reproducible results [121]. The PMMA we used has a molecular weight of 950000 $g/gmol$. To achieve the desired low thickness, PMMA was mixed with Anisole. When PMMA is exposed to an electron beam the electrons generate adequate energy to dissociate the C-C bonds resulting with lower molecular weight segments from the original polymer [72]. These lower molecular weight compounds dissolve more easily in the developer solvents than the unexposed PMMA. We have used Methyl Isobutyl Ketone (MIBK) and Isopropanol (IPA) with 3 to 1 ratio as the developer solvent to obtain best selectivity [122] among the exposed and unexposed PMMA. The nano-magnetic devices were made of soft ferromagnetic material to enable easy switching between the two stable magnetization states. The soft ferromagnetic material we have used is Permalloy. Permalloy is a magnetic alloy made of Nickel and Iron ($Ni_{80}Fe_{20}$). A Thin layer of ferromagnetic films can be deposited by chemical or physical vapor deposition methods. To deposit Pemalloy on the substrate we have used electron beam evaporation, which is a physical vapor deposition method. Electron beam evaporation facilitates line of sight deposition which assists in the final liftoff process to remove the unwanted material and also preserves the stoichiometry of Permolloy [55]. The final step of fabricating the nano-magnetic devices involves a liftoff process which selectively removes the unwanted material from the substrate. To selectively remove the unexposed PMMA and preserve the Permalloy thin film on the Silicon wafer surface we dipped the sample in an Acetone bath. To enhance the liftoff process the Acetone bath was heated and assisted with an ultrasonic agitation.

Fabrication of nano-magnetic devices comprises of six main steps. Fig. 3.1 shows brief flow diagram of the fabrication process. In the proceeding section a detail description of each fabrication step involved in fabricating nano-magnetic devices are given. To characterize the nano-magnetic device we have used a SEM and scanning probe microscope in the AFM mode. To observe magnetization states of the nano-magnetic devices we have used a scanning probe microscope in the MFM mode. A detailed description of the characterization is given in section 3.3.

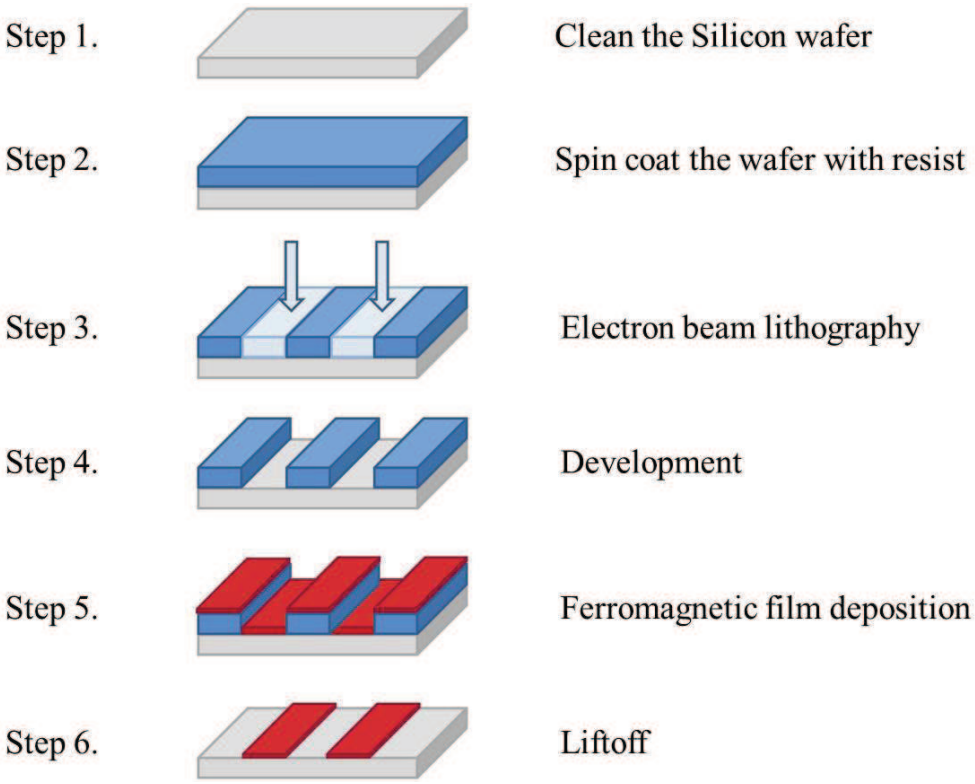

Figure 3.1: A flow diagram to fabricate single layer nano-magnetic devices.

3.2 Fabrication Process

Fabrication of nano-magnetic devices involves six steps. The flow diagram in Fig. 3.1 shows the fabrication steps. As for the substrate we have used an n-type, <100>, 2 inch Silicon wafer. The first step involves cleaning the Silicon wafer. To clean the Silicon wafer we have used a standard RCA cleaning procedure. The second step involves spin coating the Silicon wafer with PMMA. Exposing the Silicon wafer with an electron beam to produce the desired patterns is the third step. Once the exposure is completed the next step is to develop the sample in a developer solution. In the fifth step a uniform layer of Permalloy was evaporated on to the Silicon wafer. The final step involves the liftoff procedure to remove the unwanted material from the Silicon wafer leaving the nano-magnetic logic devices. A detail description of each fabrication step is described next in this section.

3.2.1 Step 1. Substrate Cleaning Procedure

To clean the Silicon wafer we have used a standard RCA cleaning procedure. The RCA cleaning procedure removes all organic, ionic, oxide and heavy metal contaminants from the surface of the Silicon wafer. The procedure has three cleaning solutions. The first solution contains Ammonium Hydroxide, Hydrogen Peroxide and water. This solution removes all organic contamination from the surface. The second solution was a Hydrogen Fluoride solution which removes metallic contamination and oxide from the surface. The final solution was a mixture of Hydrochloric acid, Hydrogen Peroxide and water. This removes all ionic and heavy metal contamination from the surface. In between each solution the wafer was dipped in deionized water to remove any residues from the previous solution. Finally the wafer was dried with Nitrogen gas. A detail description of each step in the RCA cleaning procedure is described in Table. 3.1.

Table 3.1: RCA cleaning procedure.

Step	Process	Description
1	Rinse wafer with Deionizer water.	Rinses off any superficial particles.
2	Dip in NH_4OH : H_2O_2 : H_2O (1:1:5) (SC1) at 60^oC for 10 minutes.	Removes insoluble organic contaminants.
3	Rinse wafer with deionizer water.	Rinses off any residue.
4	Dip in HF (50:1) for 20 seconds.	Removes native oxide layers.
5	Rinse the wafer with deionizer water.	Rinses off any residue.
6	Dip in HCl : H_2O_2 : H_2O (1:1:6) (SC1) at 60^oC for 10 minutes.	Removes ionic and heavy metal contaminants.
7	Rinse wafer with deionizer water.	Rinses off any residue.
8	Dry with Nitrogen Gas.	Removes moisture off the wafer.

3.2.2 Step 2. Resist Coating Procedure

Spin coating the Silicon wafer with PMMA is a key step in the fabrication procedure. The thickness of the PMMA is crucial for the liftoff procedure. As a rule of thumb, the thickness of the PMMA should be more than three times the thickness of the nano-magnetic device. Since the nano-magnetic devices have a thickness of about 10 *nm* we anticipated the thickness of PMMA to be about 30 *nm* - 40 *nm*. To achieve this thickness PMMA was dissolved in Anisole prior to spin coating on the Silicon wafer. To spin coat the PMMA we have used a Laurell Technologies WS-400A-8NPP/Lite Spin Processor. Once the resist was spun over the silicon wafer, the Silicon wafer was soft baked in a furnace at 170^oC for 30 minutes to remove any excess solvents. The procedure used for PMMA coating is given in Table. 3.2.

Table 3.2: Resist coating procedure.

Step	Process & Description
1	Place wafer on the spinner and a drop of PMMA/Anisole on the wafer.
2	Pre-ramp up: 0 - 500 rpm in 5 seconds.
3	Ramp up: 500 - 6000 rpm in 10 seconds.
4	Spin: 6000 rpm for 45 seconds.
5	Ramp down: 6000 - 0 rpm in 15 seconds.
6	Soft bake: 170^{o}C for 30 minutes to remove solvent.

3.2.3 Step 3. Electron Beam Lithography Procedure

To pattern the nano-magnetic devices on the resist we have used an electron beam lithography technique to achieve high resolution lithography. To expose the resist to an electron beam we used a Hitachi SU-70 scanning electron microscope that was retrofitted with a Nanometer Pattern Generation System (NPGS) by JC Nabity Lithography Systems. The pattern of the nano-magnetic devices was designed on DesignCAD 2000 NT and was saved in a format recognized by NPGS. Once the patterns were designed and the Silicon wafer coated with PMMA was mounted in the SEM chamber, the SEM was operated at 30 *kV* and the electron beam was aligned, stigmatized and focused to achieve the optimum resolution. The optimum condition for writing the pattern was determined by growing contamination spots on the PMMA resist prior to patterning the nano-magnetic logic devices. Such a spot with a diameter of 20 *nm* is shown in the SEM image in Fig 3.2. Once the optimum conditions were reached the patterns were written on the resist. A detail description of the electron beam lithography procedure is given in Table. 3.3.

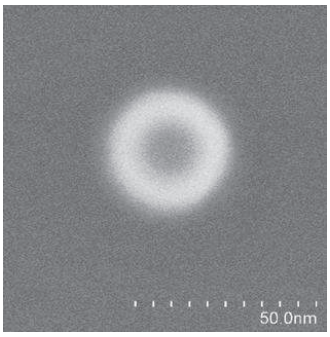

Figure 3.2: SEM image of a contamination spot grown by an optimized electron beam.

Table 3.3: The electron beam lithography procedure.

Step	Process & Description
1	Mark a specific location on the sample and insert it into the SEM chamber
2	Operating voltage 30 kV, working distance $<$5mm, optimize condenser lens, objective and anode aperture values.
3	Focus and stigmate the beam, align the apertures and increase the magnification until magnification is x800000 and measure beam current.
4	Insert electron-beam current, dose, line spacing and center to center distance values to the NPGS system.
5	Run the CAD pattern of the nano-magnetic devices in the unexposed resist area.
6	Shutdown the system and remove sample from the SEM chamber.

3.2.4 Step 4. Development Procedure

The objective in this procedure was to remove the exposed PMMA from the Silicon wafer. The difference between the exposed and unexposed PMMA is the molecular weight of the polymer. The exposed PMMA has lower molecular weight while the unexposed has higher molecular weight. The developer solvent dissolves the polymer with the lower molecular weight. We have used a mixture of

MIBK and IPA with a 3 to 1 ratio as the developer solution. The sample was dipped in the developer solution for 60 seconds to dissolve the exposed PMMA. We have optimized the concentration and the duration of the procedure to attain perfect exclusion of the exposed PMMA leaving the unexposed PMMA on the Silicon wafer. Once the sample is taken out from the developer solution, it was rinsed with IPA and dried with Nitrogen gas. The complete procedure of the development is given in Table. 3.4.

Table 3.4: Resist development procedure.

Step	Process	Description
1	Development	Methyl isobutyl ketone : Isopropanol - 1:3 for 60 seconds.
2	Rinse	20 seconds in an Isopropanol bath.
3	Dry	Aerate with Nitrogen gas.

3.2.5 Step 5. Ferromagnetic Film Deposition Procedure

To fabricate the nano-magnetic devices we have used Permalloy as a soft ferromagnetic material. To deposit a uniform thin film of Permalloy on the sample we used a Varian Model 980-2462 Electron Beam Evaporator. The sample was mounted in the chamber of the evaporator and then the chamber was then pumped down to a pressure of 2 μTorr. Once the chamber reached high vacuum level the electron filament was powered on. In the electron beam evaporator the Permalloy source was heated by the energy provided from the electron beam until it was vaporized. Once the Permalloy source was uniformly heated the shutter was opened and the deposition took place. We evaporated 10 *nm* of Permaloy onto the sample at a rate of 1 - 2 Ås^{-1}.

3.2.6 Step 6. Liftoff Procedure

This is the final step in the fabrication process of nano-magnetic devices. In this step, we selectively remove the unwanted material. In this case the unwanted materials are the unexposed PMMA and the Permalloy on the unexposed PMMA. We want to preserve the Permalloy that was deposited on the Silicon surface. We have used Acetone to selectively remove the organic resist and to preserve the ferromagnetic material on the sample. The unexposed PMMA easily dissolves in Acetone and the Permalloy on top of the unexposed PMMA is also removed synchronously. We dipped the sample in an Acetone bath for 10 minutes. To enhance the removal we agitated the sample in a heated ultrasonic bath. Once the liftoff was completed the sample was rinsed with IPA and dried with Nitrogen gas. A detail description of the liftoff procedure is given in Table. 3.5.

Table 3.5: Liftoff procedure.

Step	Process	Description
1	Liftoff	Agitate the sample for 10 minutes in a warm ultrasonic bath of Acetone.
2	Rinse	5 seconds in a Isopropanol.
3	Dry	Aerate with Nitrogen gas.

3.3 Characterization Process

Characterization of nano-magnetic devices includes topological and magnetic inspection. Topological inspection allows us to identify the defect free nano-magnetic devices. The defect free nano-magnetic devices are then subjected to magnetic inspection to analyses the magnetizations states. Based on the magnetization states of the nano-magnetic devices we can understand and implement computations.

For topological inspection we use a SEM and scanning probe microscope in the AFM mode. A Hitachi SU-70 SEM operating at 30 *kV* was used to obtain lateral measurements of nano-magnetic devices. The working distance of the SEM was reduced to 5 *mm* to obtain high resolution SEM images of the nano-magnetic devices. To obtain thickness measurements of the nano-magnetic devices we used a VEECO DI300 scanning probe microscope in the AFM mode. A Silicon probe with an angle of 22^0 and an apex with a radius of 20 *nm* was mounted onto the scanning probe microscope. The AFM imformation was also used to measure the roughness of the surface of the nano-magnetic devices. Combining the SEM measurements and AFM measurements we were able to identify defect free nano-magnetic devices.

For magnetic inspections of the nano-magnetic devices we used a VEECO DI300 scanning probe microscope in the MFM mode. A magnetic probe was mounted on the scanning probe microscope. There are three types of magnetic probes: Standard moment (coercivity: 400 Oe., moment: $1e^{-13}$ EMU), low moment (coercivity: $<$400 Oe., moment $0.3e^{-13}$ EMU) and low coercivity (coercivity: $<$ 10 Oe., moment: $< 1e^{-13}$ EMU). We used a low moment magnetic probe to obtain high resolution magnetic images of the nano-magnetic logic devices. We used these MFM images of nano-magnetic devices to identify frustration free magnetic systems and realize computation.

Chapter 4: Driving Nano-Magnetic Devices for Data Propagation

Single domain magnets serve as an excellent mechanism to store and preserve Boolean information. The work in this chapter is an effort to establish that data cannot only be stored and altered as in memory but also can be propagated in a causal fashion from the driver to the driven cell in presence of an external field. We have experimented with a ferromagnetic wire having a pair of nano-magnetic devices, which were 20 *nm* apart. A MFM tip, resulting in 8 mT field was used to switch the magnetization of one of the nano-magnetic devices. Even though the individual nano-magnetic device switched its magnetization, the neighbor remained unchanged. This experimentally validates the observation made by Csaba *et al.* [18] that a clocking field is necessary for the neighbor interaction. Finally, we used a DC electromagnet with a field of 45 mT, to provide an out-of-plane clocking field. We observed two important phenomena: (1) the input field was reduced up to 2.5 mT to reverse the magnetization and (2) upon removal of the hard axis field, the neighbor magnet reversed its magnetization according to the input.

The work in this chapter is published in [45] and reused here by permission (see Appendix A). The contributors to this publication are D. K. Karunaratne, J. Pulecio and S. Bhanja.

4.1 Background

Recently, a significant interest has arisen to use magnetism and magnetic materials for computation and computation devices, respectively. Boolean logic information is enumerated in the magnetization in the nano-magnetic device. Cowburn *et al.* [17] were the first to experimentally demonstrate logic operation and information propagation at room temperature using nano-magnetic

devices. The nano-magnetic devices used in this experiment were cylindrical and had no shape anisotropy. Bernstein *et al.* [6] experimented with nano-magnetic devices that were fabricated into a rectangular prism shape. This introduced shape anisotropy and was able to enumerate logic 0 and logic 1 along the magnetic easy axis. Bernstein *et al.* [6] reported a perfect antiferromagnetic ordering along a 64 magnet-long chain. Imre *et al.* [40] were the first to design a nano-magnetic logic architecture and experimentally demonstrated a universal logic gate that can compute the majority of three Boolean inputs or even operate as a NOR or NAND gates by fixing the third input to either logic 1 or 0. They presented MFM images of all possible combinations of majority logic. Varga *et al.* [111] demonstrated the ability of a fan-out signal in nano-magnetic logic architectures and Pulecio *et al.* [87] demonstrated a coplanar crosswire system which has the ability to transfer data over an intersection without any data loss. However, in these set of experiments [6, 17, 40, 87, 111], the nano-magnetic devices were always driven into a stimulated state and relaxed to an energy minimum and there were no observations of an input or a driver driving the neighboring device. Note that this phenomena is essential for the input-output causal ordering of information originated from the input towards the output. This chapter is focused on providing a localized input mechanism to a nano-magnetic device and a clocking scheme for reliable data propagation in a ferromagnetic wire architecture.

4.2 Fabrication and Characterization Process

The nano-magnetic devices were designed using DesignCAD2000 NT and was fabricated on a Silicon wafer. Initially the Silicon wafer was cleaned with an RCA cleaning procedure to remove all organic, ionic, oxide and heavy metal contaminants. The clean Silicon wafer was coated with a uniform layer of 950 Polymethyl methacrylate (PMMA) via a Laurell Technologies WS-400A-8NPP/Lite Spin Processor. The thickness of the PMMA was measured to be approximately 35 *nm*. To achieve this thickness the PMMA was dissolved with Anisole. To remove the unwanted residual solvents on the wafer, the wafer was baked in an oven at $170^{o}C$ for 30 minutes. Once the wafer

was cooled down to room temperature the wafer was loaded into a JEOL 840 scanning electron microscope retrofitted with a Nabity NPGS system to expose the patterns. An acceleration voltage of 35 kV and a beam current of 25 pA were used. The exposed wafer was unloaded and submerged in a Methyl isobutyl ketone/Isopropanol (3:1) developer solution for 60 seconds. The wafer was aerated with Nitrogen and mounted in the chamber of a Varian Model 980-2462 electron beam evaporator to deposit a uniform layer of Permalloy. The evaporation was taken place in a 2 μTorr vacuum at a rate of 2 $\text{Å}s^{-1}$ for 50 seconds resulting with a 10 nm uniform film. Subsequently the wafer was removed from the chamber and submerged in a heated Acetone bath for 10 minutes for the liftoff process. Finally, the samples were characterized with the combination of an SEM and an AFM to identify the defect free ferromagnetic wire architectures.

4.3 Experimental Setup

In this work, we have provided a magnetic input signal and examined the magentic output signal of a ferromagnetic wire architecture. The magnetic input was provided with an MFM tip mounted on a VEECO DI 300 scanning probe microscope (SPM) and was operated in the Nanolithography mode. In [126], the authors have reported observations of a MFM tip influencing the magnetization of a submicron size particle made of a magnetic material. We have used this favorably to toggle the magnetization of a nano-magnetic device in the ferromagnetic wire architecture. To examine the magnetic output we used the same SPM in the MFM mode.

Fig. 4.1 shows the sequence of motions of the MFM tip to toggle the magnetization of a nano-magnetic device. To achieve this controlled motion over the MFM tip, a script in *C* was written and uploaded to the SPM system software in the nanolithography mode. A detailed description of the input parameters and the functionality of the script is given in Algorithm 1.

Since the SPM was not equipped with an X-Y feedback control system and precise movement of the MFM tip was essential to provide an input to a nano-magnetic device, a detail characterization step of the script to maneuver the MFM tip was taken in to account. To observe the MFM tip

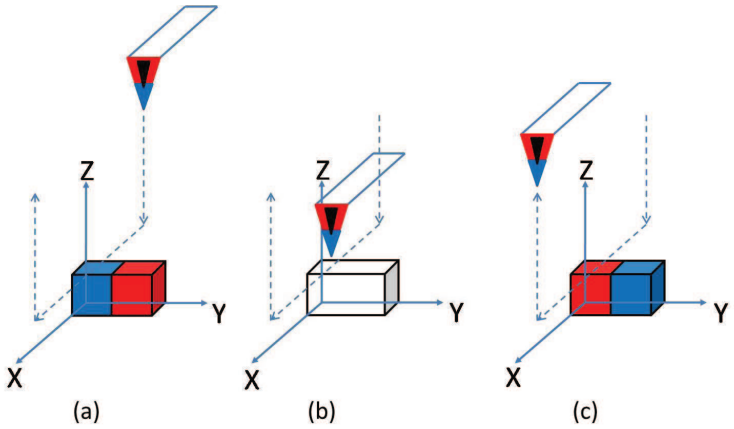

Figure 4.1: Schematic diagram of the MFM tip movement to provide input. (a) Initial position of the MFM tip. (b) MFM tip lowered to 10 *nm* above the surface of the nano-magnetic device and moved over the width. (c) Final position of the MFM tip.

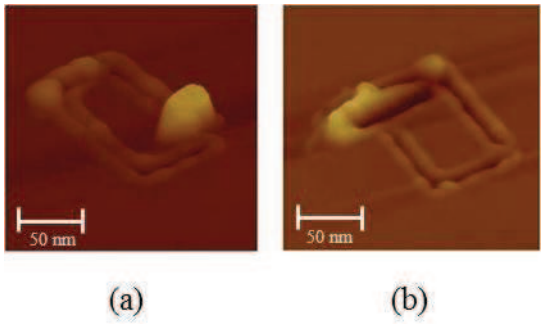

Figure 4.2: (a) AFM 3D image of a 100 *nm* x 50 *nm* rectangle made by nano-indentation. (b) AFM 3D image of a nano-indentation of a line made on the rectangle by the scrip to maneuver the MFM tip to provide input to the nano-magnetic device.

Algorithm 1 Script to move the MFM tip.

Input: Magnetize the nano-magnet in their hard axis
Magnetize tip apex with magnetic south pole
Select the nano-magnet to write data.
Center the nano-magnet in scan area.
Nano-magnet length $L\mu m$.
Nano-magnet width $W\mu m$.
Nano-magnet orientation θ°.
Data writing rate = $r\mu m/s$.
Tip-nano-magnet separation = $d\mu m$.
Correction factor = e.
Store data = b (boolean logic "0" or "1").

Center the tip in scan area.
if b == 1 **then**
    Move tip to $(-e\{\frac{L}{4}\sin\theta + \frac{W}{2}\cos\theta\}, e\{\frac{W}{2}\sin\theta - \frac{L}{4}\cos\theta\})$
    Move tip to tip magnet separation, d
    Move tip to $(e\{W\cos\theta\}, -e\{W\sin\theta\})$
else
    Move tip to $(e\{\frac{L}{4}\sin\theta + \frac{W}{2}\cos\theta\}, e\{-\frac{W}{2}\sin\theta + \frac{L}{4}\cos\theta\})$
    Move tip to tip magnet separation
    Move tip to $(-e\{W\cos\theta\}, e\{W\sin\theta\})$
end if
Move tip up
Data written

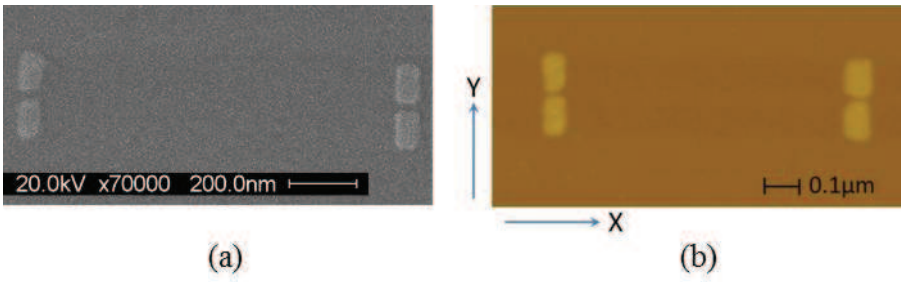

Figure 4.3: (a) SEM image of the ferromagnetic wires (the wire to the right: wire-1 the wire to the left: wire-2).(b) An AFM image of the ferromagnetic wires.

movement we performed a set of nano-indentations on Silicon wafer coated with PMMA. Fig. 4.2(a) shows an AFM image of a rectangle with similar dimensions to our nano-magnetic device made by nano-indentation on the PMMA surface. Fig. 4.2(b) shows the AFM image of a second nano-indentation of a line made on a rectangle similar to the one in Fig. 4.2(a) made by the scrip (Algorithm 1) to maneuver the MFM tip. Fig. 4.2(b) shows that we have achieved precise motion and control of the MFM tip to provide input to the nano-magnetic deivce.

4.4 Data Propagation in Nano-Magnetic Device

To determine the reliability of data propagation via nano-magnetic device, a ferromagnetic wire architecture was fabricated. The magnetic system used for the experiment consisted of two ferromagnetic wires. Each wire has two nano-magnetic device aligned in their easy axis. The separation of each nano-magnetic device in a wire was approximately 20 *nm* and the wires were placed 1 μm away from each other. This separation was sufficient to minimize crosstalk. In the SEM image in Fig. 4.3(a) and the AFM image in Fig. 4.3(b), the wire to the right (wire-1) has nano-magnetic devices with dimensions of 120 *nm* x 60 *nm* x 10 *nm* and it was used for data propagation (nano-magnetic deivces overlaid by white rectangles in Fig. 4.4, 4.6); the wire to the left (wire-2) has nano-magnetic devices with dimensions of 100 *nm* x 50 *nm* x 10*nm* and was used as a reference wire.

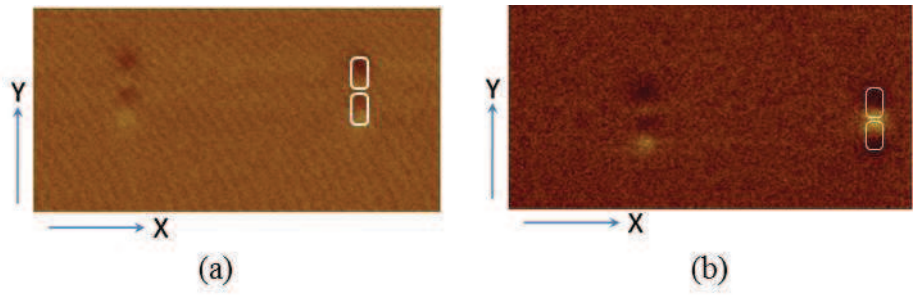

Figure 4.4: (a) MFM image of ferromagnetic wires. An external magnetic field from a DC electromagnet was provided along the easy axis (Y - axis). (b) MFM image of the ferromagnetic wires. An input was given to one of the nano-magnetic devices overlaid by the white rectangles. A frustration can be seen since the neighboring nano-magnetic device did not respond to the input device.

Fig. 4.4(a) shows the MFM image of the initial state of the ferromagnetic wires after an external magnetic field was applied along the easy axis (Y - axis). Fig. 4.4(b) shows the result of providing an input with the standard moment (magnetic moment of $1e^{-13}$ EMU) magnetic tip, moved according to Fig. 4.1 over the input nano-magnetic device of wire-1. As it can be seen in Fig. 4.4(b), a frustration has occurred and data has not propagated to the neighboring nano-magnetic device in wire-1. This experimentally validates the observation made by Csaba *et al.* [18] that a clocking field is necessary for the neighbor interaction.

To propagate data in a ferromagnetic wire a clocking field is essential. The clocking field is required to switch the magnetization of a nano-magnetic device from its in-plane easy axis to its out-of-plane hard axis. This can be done by applying an external magnetic clocking field in the direction of the out-of-plane hard axis (Z - axis). In this experiment, the sample with the magnetic systems was placed in between a conventional iron core direct current (DC) electromagnet and the piezo translator (PZT) of the scanning probe microscope (SPM). Next, the clocking field was gradually increased until an adequate field was applied to change the magnetic moment of the nano-magnetic devices in wire-1 from easy axis to out-of-plane hard axis. Once the magnetization of the nano-magnetic device in wire-1 were in their out-of-plane hard axis, the MFM tip was lowered to provide an input to the input nano-magnetic device in wire-1. When the MFM tip reached 10 *nm*

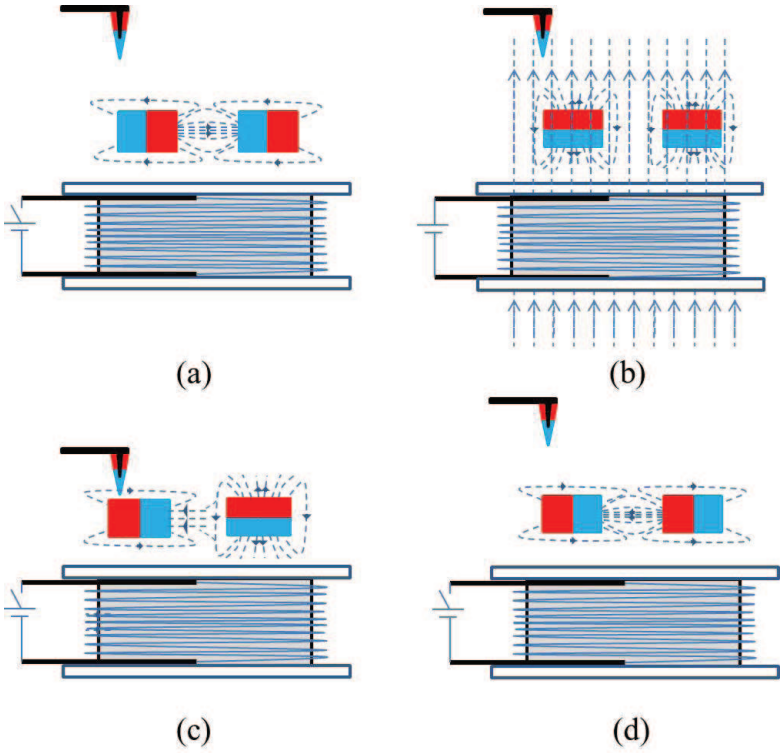

Figure 4.5: Schematic diagram of the MFM tip movement and magnetic field interaction of the nano-magnetic devices. (a) Initial state of the nano-magnetic devices in their easy axis. (b) External clock field provided by the DC electromagnet in the out-of-plane (Z- axis) direction. The nano-magnetic devices flip into their out-of-plane hard axis. (c) External clocking field was removed when the tip was reached the surface to provide an input to the input nano-magnetic device. (d) Final state of the nano-magnetic devices.

above the surface of the input nano-magnetic device the out-of-plane hard axis clocking field was removed. A schematic diagram of this procedure is given in Fig. 4.5.

Fig. 4.6 shows the experimental observation of the above procedure. Initially the wires were subjected to an easy axis external magnetic field and they were saturated in their easy axis (see Fig. 4.4(a)). Next, the sample was subjected to an out-of-plane hard axis clocking field of 45 mT. In the MFM image in Fig. 4.6(a) a single magnetic pole can be seen over wire-1. This validates that wire-1 was in its out-of-plane hard axis while wire-2 remains in its initial magnetic moment (see section 4.4.1). Using the nanolithography mode of the SPM, the mounted low moment MFM tip was moved according to Fig. 4.1 to provide an input to the input nano-magnetic device in wire-

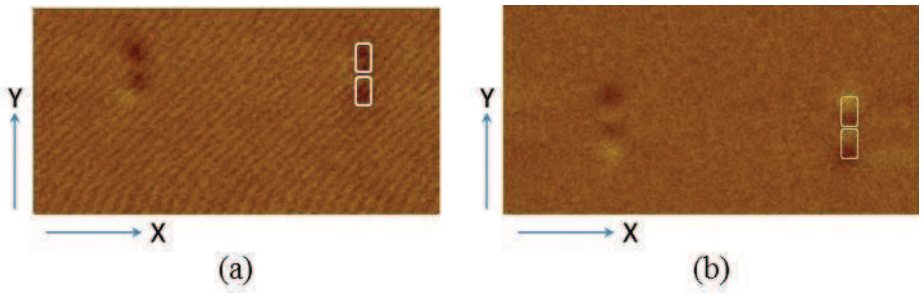

Figure 4.6: (a) MFM image of the ferromagnetic wires under the influence of an out-of-plane hard axis (Z - axis) magnetic field of 45 mT. White rectangle has been overlaid on the nano-magnetic devices which changed their magnetic moment from easy axis to out-of-plane hard axis. (b) MFM image of the ferromagnetic wires after the input is given under the influence of an external clocking field. Note that the neighboring nano-magnetic device has changed their magnetic moment according to the input.

1. We also observed when the magnetization of a nano-magnetic device was in their out-of-plane hard axis direction, a low moment (magnetic moment of $0.3e^{-13}$ EMU) magnetic tip was sufficient to influence the magnetization of the input nano-magnetic device. The input field was reduced up to 2.5 mT to reverse the magnetization of the input magnet with an out-of-plane hard axis magnetization. This experimental observation leads us to believe that a nano-magnetic devices are power efficient if the magnetic moment of a nano-magnetic device is brought to their hard axis before providing an input. When the tip reached 10 nm above the surface of the nano-magnetic device, the clocking field was removed. The MFM image in Fig. 4.6(b) clearly shows the nano-magnet devices in wire-1 had propagated data to the neighboring device from the input device while wire-2 remains in its previous magnetization. This observation can lead us to construct complicated magnetic interconnects and crosswire junctions to propagate data reliably.

4.4.1 Additional Observations

The external magnetic field (clocking field) needed to change the magnetization of a nano-magnetic device with a rectangular shape anisotropy from its in-plane easy axis to out-of-plane hard

axis changes with the magnet dimensions [84]. The total energy E of a nano-magnet can be written as the sum of the magnetocrystalline, shape and exchange bias anisotropies as:

$$E = K + (AR - 1) \times (\frac{t}{L}) \times (M_s^2) + (\frac{(J_{eb}) \times (M_s^2)}{t}) \times (1 - (\frac{T}{T_b})) \tag{4.1}$$

where K is the magneto-crystalline energy, AR the aspect ratio, t is the thickness of the nano-magnet, L is the long axis dimension of the nano-magnet, J_{eb} is the exchange energy, M_s is the saturation magnetization, T the actual temperature and T_b the storage layer blocking temperature. The energy barrier of a nano-magnet, being inversely proportional to the nano-magnet length, L, increases significantly as the nano-magnet size is reduced. Therefore, the required clocking field increases to change the magnetization of a nano-magnet. We experimentally observed this energy difference with the nano-magnetic devices in wire-1 and wire-2. The nano-magnetic devices in both ferromagnetic wires have the same thickness but with different lengths and widths. Wire-2 has smaller nano-magnetic device than the other. We observed that the clocking field of 45 mT was needed to change the magnetizations of the nano-magnetic devices in wire-1 from easy axis to out-of-plane hard axis and that of wire-2 required 50 mT. In the MFM image Fig. 4.6(a), it can be clearly seen that the nano-magnetic devices in wire-1 have changed their magnetic moment from easy axis to out-of-plane hard axis while the nano-magnetic devices in wire-2 remains in their initial magnetic moment in the presence of an out-of-plane external clocking field of 45 mT.

4.5 Conclusion

In this work, we have experimentally demonstrated that a clocking field is essential to propagate data in a ferromagnetic wire. By providing a clocking field we have successfully shown data propagation in a ferromagnetic wire architecture.

Chapter 5: Seven-Input Majority Logic Architecture

Nano-magnetic logic architectures have been a promising technology for logic computation. This work is an effort to determine if indeed the nano-magnetic logic architectures are an error free and a reliable mechanism to process (and propagate) information. For this task we have designed and fabricated six different nano-magnetic logic architectures to compute the majority of seven Boolean variables. Each design consists of three three-input majority logic gates which are interconnected with ferromagnetic and anti-ferromagnetic wire architectures. Each design differs from one another by the arrangement and total number nano-magnetic devices. We have captured MFM images of all six nano-magnetic logic architectures and have observed error-free operations in one of the designs.

The work in this chapter is published in [44] and reused here by permission (see Appendix A). The contributors to this publication are D. K. Karunaratne and S. Bhanja.

5.1 Background

Nano-magnetic logic architectures have been deemed as a potential candidate to replace complementary metal-oxide-semiconductor (CMOS) technology. In nano-magnetic logic architectures, the main computing elements are single domain magnets that have been fabricated from a soft ferromagnetic material into the shape of a rectangular prism. Boolean information is encoded in the magnetization of the nano-magnetic devices and computation takes place by magnetic field interaction. The placements of these nano-magnetic devices are critical for error-free computation and data propagation. Bernstein *et al.* [6] have placed 64 rectangular nano-magnetic devices in an anti-parallel fashion and demonstrated perfect propagation of information from the input to

the output. This type of magnetic wire architecture is recognized as an antiferromagnetic wire architecture. Similarly, Pulecio *et al.* [88] have demonstrated a ferromagnetic wire architecture. In a ferromagnetic wire architecture the rectangular nano-magnetic devices are place in parallel fashion. Imre *et al.* [40] placed five rectangular nano-magnetic devices in the simplest arrangement, that is, a central devices surrounded by four others and have constructed a three-input majority logic gate. By fixing the central input of the three-input majority logic gate to logic 1 or 0, the nano-magnetic logic architecture can function as an OR gate or as an AND gate respectively. In this chapter, we have connected three three-input majority logic gates with ferromagnetic and antiferromagnetic wire architectures and fabricated a complex nano-magnetic logic architecture that can compute the majority of seven Boolean logic variables.

5.2 Fabrication and Characterization Process

The nano-magnetic logic architectures were designed using DesignCAD2000 NT and were fabricated on a Silicon wafer. Initially the Silicon wafer was cleaned with an RCA cleaning procedure to remove all organic, ionic, oxide and heavy metal contaminants. The cleand Silicon wafer was coated with a uniform layer of 950 Polymethyl methacrylate (PMMA) via a Laurell Technologies WS-400A-8NPP/Lite Spin Processor. The thickness of the PMMA was measured to be approximately 35 *nm*. To achieve this thickness the PMMA was dissolved with Anisole. To remove the unwanted residual solvents on the wafer, the wafer was baked in an oven at 170^oC for 30 minutes. Once the wafer was cooled down to room temperature it was loaded into a Hitachi SU-70 scanning electron microscope retrofitted with a Nabity NPGS system to exposure the patterns. An acceleration voltage of 30 *kV* and a beam current of 25 *pA* were used. The exposed wafer was unloaded and submerged in a Methyl isobutyl ketone/Isopropanol (3:1) developer solution for 60 seconds. The wafer was aerated with Nitrogen and mounted in the chamber of a Varian Model 980-2462 electron beam evaporator to deposit a uniform layer of Permalloy. The evaporation took place in a 2 μTorr vacuum at a rate of 2 $Å s^{-1}$ for 50 seconds resulting in a 10 *nm* uniform film.

Subsequently the wafer was removed from the chamber and submerged in a heated Acetone bath for 10 minutes for the liftoff process. Finally, the samples were characterized with the combination of an SEM and an AFM to identify the defect-free nano-magnetic logic architectures.

5.3 Experimental Setup

For computation to take place in nano-magnetic logic architectures they require a stimulation and relaxation process with the assistance of an external magnetic field in the form of a pulse. To provide this external magnetic field we used a direct current (DC) electromagnet powered by a 300W DC power supply. To take measurements of the external magnetic field provided to the sample we used a National Institute of Standards and Technology (NIST) calibrated Gauss meter by AlphaLab. The sample was placed in between two opposite magnetic poles in the electromagnet to provide a uniform out-of-plane hard axis external magnetic field. The external magnetic field was ramped up to 100 mT in 0.1 seconds and kept constant for 0.5 seconds followed by a ramp down over 0.1 seconds.

Once the samples were stimulated and allowed to relax, qualitative magnetic measurements of the nano-magnetic logic architectures were taken using a VEECO DI 300 scanning probe microscope in the MFM mode. A low moment (magnetic moment of $0.3e^{-13}$ EMU) MFM tip was used to take the measurements while minimizing the distortion on the nano-magentic devices.

5.4 Results and Discussion

Fig. 5.1 through Fig. 5.6 shows the schematic diagrams, SEM images and MFM images of the six different nano-magnetic logic architectures designed to compute the majority of seven Boolean logic variables. All nano-magnetic logic architectures consists of three three-input majority logic gates [40, 78] interconnected with ferromagnetic and antiferromagnetic wire architectures [88]. The

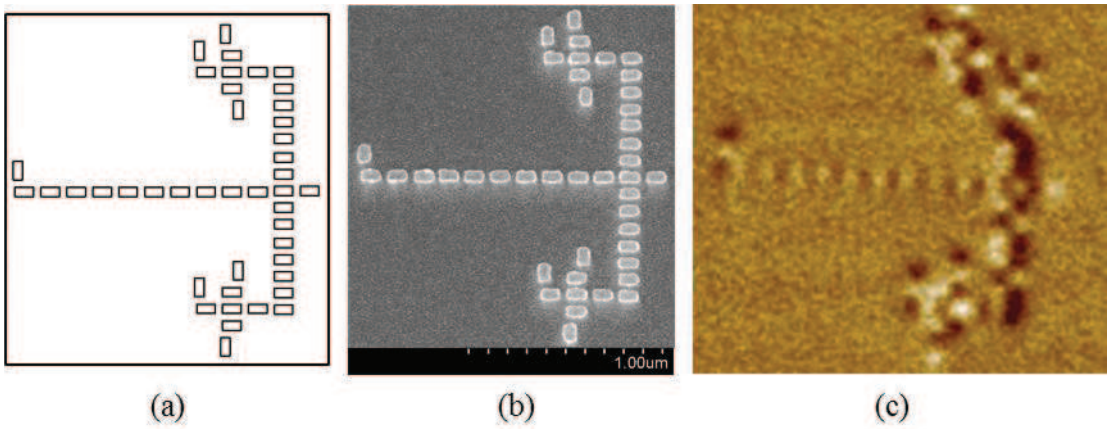

Figure 5.1: (a) Schematic diagram of the nano-magnetic logic architecture with 43 nano-magnetic devices. (b) SEM image of the nano-magnetic logic architecture. (c) MFM image of the nano-magnetic logic architecture.

nano-magnetic logic architectures have been designed such that the information processing nano-magnetic devices have the same latency, and the system would ease to an energy minimum such that the output nano-magnetic device will compute the majority of the seven Boolean logic variables.

Table 5.1: Performance evaluation of the nano-magnetic logic architecture in Figure 5.1.

	0 Error	1 Error	2 Errors	More than 2 erros
Error rate	0	0	0	100%

The schematic diagram in Fig. 5.1(a) shows the placements of the nano-magnetic devices in the first nano-magnetic logic architecture we designed. The three-input majority logic gates used in this nano-magnetic logic architecture was designed and tested by Nomura *et al.* [73, 78]. We have interconnected the output of two three-input majority logic gates to the third three-input majority logic gate with ferromagnetic and antiferromagnetic wire architectures. As can be seen in the SEM image in Fig 5.1(b), the nano-magnetic logic architecture consists of 43 nano-magnetic devices with average dimensions of 100 *nm* x 50 *nm* x 10 *nm* and each been 20 *nm* apart from their nearest neighbors. The nano-magnetic logic architecture was stimulated with an external magnetic field and was allowed to settle to an energy minimum state. The remnant magnetization of the nano-magnetic

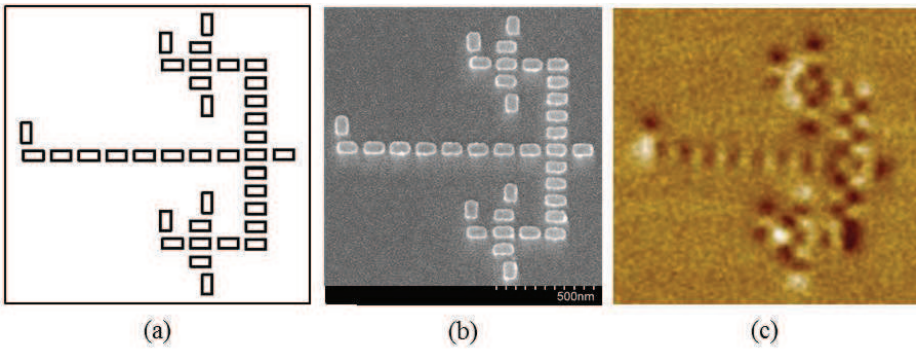

Figure 5.2: (a) Schematic diagram of the nano-magnetic logic architecture with 37 nano-magnetic devices. (b) SEM image of the nano-magnetic logic architecture. (c) MFM image of the nano-magnetic logic architecture.

logic architecture was captured with an MFM. The magnetic frustrations in the nano-magnetic logic architecture were counted as the number of errors in the computation. This experiment was repeated number of times. The MFM image in Fig. 5.1(c) shows the magnetization states of the nano-magnetic devices in the nano-magnetic logic architecture of one of the experiments. Table 5.1 shows the error occurrence of all the experiments as a percentage. In this nano-magnetic logic architecture most of the magnetic frustration occurred in the antiferromagnetic wires. To overcome this problem we designed the nano-magnetic logic architecture in Fig. 5.2 with shorter antiferromagnetic wires.

Table 5.2: Performance evaluation of the nano-magnetic logic architecture in Figure 5.2.

	0 Error	1 Error	2 Errors	More than 2 erros
Error rate	0	9%	27.37%	63.63%

The schematic diagram in Fig. 5.2(a) shows the placements of the nano-magnetic devices in the second nano-magnetic logic architecture we designed. The three-input majority logic gate used in this nano-magnetic logic architecture was designed and tested by Nomura *et al.* [73, 78]. We have interconnected the output of two three-input majority logic gates to the third three-input majority logic gate with antiferromagnetic and ferromagnetic wire architectures. As is evident in the SEM image in Fig 5.2(b), the nano-magnetic logic architecture consists of 37 nano-magnetic devices

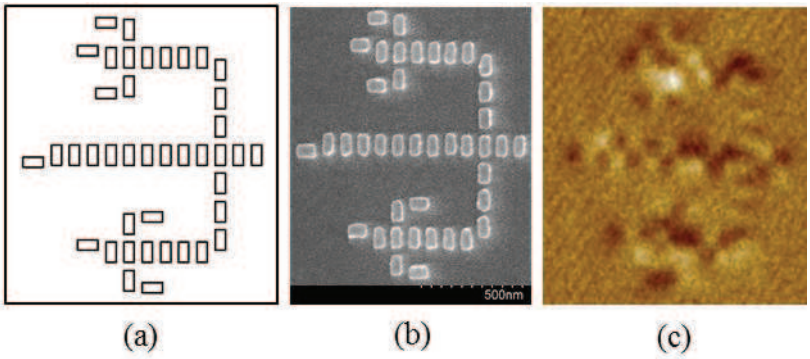

Figure 5.3: (a) Schematic diagram of the nano-magnetic logic architecture with 41 nano-magnetic devices. (b) SEM image of the nano-magnetic logic architecture. (c) MFM image of the nano-magnetic logic architecture.

with average dimensions of 100 *nm* x 50 *nm* x 10 *nm* and each been 20 *nm* apart from their nearest neighbors. Similarly, as with the nano-magnetic logic architecture in Fig. 5.1, this sample was also stimulated with an external magnetic field and was allowed to relaxe before the MFM measurements were taken. The MFM image in Fig. 5.2(c) shows the magnetization states of the nano-magnetic devices in the nano-magnetic logic architecture of one of the experiments. Table 5.2 shows the error occurrence of all the experiments as a percentage. Comparing the results in Table 5.1 for the nano-magnetic logic architecture in Fig. 5.1 and in Table 5.2 for the nano-magnetic logic architecture in Fig. 5.2, we can see the number of errors have reduced by shortening the antiferromagnetic wires in the nano-magnetic logic architecture.

Table 5.3: Performance evaluation of the nano-magnetic logic architecture in Figure 5.3.

	0 Error	1 Error	2 Errors	More than 2 erros
Error rate	0	0	0	100%

The schematic diagram in Fig. 5.3(a) shows the placements of the nano-magnetic devices in the third nano-magnetic logic architecture we designed. The three-input majority logic gate used in this nano-magnetic logic architecture was designed and tested by Imre *et al.* [40]. We have interconnected the output of two three-input majority logic gates to the third three-input majority

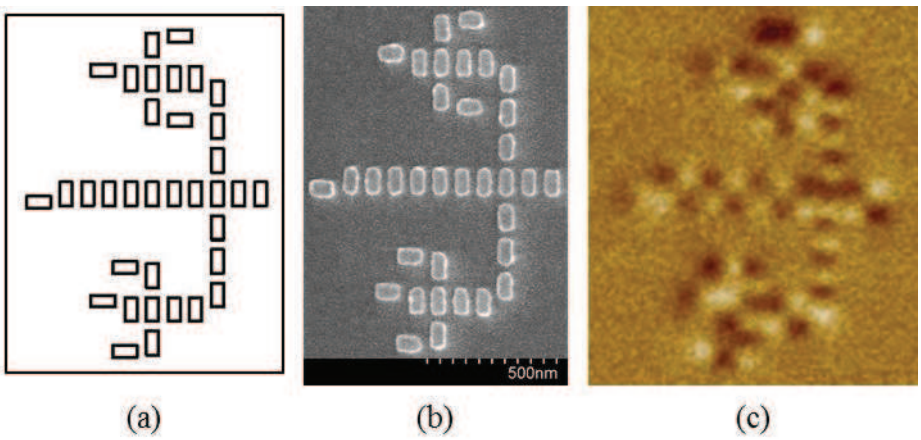

Figure 5.4: (a) Schematic diagram of the nano-magnetic logic architecture with 35 nano-magnetic devices. (b) SEM image of the nano-magnetic logic architecture. (c) MFM image of the nano-magnetic logic architecture.

logic gate with ferromagnetic and antiferromagnetic wire architectures. In this design we have used a step junction at the antiferromagnetic and ferromagnetic wire junction. As can be seen in the SEM image in Fig 5.3(b), the nano-magnetic logic architecture consists of 41 nano-magnetic devices with average dimensions of 100 *nm* x 50 *nm* x 10 *nm* and each been 20 *nm* apart from their nearest neighbors. The nano-magnetic logic architecture was stimulated with an external magnetic field and was allowed to settle to an energy minimum state. The remnant magnetization of the nano-magnetic devices was captured with an MFM. The magnetic frustrations in the nano-magnetic logic architecture were counted as the number of errors in the computation. This experiment was repeated multiple times. The MFM image in Fig. 5.3(c) shows the magnetization states of the nano-magnetic devices in the nano-magnetic logic architecture of one of the experiments. Table 5.3 shows the error occurrence of all the experiments as a percentage. In this nano-magnetic logic architecture most of the magnetic frustrations occurred in the antiferromagnetic wires. To overcome this problem we designed the nano-magnetic logic architecture in Fig. 5.3 with shorter antiferromagnetic wires.

Table 5.4: Performance evaluation of the nano-magnetic logic architecture in Figure 5.4.

	0 Error	1 Error	2 Errors	More than 2 erros
Error rate	0	0	50%	50%

The schematic diagram in Fig. 5.4(a) shows the placements of the nano-magnetic devices in the fourth nano-magnetic logic architecture we designed. The three-input majority logic gate used in this nano-magnetic logic architecture was designed and tested by Imre *et al.* [40]. We have interconnected the output of two three-input majority logic gates to the third three-input majority logic gate with ferromagnetic and antiferromagnetic wire architectures. In this design also we have used a step junction at the antiferromagnetic and ferromagnetic wire connection. The only difference between the nano-magnetic logic architecture in Fig. 5.3 and this nano-magnetic logic architecture is that this has used less number of nano-magnetic devices. As is evident in the SEM image in Fig 5.4(b), the nano-magnetic logic architecture consists of 35 nano-magnetic devices with average dimensions of 100 *nm* x 50 *nm* x 10 *nm* and each been 20 *nm* apart from their nearest neighbors. Similarly, as with the nano-magnetic logic architecture in Fig. 5.3, this architecture was stimulated with an external magnetic field and was allowed to relaxe before the MFM measurements were taken. The MFM image in Fig. 5.4(c) shows the magnetization states of the nano-magnetic devices in the nano-magnetic logic architecture of one of the experiments. Table 5.4 shows the error occurrence of all the experiments as a percentage. Comparing the results in Table 5.3 for the nano-magnetic logic architecture in Fig. 5.3 and in Table 5.4 for the nano-magnetic logic architecture in Fig. 5.4 we can see that the number of errors have reduced by shortening the antiferromagnetic wires in the nano-magnetic logic architecture but there was no improvement of error free computation with the step junction at the antiferromagnetic and ferromagnetic wire connection.

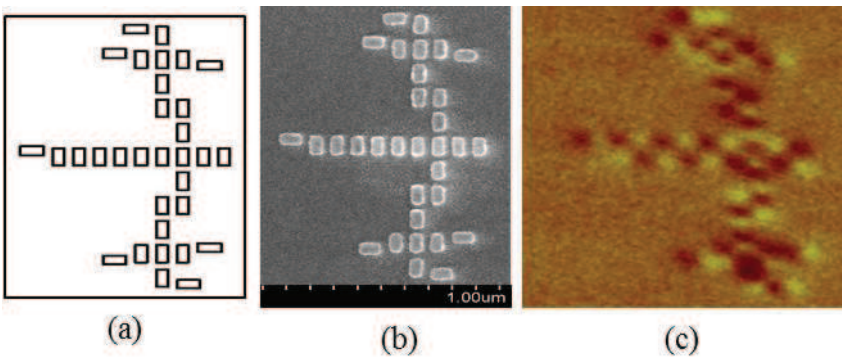

Figure 5.5: (a) Schematic diagram of the nano-magnetic logic architecture with 32 nano-magnetic devices. (b) SEM image of the nano-magnetic logic architecture. (c) MFM image of the nano-magnetic logic architecture.

Table 5.5: Performance evaluation of the nano-magnetic logic architecture in Figure 5.5.

	0 Error	1 Error	2 Errors	More than 2 erros
Error rate	0	33.33%	0%	66.67%

The schematic diagram in Fig. 5.5(a) shows the placements of the nano-magnetic devices in the fifth nano-magnetic logic architecture we designed. In this nano-magnetic logic architecture we have used two three-input majority logic gates designed by Nomura *et al.* [73, 78] and one from Imre *et al.* [40]. We have interconnected the output of two three-input majority logic gates to the third three-input majority logic gate with antiferromagnetic wire architectures. As can be seen in the SEM image in Fig 5.5(b), the nano-magnetic logic architecture consists of 32 nano-magnetic devices with average dimensions of 100 *nm* x 50 *nm* x 10 *nm* and each been 20 *nm* apart from their nearest neighbors. The nano-magnetic logic architecture was stimulated with an external magnetic field and was then allowed to settle to an energy minimum state. The remnant magnetization of the nano-magnetic logic architecture was captured with a MFM. The magnetic frustrations in the nano-magnetic logic architecture were counted as the number of errors in the computation. This experiment was repeated a number of times. The MFM image in Fig. 5.5(c) shows the magnetization states of the nano-magnetic devices in the nano-magnetic logic architecture of one of

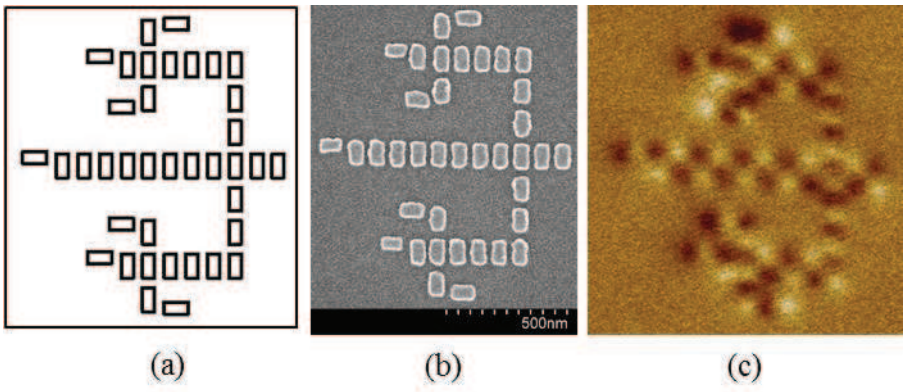

Figure 5.6: (a) Schematic diagram of the nano-magnetic logic architecture with 38 nano-magnetic devices. (b) SEM image of the nano-magnetic logic architecture. (c) MFM image of the nano-magnetic logic architecture.

the experiments. Table 5.5 shows the error occurrence of all the experiments as a percentage. In this nano-magnetic logic architecture most of the magnetic frustrations occurred in the antiferromagnetic wire.

Table 5.6: Performance evaluation of the nano-magnetic logic architecture in Figure 5.6.

	0 Error	1 Error	2 Errors	More than 2 erros
Error rate	0	14.29%	28.57%	57.14%

The schematic diagram in Fig. 5.6(a) shows the placements of the nano-magnetic devices in the sixth nano-magnetic logic architecture we designed. The three-input majority logic gate used in this nano-magnetic logic architecture was designed and tested by Imre *et al.* [40]. We have interconnected the output of two three-input majority loigc gates to the third three-input majority logic gate with antiferromagnetic and ferromagnetic wire architectures. As can be seen in the SEM image in Fig 5.6(b), the nano-magnetic logic architecture consists of 38 nano-magnetic devices with average dimensions of 100 *nm* x 50 *nm* x 10 *nm* and each been 20 *nm* apart from their nearest neighbors. The nano-magnetic logic architecture was stimulated with an external magnetic field and was allowed to settle to an energy minimum state. The remnant magnetization of the nano-magnetic logic architecture was captured with an MFM. The magnetic frustrations in the nano-magnetic logic

architecture were counted as the number of errors in the computation. This experiment was repeated a number of times. The MFM image in Fig. 5.6(c) shows the magnetization states of the nano-magnetic devices in the nano-magnetic logic architecture of one of the experiments. Table 5.6 shows the error occurrence of all the experiments as a percentage. Comparing this nano-magnetic logic architecture with the other five nano-magnetic logic architectures we designed to compute the majority of seven Boolean logic variables, this was the nano-magnetic logic architecture that gave the best performance. Therefore, we further tested with this nano-magnetic logic architecture to achieve an error free, reliable computation.

5.4.1 Error Free Computation and Functionality of the Seven-Input Majority Logic Architecture

After further testing by stimulating and imaging the nano-magnetic logic architecture in Fig. 5.6, we were able to achieve multiple error free computations. The MFM image in Fig. 5.7(c) shoes one such error-free computation. It is evident from MFM image in Fig. 5.7(c) that the magnetization states of all the nano-magnetic devices in the nano-magnetic logic architecture are aligned correctly and has no magnetic frustrations. For the experimental results shown in Fig. 5.7, we have provided all seven-inputs with logic 1, and the nano-magnetic logic architecture has computed logic 1 as the output, which is the expected correct output. Table 5.7 shows the error occurrence of all the experiments as a percentage. The nano-magnetic logic architecture was able compute the correct output for more than 45% of the experiments.

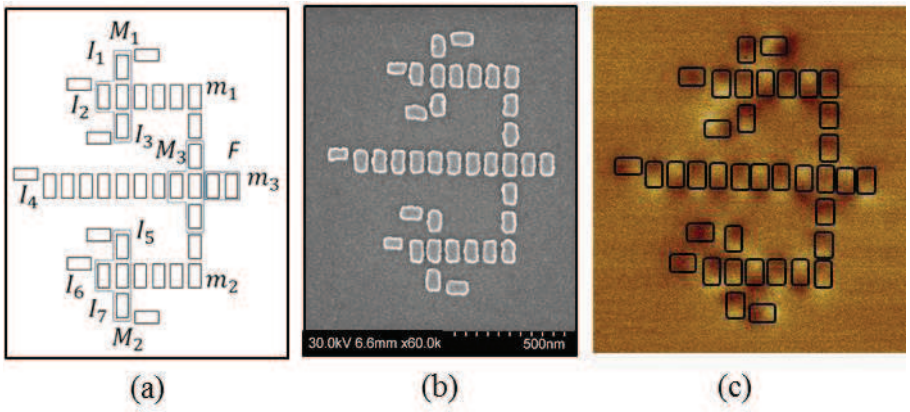

Figure 5.7: (a) Schematic diagram of the nano-magnetic logic architecture with 38 nano-magnetic devices (error free). (b) SEM image of the nano-magnetic logic architecture. (c) MFM image of an error free computation the nano-magnetic logic architecture.

Table 5.7: Performance evaluation of the nano-magnetic logic architecture in Figure 5.7.

	0 Error	1 Error	2 Errors	More than 2 erros
Error rate	45.45%	45.45%	0%	9.1%

Fig. 5.7(a) shows the schematic diagram of the nano-magnetic logic architecture with the three-input majority logic gates and fanout circuit overlaid with blue lines. The seven-input majority loigc architecture consists of seven input variables (I_{1-7}) (Boolean), three three-input majority logic gates (M_{1-3}) and a fanout (F) circuit. The architecture was designed to operate in two levels. In the first level, it computes the majority (m_1) of inputs I_{1-3} and majority (m_2) of inputs I_{5-7}. In the second level, it computes the majority (m_3) of inputs I_4, m_1 and m_2 where m_3 is the majority of all seven input variables.

Fig. 5.8 shows the data propagation sequence in the nano-magnetic logic architecture in Fig 5.7. If we provide the inputs to the nano-magnetic logic architecture at $t = T$ seconds and assume the computation time for one nano-magneti devices was Δt seconds, then it takes $T + 2\Delta t$ seconds for the first level computation and at $t = T + 8\Delta t$ seconds the data would reach the third three-input

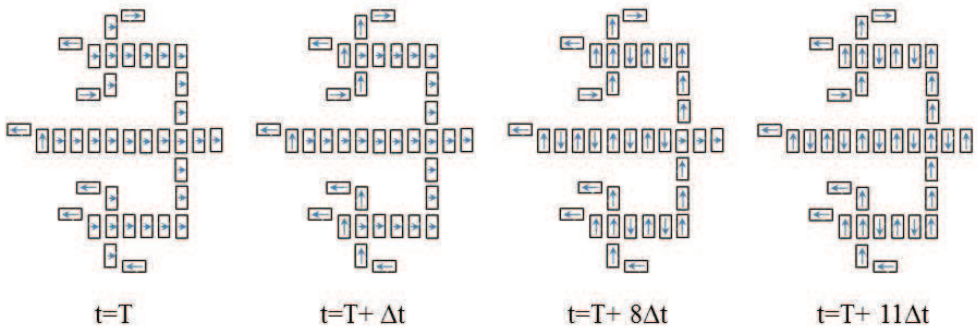

Figure 5.8: The timing diagram of data propagation from input to output in the seven-input majority logic architecture in Figure 5.7. [t = time in seconds, T = input given time, Δt = Nano-magnetic device processing time]

majority logic gate, M_3. For second level computation to complete it takes $T + 9\Delta t$ seconds and to read the output from the output nano-magnetic device it takes $11\Delta t$ seconds.

5.4.2 Re-configurability of the Seven-Input Majority Architecture

The seven-input majority logic architecture can be viewed as a re-configurable hardware device. The hardware may be magnetically configured to suit a particular application/logic function. The ability to reconfigure hardware is useful and cost effective for more than prototyping simple devices. If the second (middle) input of a three-input majority logic gate [40] is set to binary logic 1 it functions as a AND gate, and likewise if the input is set to logic 0 it functions as an OR gate. By simply fixing the binary states of inputs I_2, I_4, and I_6 of the three-input majority logic gates M_1, M_2, M_3 respectively to ether logic 0 or 1, we can program the seven-input majority logic architecture to work in eight different hardware configurations. If the input variables are set to I_1 = A, I_3 = B, I_6 = C and I_7 = D where A, B, C and D are binary values, the re-configurable seven-input majority logic architecture works as [A.B + C.D], [A+B . C+D], [A+B + C.D], [A+B + C+D], [A.B + C+D], [A+B . C.D], [A.B . C.D], [A.B . C+D]. If the input variable C = $\bar{A}$ and B = $\bar{D}$, the architecture could be

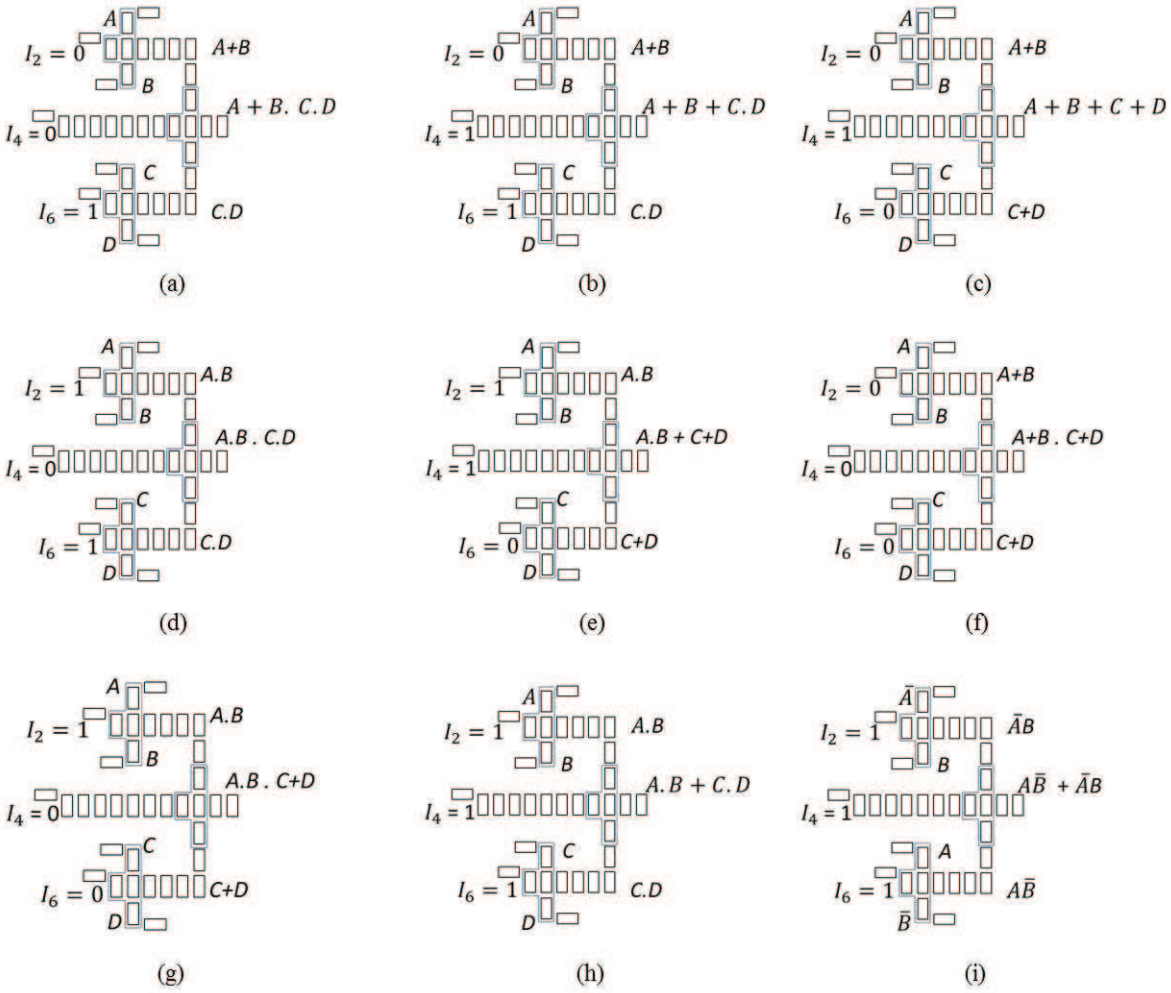

Figure 5.9: Re-configurability of the seven-input majority logic architecture.

configured to function as a XOR or as the sum of a half-adder circuit. The schematic diagrams in Fig. 5.9 shows all possible re-configurable hardware configurations.

5.5 Conclusion

In this chapter, we have designed and fabricated six different nano-magnetic logic architectures that can compute the majority of seven Boolean logic variables. Even though we observed error-free

operations, it became clear that we needed a better control over single layer nano-magnetic devices to minimize the magnetic frustrations that occured in nano-magnetic logic architectures. These magnetic frustrations can be minimized by implementing the methods and techniques proposed by Carlton *et al.* [11] and Niemier *et al.* [76]. Regardless of additional modifications to single layer nano-magnetic devices, unidirectional field approach used for clocking has a high tendency to give errors in nano-magnetic logic architectures. To minimize these errors and for better control and access mechanisms over individual single layer nano-magnetic devices we have moved to multilayer nano-magnetic device, which we will discuss in the next chapter.

Chapter 6: Multilayer Nano-Magnetic Devices

Nano-magnetic logic architectures have proven the ability to propagate and process data. It was also evident that we need better control (write/read/clock) over individual single nano-magnetic devices in a nano-magnetic logic architecture for successful long-term operation. In this chapter, we have proposed a multilayer nano-magnetic device that has the potential of addressing the read, write and clock problems in single layer nano-magnetic devices. The multilayer nano-magnetic device we have designed has a bottom layer with a perpendicular magnetization, a spacer layer with a non-magnetic conducting metal and a free layer with an in-plane magnetization (we have named this device as Spin Valve Base Nano-magnetic-logic (SVBN)). We have performed a set of experiments with SVBN devices to realize neighbor interaction between adjacent free layers of the devices. Based on the MFM images, we conclude that dipolar coupling between the free layers of the neighboring multilayer nano-magnetic devices can be exploited to construct local elements like the three-input majority logic gates, inverters and interconnects.

The work in this chapter is published in [44]. The contributors to this publication are D. K. Karunaratne and S. Bhanja.

6.1 Background

Continuous scaling of the metal-oxide-semiconductor field-effect transistor (MOSFET) physical gate length to improve the performance of electronic appliances is no longer possible due to the influence of quantum effects which are degrading and ultimately prohibiting conventional device operation [2]. In order to keep improving the performances of electronic appliances, researchers are

exploring novel devices/computing paradigms that will either co-exist or replace current MOSFET technology.

Nano-magnetic devices have been deemed as a potential candidate beyond MOSFET technology. However, to successfully perform long-term computation with nano-magnetic devices we have to overcome the write/clock/read problems. There have been few attempts to solve these problems in nano-magnetic devices [3, 56, 61, 62, 64, 65]. Alam *et al.* [3] have demonstrated an on chip clocking system. In this work they have fabricated single layer nano-magnetic devices over a current carrying copper wire. They were able to write data on to the nano-magnetic device by passing 680 *mA* through the copper wire. In this magnetic system the nano-magnetic devices were switching independently without any neighbor interaction since, the spacing between the devices were approximately 300 *nm*. Lyle *et al.* [65] have demonstrated the readability of the nano-magnetic devices by placing magnetic tunnel junctions as two neighboring devices. Since the bottom layer of the magnetic tunnel junctions were coupled with the free layer, the problem of dynamic measurements was not addressed. Liu *et al.* [62] have performed a set of simulation experiments on an interface between a nano-magnetic device and an electrical circuitry to address write/clock/read problems.

In this chapter we have proposed and experimentally demonstrated a magnetic multilayer structure that can address the write and clock issues in single layer nano-magnetic devices for computation. To design and implement the multilayer structure for computation, we have enriched the existing Magnetoresistive Random Access Memory (MRAM) technology [114]. Unfortunately, conventional MRAM cells (that is, a multilayer stack with a magnetic bottom layer that has a fixed in-plane magnetization, non-magnetic spacer layer and a soft magnetic top layer that has an in-plane magnetization) cannot be used for computation because the magnetic coupling energy between the bottom and top layers dominates the coupling energy between the adjacent top layers. (See Fig. 6.1.) To overcome this problem we have engineered the bottom layer to have a perpendicular (out-of-plane) magnetization. By doing this, we have minimized the magnetic coupling between the bottom and top layers and have allowed magnetic coupling to take place between the adjacent top layers. (See Fig. 6.2.) This multilayer structure potentially allows us to write data on to

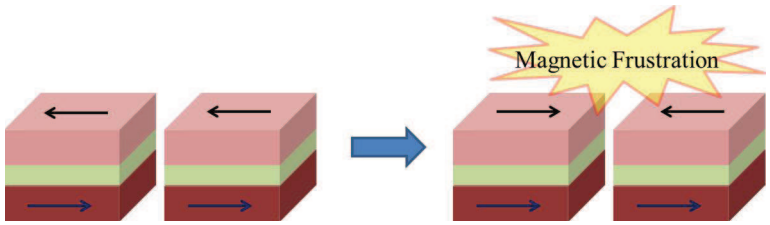

Figure 6.1: Neighbor interaction between two magnetic multilayer devices that have a bottom layer with an in-plane magnetization.

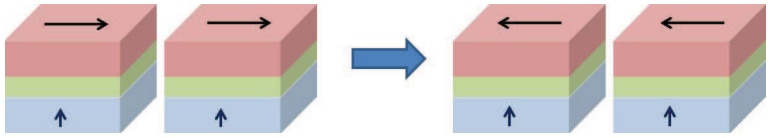

Figure 6.2: Neighbor interaction between two magnetic multilayer devices that have a bottom layer with a perpendicular magnetization.

the top layer by means of spin polarized current [5, 63] and to clock the device by means of passing current from the top layer to the bottom layer. In both cases spin transfer torque is used to change the magnetization dynamics [59]. When writing data the magnetization of the top layer is changed between positive and negative in-plane directions and when clocking the device the top layer magnetization is changed from in-plane direction to out-of-plane direction.

6.2 Spin Valve Based Nano-magnetic-logic (SVBN) Devices

The multilayer structure we have designed and implemented has a bottom layer with a perpendicular magnetic anisotropy, a spacer layer with a non-magnetic conducting metal and a top layer with an in-plane magnetization to switch its magnetic moment according to neighbor interaction (see Fig. 6.3). To obtain a perpendicular magnetization for the bottom layer we have used a thin film of Cobalt. Experimental demonstration in [9, 19, 118] have shown that if the Cobalt thin film is less than 1 *nm*, it would have a perpendicular magnetization. We have designed the bottom layer to have a thickness between 4 Å to 6 Å of Cobalt. As for the spacer layer we have used a thin film of

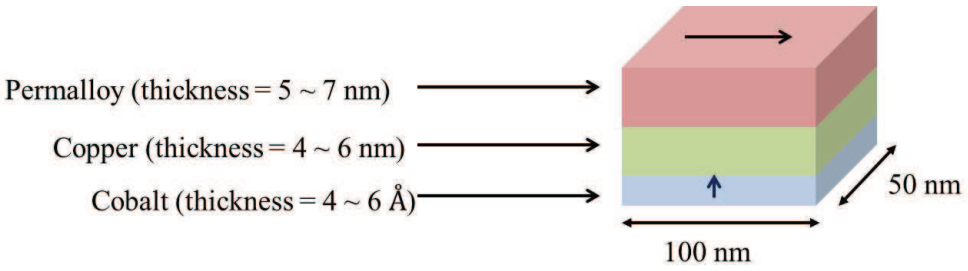

Figure 6.3: Schematic diagram of Spin Valve Based Nano-magnetic-logic (SVBN) device.

Copper since it is a non-magnetic conducting metal. The thickness of the Copper film was between 4 *nm* and 6 *nm*. The top layer was made of Permalloy due to the fact that Permalloy has a very low coercivity and thus its magnetization is easily susceptible to change in the in-plane direction. The thickness of the top layer was between 5 *nm* and 7 *nm*. The lateral dimensions of the multilayer stack was 100 *nm* x 50 *nm* and the nearest-neighbors spacing was about 20 *nm*. Since this multilayer stack has a similar structure to a spin-valve [22, 108], we have named this multilayer nano-magnetic device as Spin Valve Based Nano-magnetic-logic (SVBN).

6.3 Fabrication and Characterization Process

We have fabricated closely placed SVBN devices in the arrangements of ferromagnetic wire architecture, antiferromagnetic wire architecture and a three-input majority logic gate (see Fig. 6.6(a), 6.7(a) 6.8(a), 6.9(a) and 6.10(a)). The architectures were designed using DesignCAD2000 NT and were fabricated on a Silicon wafer. Initially the Silicon wafer was cleaned with an RCA cleaning procedure to remove all organic, ionic, oxide and heavy metal contaminants. The clean Silicon wafer was coated with a uniform layer of 950 Polymethyl methacrylate (PMMA) via a Laurell Technologies WS-400A-8NPP/Lite Spin Processor. The thickness of the PMMA was measured to be approximately 45 *nm*. To achieve this thickness the PMMA was dissolved with Anisole. To remove the unwanted residual solvents on the wafer, the wafer was baked in an oven at $170^{o}C$ for

30 minutes. Once the wafer was cooled down to room temperature it was loaded into a Hitachi SU-70 scanning electron microscope retrofitted with a Nabity NPGS system to expose the patterns. An acceleration voltage of 30 *kV* and a beam current of 25 *pA* were used. The exposed wafer was unloaded and submerged in a Methyl isobutyl ketone/Isopropanol (3:1) developer solution for 60 seconds. The patterned wafer was aerated with Nitrogen and carefully mounted in the chamber of a Varian Model 980-2462 electron beam evaporator to deposit the thin films of Cobalt, Copper and Permalloy. A second silicon wafer was placed in close vicinity to the patterned sample in the electron beam evaporator chamber for X-ray reflectivity (XRR) measurements of the multilayer stack. To obtain a bottom layer with a perpendicular magnetic anisotropy the SVBN devices were fabricated on a silicon wafer with a lattice orientation of $<100>$. The substrate temperature was 50^{o}C. A thin layer of Cobalt was evaporated at a rate of 0.1 Å/s in a high vacuum chamber. The slow growth rate and the thermal energy encouraged a high quality cobalt epitaxial to have a $<100>$ crystal lattice resulting in a high magnetocrystalline anisotropy energy in the perpendicular direction. This allowed the bottom layer in the stack to have a perpendicular magnetic anisotropy. Next, a thin layer of Copper was deposited at a rate of 0.2 Å/s to function as the spacer of the stack. Finally, as for the free layer, a thin layer of Permalloy was evaporated with a rate of 0.2 Å/s in the same vacuum chamber. Once the evaporation of the multilayer stack was completed the patterned wafer was submerged in a heated Acetone bath for 10 minutes for the liftoff process. The flow diagram of the fabrication process is shown in Fig. 6.4.

The second silicon wafer that was placed in the close vicinity to the patterned sample in the electron beam evaporator was subjected to XRR analysis to measure the thickness of each layer in the multilayer stack. For the XRR measurements, a PANalytical′s X′Pert PRO Materials Research Diffractometer was used. Fig 6.5 and Table 6.1 shows the XRR result of the thickness and the roughness of each layer in the multilayer stack. Next, the patterned wafer was subjected to topological measurements to identify defect-free SVBN devices. For topological characterization a Hitachi SU-70 scanning electron microscope and a VEECO DI3000 scanning probe microscope in the AFM mode were used. The lateral dimension of the SVBN devices was approximately 100 *nm* x 50 *nm* and the spacing between the nearest neighbor was approximately 20 *nm*.

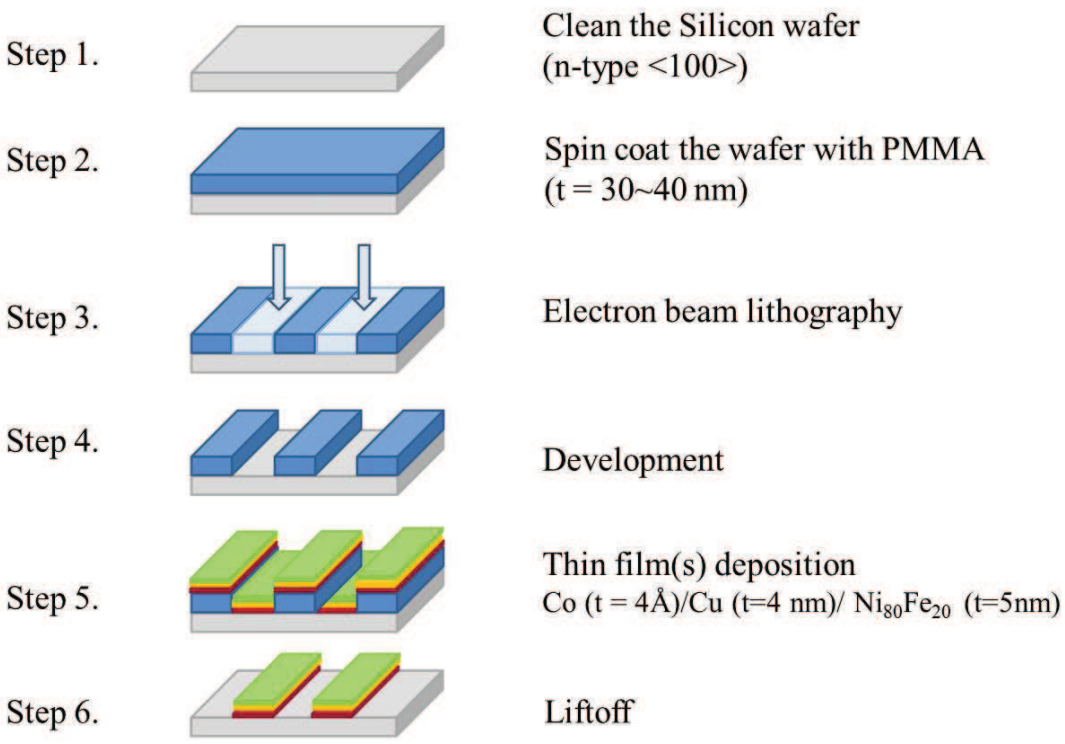

Figure 6.4: A flow diagram of the fabrication procedure to fabricate SVBN devices.

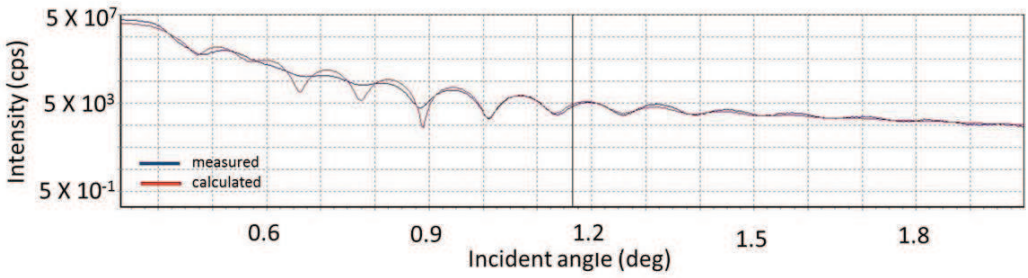

Figure 6.5: Specular-reflective curve for Si/Co/Cu/$Ni_{80}Fe_{20}$.

Table 6.1: XRR results of the multilayer thin films.

Material	Density (g/cm 3)	Thickness (nm)	Roughness (nm)
$Ni_{80}Fe_{20}$	8.681	5	0.2
Cu	8.96	4	0.2
Co	8.9	0.4	0.1
Si	2.33	Substrate	0.1

6.4 Experimental Setup

The main intention of this experiment was to make observations for a proof of concept that the top layers would have neighbor interaction and would compute the correct output. In order for computation to take place the multilayer nano-magnetic devices require a stimulation and relaxation process with assistance of an external magnetic field in the form of a pulse. To provide an external magnetic field we used a direct current (DC) electromagnet powered by a 300W DC power supply. To take measurements of the external magnetic field provided to the sample we used a National Institute of Standards and Technology (NIST) calibrated Gauss meter by AlphaLab. The sample was placed in between two opposite magnetic poles in the electromagnet to prove a uniform out-of-plane hard axis external magnetic field. The external magnetic field was ramped up to 100 mT in 0.1 seconds and kept constant for 0.5 seconds followed by a ramp down over 0.1 seconds.

Once the samples were stimulated and allowed to relax to an energy minimum, qualitative magnetic measurements of the top layers of SVBN devices were taken from a VEECO DI 300 scanning probe microscope in the MFM mode. A low moment (magnetic moment of $0.3e^{-13}$ EMU) MFM tip was used to take the measurements while minimizing the distortion on the SVBN devices.

6.5 Results and Discussion

A ferromagnetic wire architecture was fabricated with four SVBN devices similar to the schematic diagram in Fig. 6.6(a). The SEM image in Fig. 6.6(b) shows the fabricated ferromagnetic wire architecture with four SVBN devices. The average dimensions of the SVBN devices in the ferromagnetic wire architecture were about 100 *nm* x 50 *nm* and the spacing between the nearest neighbor was about 20 *nm*. We have assumed that the thickness of each layer in the SVBN devices in Fig. 6.6(b) was similar to the values in Table. 6.1. The MFM image in Fig. 6.6(c) shows the magnetization of the top layers of the SVBN devices in the ferromagnetic wire architecture in Fig. 6.6(b). It is evident from the MFM image in Fig. 6.6(c) that there are no magnetic frustrations in the system and the ferromagnetic wire architecture with four SVBN devices have propagated the correct information from one end to the other.

The ferromagnetic wire architecture with four SVBN devices was extended to a ferromagnetic wire architecture with eight SVBN devices. The schematic diagram of the ferromagnetic wire architecture with eight SVBN devices is shown in Fig. 6.7(a). The SEM image in Fig. 6.7(b) shows the fabricated ferromagnetic wire architecture with eight SVBN devices. The average dimensions of the SVBN devices in the ferromagnetic wire architecture were about 100 *nm* x 50 *nm* and the spacing between the nearest neighbor was about 20 *nm*. We have assumed that the thickness of each layer in the SVBN devices in Fig. 6.7(b) has a similar value to the ones in Table. 6.1. The MFM image in Fig. 6.7(c) shows the magnetization of the top layers of the SVBN devices in the ferromagnetic wire architecture in Fig. 6.7(b). It is evident from the MFM image in Fig. 6.7(c) that there are no magnetic frustrations in the system and the ferromagnetic wire architecture with eight SVBN devices has propagated the correct information from one end to the other.

The schematic diagram in Fig. 6.8(a) shows an antiferromagnetic wire architecture with four SVBN devices. The fabricated antiferromagnetic wire architecture with four SVBN devices is shown in the SEM image in Fig. 6.8(b). The average dimensions of the SVBN device in the antiferromagnetic wire architecture was about 100 *nm* x 50 *nm* and the spacing between the nearest neighbor was about 20 *nm*. We have assumed that the thickness of each layer in the SVBN devices in

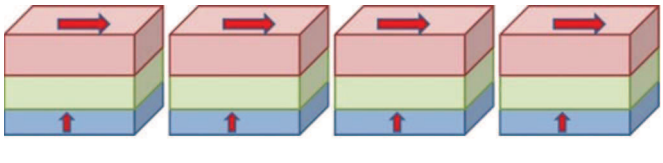

(a)

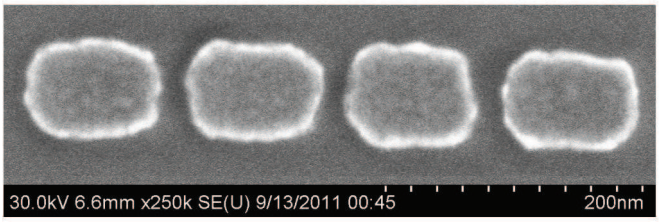

(b)

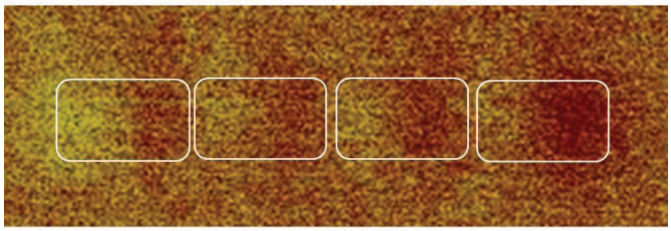

(c)

Figure 6.6: (a) Schematic diagram of a ferromagnetic wire architecture with four SVBN devices. (b) SEM image of a ferromagnetic wire architecture with four SVBN devices. (c) MFM image of a ferromagnetic wire architecture with four SVBN devices.

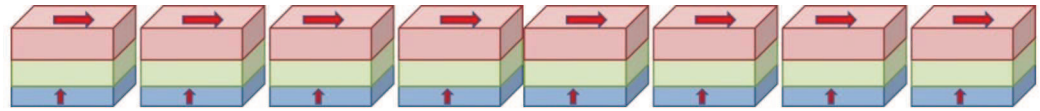

(a)

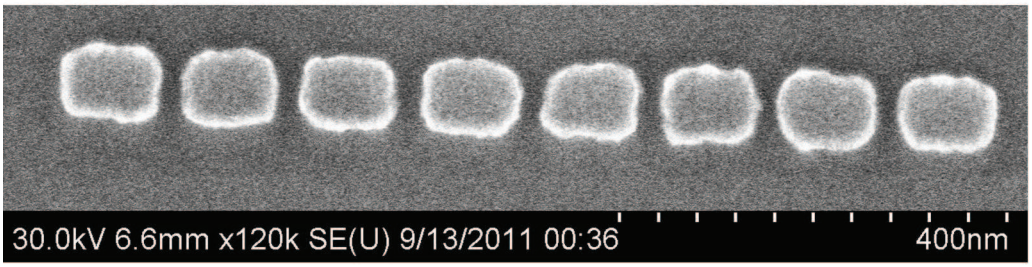

(b)

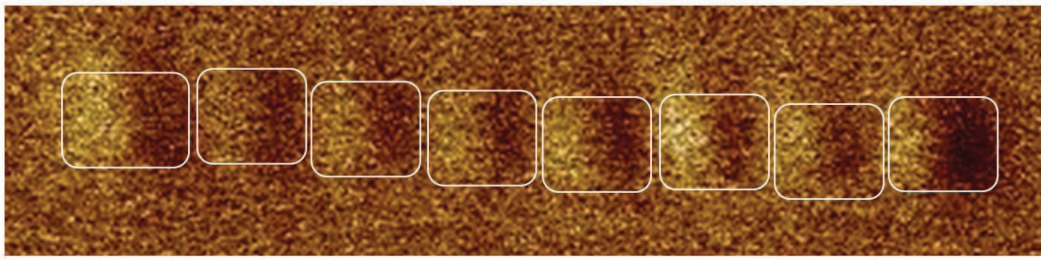

(c)

Figure 6.7: (a) Schematic diagram of a ferromagnetic wire architecture with eight SVBN devices. (b) SEM image of a ferromagnetic wire architecture with eight SVBN devices. (c) MFM image of a ferromagnetic wire architecture with eight SVBN devices.

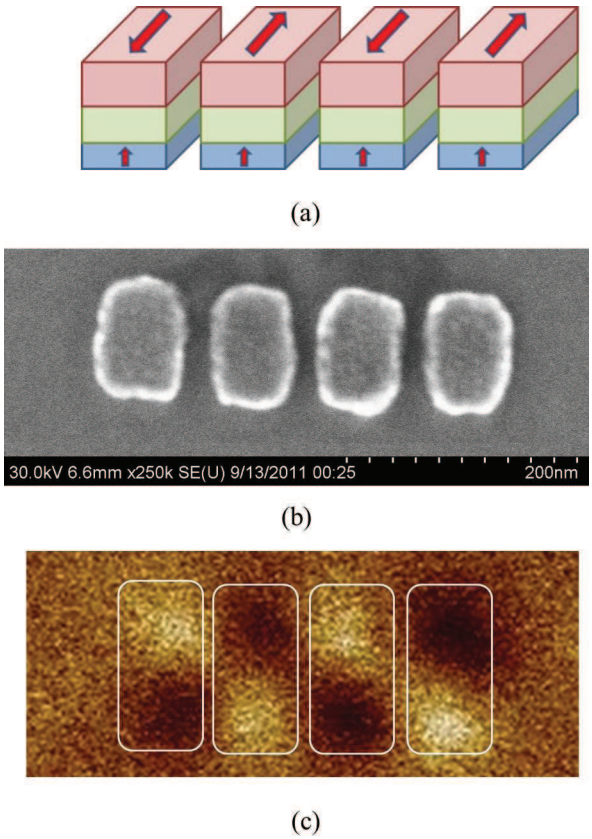

Figure 6.8: (a) Schematic diagram of an antiferromagnetic wire architecture with four SVBN devices. (b) SEM image of an antiferromagnetic wire architecture with four SVBN devices. (c) MFM image of an antiferromagnetic wire architecture with four SVBN devices.

Fig. 6.8(b) has a similar value to the ones in Table. 6.1. The MFM image in Fig. 6.8(c) reveals perfect antiferromagnetic alignment in all the top layers of the SVBN devices in the antiferromagnetic wire architecture, meaning that the antiferromagnetic wire architecture has propagated the information correctly from one end to the other.

The antiferromagnetic wire architecture with four SVBN devices was extended to an antiferromagnetic wire architecture with eight SVBN devices. The schematic of the antiferromagnetic wire architecture with eight SVBN devices is shown in Fig. 6.9(a). The SEM image in Fig. 6.9(b) shows the fabricated antiferromagnetic wire architecture with eight SVBN devices. The average dimensions of the SVBN devices in the antiferromagnetic wire architecture were about 100 *nm*

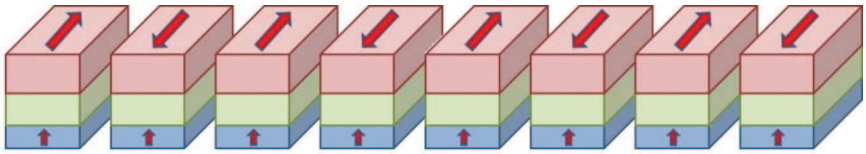

(a)

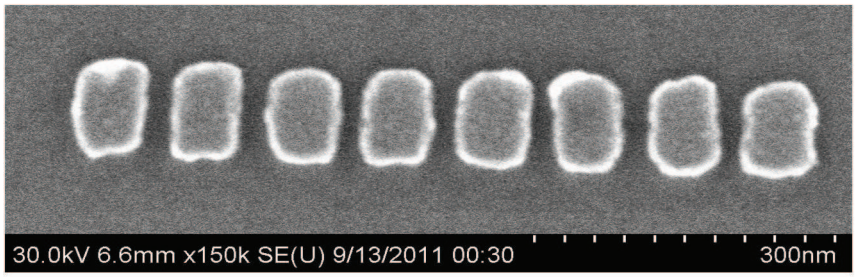

(b)

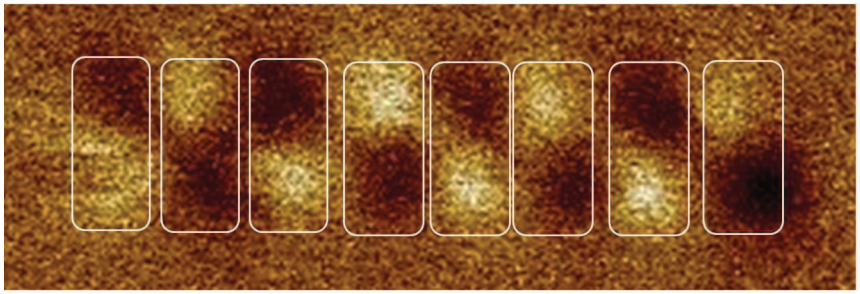

(c)

Figure 6.9: (a) Schematic diagram of an antiferromagnetic wire architecture with eight SVBN devices. (b) SEM image of an antiferromagnetic wire architecture with eight SVBN devices. (c) MFM image of an antiferromagnetic wire architecture with eight SVBN devices.

x 50 *nm* and the spacing between the nearest neighbor was about 20 *nm*. We have assumed that the thickness of each layer in the SVBN devices in Fig. 6.9(b) has a similar value to the ones in Table. 6.1. The MFM image in Fig. 6.9(c) reveal perfect antiferromagnetic alignment in all the top layers of the SVBN devices in the antiferromagnetic wire architecture, meaning that the antiferromagnetic wire architecture has propagated the information correctly from one end to the other.

The schematic diagram in Fig. 6.10(a) shows a three-input majority logic gate with four SVBN devices. The SEM image in Fig. 6.10(b) shows the fabricated three-input majority logic gate with

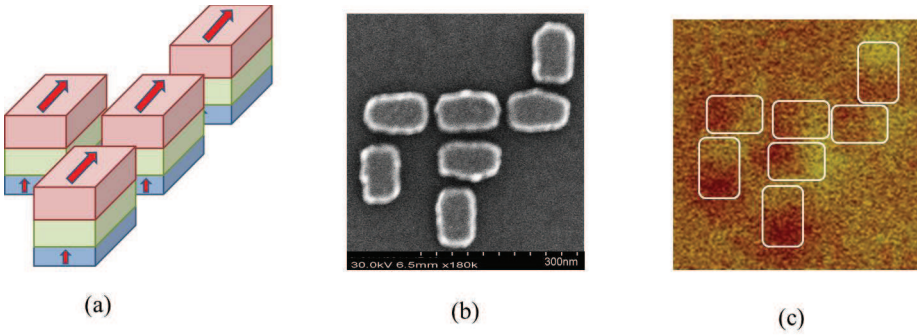

Figure 6.10: (a) Schematic diagram of three-input majority logic gate with four SVBN devices. (b) SEM image of three-input majority logic gate with four SVBN devices and three drive SVBN device. (c) MFM image of three-input majority logic gate with four SVBN devices and three drive SVBN device.

four SVBN devices and three driver SVBN devices to provide input. The average dimensions of the SVBN devices in the three-input majority logic gate were about 100 *nm* x 50 *nm* and the spacing between the nearest neighbor was about 20 *nm*. The MFM image in Fig. 6.10(c) reveal the expected magnetic alignment in all the top layers of the SVBN devices in the three-input majority logic gate, meaning that the three-input majority logic gate has computed the correct output.

6.6 Conclusion

In this chapter, we have proposed and experimentally demonstrated a multilayer nano-magnetic device that can potentially address the write and clock issues in conventional single layer nano-magnetic devices. The experimental observation concludes that the free layers of the SVBN devices functioned similarly to the three-input majority logic gate [40] and the ferromagnetic and anitferromagnetic wire [88] architectures with single layer nano-magnetic devices. These exciting results can lead us to fabricate complex SVBN architectures for computing paradigms. By connecting access transistors to the SVBN device we can convert electrical signals to magnetic signals and vice versa. Fig. 6.11 shows schematic diagrams of SVBN and MOSFET, hybrid configuration of a ferromagnetic wire, antiferromagnetic wire and a three-input majority logic gate. We can use

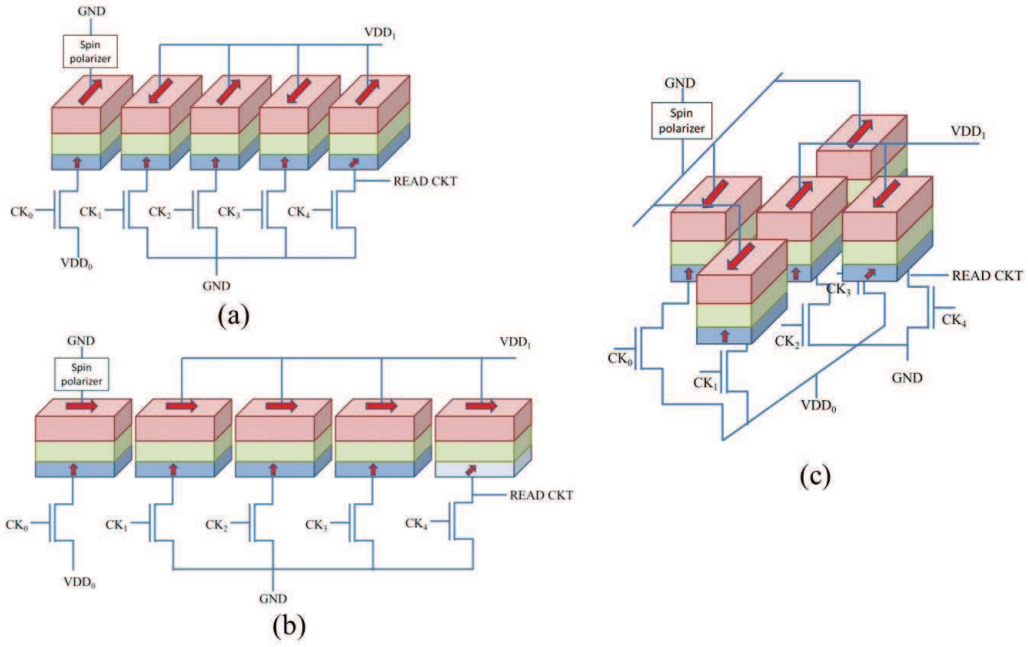

Figure 6.11: Schematic diagrams of SVBN and MOSFET hybrid devices. (a) Ferromagnetic wire architecture. (b) Antiferromagnetic wire architecture. (c) Three-input majority logic gate.

spin polarized current to write data on the top layer of the input SVBN device and use spin transfer torque to clock the devices. Engineering the bottom layer of the output SVBN device to have a tilted magnetization [71] allows us to read the device by giant magnetoresistance (GMR). With the aid of these hybrid devices we can achieve long-term reliable computation [20].

Chapter 7: Experimental Demonstration of Non-Boolean Computing with Nano-Magnetic Disks: Perceptual Organization In Computer Vision

Identifying salient features in a picture is a simple task for the human brain. However, for a computer that uses traditional Boolean arithmetic computation methods, it is a tedious task. In the numerous steps that are involved in identifying the salient features in an image, the most time and resource consuming step is the quadratic optimization process, or perceptual organization step. In this research, we have experimentally demonstrated a magnetic system that would ease this task for a computer. We have harnessed the energy minimization nature of magnetic systems to solve the quadratic optimization problem, especially those arising in computer vision applications. We have fabricated a magnetic system corresponding to an image and have identified salient features with more than 85% true positive rate. These experimental results feature the potentiality of this unconventional computing method to develop a magnetic processor which solves such complex problems in few clock cycles.

This unconventional computing method was first proposed by Dr. S. Sarkar and Dr. S. Bhanja in [93, 94]. They had a vision to develop a magnetic processor that is similar to the one in Fig. 7.1, to solve perceptual organization problems. The compiler for this processor would process the image and identify all the edge segments and map each edge segment to a unique nano-magnetic disk in the two-dimensional array of nano-magnetic disks. The magnetization of the unselected nano-magnetic disks in the two-dimensional array would be driven into a non-computing state. This mechanism isolates a cluster of nano-magnetic disks that represent edge segments in an edge image. Finally, the computing nano-magnetic disks in the array would be clocked into a computing state and would

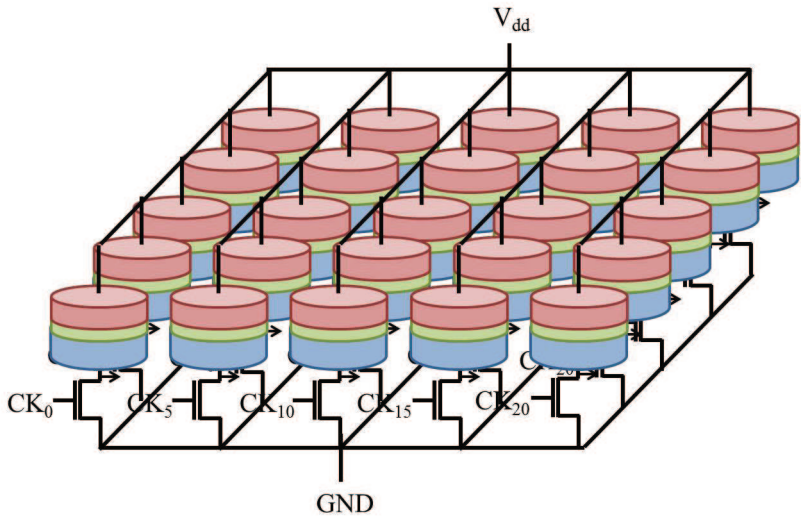

Figure 7.1: Magnetic processor.

allow the array to relax to an energy minimum. The final magnetization states of the nano-magnetic disks would be the solution for the quadratic optimization process (perceptual organization).

The initial experimental work supporting this idea was carried out Dr. J. Pulecio and his work can be found in his Ph.D. dissertations [85]. The work in this chapter is a continuation of Dr. J. Pulecio′s experimental work to prove the viability of using a magnetic system to solve perceptual organization problems. The design principles used for the nano-magnetic disks in this chapter can be found in Dr. A. Kumai′s Ph.D. dissertations [50]. A detailed description of the simulation and theoretical work supporting the experimental work in this chapter can be found in S. Rajaram′s and R. Panchumarthy′s Ph.D. dissertations, respectively.

7.1 Background

In recent years magnetic nano-structures have been widely used and researched for memory applications [82]. Information is encoded as magnetization states and it remains without power, eliminating static power dissipation. For memory applications it is important to isolate each device

to minimize the magnetic interaction among neighboring devices to preserve information. However, this magnetic interaction between neighboring magnets can be exploited for informational computation. Cowburn *et al.* [17] were the first to experimentally demonstrate logic operation and information propagation at room temperature using a magnetic system. Next, Imre *et al.* [40] designed a nano-magnetic logic architecture and experimentally demonstrated a universal logic gate that can compute the majority of three Boolean inputs or even operate as a NOR or NAND gate by fixing the third input to either logic 1 or 0. Karunaratne *et al.* [44] have used ferromagnetic and antiferromagnetic wires [88] to connect three universal logic gates [40] to construct the largest reconfigurable nano-magnetic logic architecture to compute the majority of seven Boolean variables. Since all the above nano-magnetic logic architectures were designed as an enhancement for complementary metal-oxide-semiconductor (CMOS) devices, it seeks to replicate traditional computing involving Boolean logic and arithmetic operations. Nano-magnetic logic architectures compute information by minimizing their total magnetization energy. For example, the three-input majority logic gate designed by Imre *et al.* [40] has a central nano-magnetic device which is driven to an energy minimum state by its surrounding nano-magnetic devices. This energy minimizing nature of magnetic systems can be directly harnessed to solve quadratic optimization problems which arise in many computer vision applications such as motion segmentation [81], correspondence [66], figure-ground segmentation [75], clustering [101], grouping [97], subgraph matching [110] and digital graph matching [58]. In this chapter, we have focused on one such vision problem, which is grouping important features. This task of grouping important features is known as "perceptual organization".

Analyzing and identifying the interesting parts of an image is known as "feature recognition" in computer vision [96]. To accomplish this task the digital image is subjected to four stages of image processing. We have shown an example in Fig. 7.2 of the four stages involved in feature recognition via traditional computing. The first stage of feature recognition involves the detection of the boundaries between the contrast differences in the image in Fig. 7.2(a). These boundaries are known as edge segments and they can be found through an edge detection algorithm. The edge segments in Fig. 7.2(b) of the image in Fig. 7.2(a) are found by the Canny edge detection

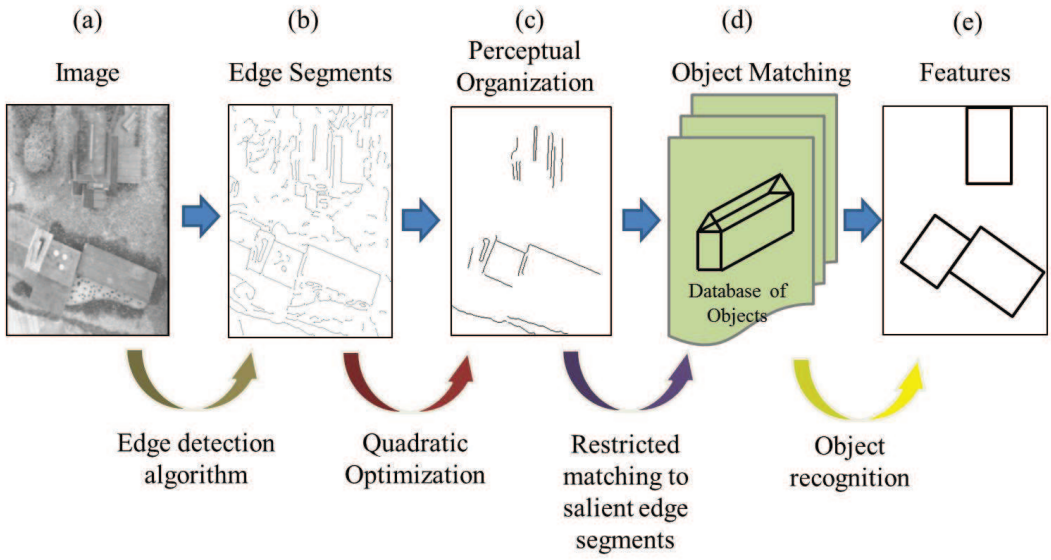

Figure 7.2: Feature recognition using traditional computing.

algorithm [10]. The algorithm has five separate processing steps: smoothing, finding gradients, non-maximum suppression, double thresholding and edge tracking by hysteresis. The clarity of the edge image is dependent on the thoroughness of these steps. As one can see there are many edge segments in the edge image in Fig. 7.2(b) which some of the edge segments belong to objects of interest and the others are from the background. We exploit the fact that there is a structure and organization in the world. Objects in the world tend to exhibit high level of symmetry, parallelism, convexity and coherence. These properties were known to be important in human perception and are known as Gestalt psychology [98]. The main objective in this computer vision problem is to identify the edge segments that belong to objects in the scene and to filter out the edge segments that belong to the background. The second stage in feature recognition involves the identification of the edge segments that belong to objects of interest and the filtering of the edge segments that belong to the background. For this task each pair of edge segments is associated with a pairwise affinity value capturing its saliency. For example, if two edges are parallel to each other, then according to the Gestalt principle [86, 95] they are likely to belong to one object and hence the affinity should be high. Similarly, edge segments that are close together are likely to be associated according to

the Proximity principle [86, 95] and lines that form one straight arrangement are also likely to be grouped according to the Continuity principle [86, 95]. To calculate the pairwise affinity value between two edge segments there are many quantitative forms of affinity functions, but qualitatively they capture similar aspects. The form defined in [97] captures the pairwise affinity, a_{ij}, of the i^{th} and j^{th} edge segment in an edge image and this form has been used to find the pairwise affinity values of the edge segments in Fig. 7.2(b). This form captures the saliency between edge segments that are parallel, perpendicular, connected and overlapped. The particular form in [97] is expressed as:

$$a_{ij} = \sqrt{l_i l_j} exp^{-\frac{o_{ij}}{max(l_i,l_j)}} exp^{-\frac{d_{min}}{max(l_i,l_j)}} cos^2(2\psi_{ij}) \tag{7.1}$$

where l_i and l_j are the lengths of the i^{th} and j^{th} edge segments respectively. ψ_{ij}, o_{ij} and d_{min} are the angle, overlap and the minimum distance between the i^{th} and j^{th} edge segments respectively. As one can see from Eqn. 7.1, the pairwise affinity between two edge segments would be high for segments that are long and continuous, or overlap each other, or are close to each other, or are either parallel or perpendicular to each other.

Once all the pairwise affinity values are calculated between all edge segments, the next task in the second stage is to find the minimum number of edge segments that maximize the total affinity value of the edge image. This task is accomplished though a quadratic optimization process and is mathematically expressed as:

$$\sum_{i=1}^{N} \sum_{j=i+1}^{N} a_{ij} x_i x_j + \left(b \left(\sum_{i=1}^{N} x_i \right) + k \right) \tag{7.2}$$

where a_{ij} is the pairwise affinity value between the i^{th} and j^{th} edge segment. The pairwise affinity value captures the parallelism, proximity and connectivity between two edge segments and we have used the form defined in [97]. x_i takes the binary value of 1 if the edge segment is in a salient group or else it takes the value of 0. N is the total number of edge segments in the image. b is a constant and k is the size of a salient group. To solve the quadratic optimization process for the edge image in Fig. 7.2(b), the researchers have used simulated annealing [48]. The perceptual

organization of the edge image in Fig. 7.2(b) is shown in Fig. 7.2(c). This is a hard problem to solve using traditional Boolean logic based architecture. A conventional compiler would break this quadratic optimization problem into multiple steps of basic arithmetic and logic operations, thereby increasing the computational time as well as the usage of hardware resources. The third stage of feature recognition involves the restricted matching between a model database and the perceptual organization. This model data base is a collection of the objects of interested. The final stage of feature recognition involves the identification and placement of the objects of interested in the image.

In this method of feature recognition via traditional Boolean logic and arithmetic based computation, the most tedious part is the quadratic optimization process. The quadratic optimization process is an unconstrained optimization problem with a non-convex object function, which is currently solved using a simulated annealing [48] or graph cuts method [8]. Typically, these methods involve multiple iterations and each iteration involves many arithmetic operations, which are computationally intensive for traditional logic based computing platform. The time taken to compute the solution for the quadratic optimization process is proportional to the number of edge segments detected in an image, which can be very large. In this chapter, we have experimentally demonstrated a non-Boolean computation method with a magnetic system made of nano-magnetic disks that could ease the task of perceptual grouping.

Nano-magnetic disks based computation offer a tantalizing alternative to traditional logic based digital computing for solving quadratic optimization problems, drastically reducing the computational time and hardware resources. When a collection of nano-magnetic disks are driven to an excited state and relaxed they tend to settle to an energy minimum state. The form of this magnetic energy optimization function is quadratic and is dependent on the relative distance between the nano-magnetic disks. Since perceptual organization is also an error-tolerant application (cost for not finding the optimal solution is not high) [97] it makes perfect sense to use nano-magnetic disks as computing elements [86].

The basic computing elements in the magnetic system are nano-magnetic disks which are made of a soft ferromagnetic material. If we map the edge segments in an edge image to the nano-

magnetic disks in a magnetic system and then stimulate the magnetic system with an external magnetic field followed by a relaxation process allowing the system to settle to an energy minimum, the solution for the quadratic optimization process (perceptual organization) lies in the total magnetic energy in the magnetic system. The perceptual organization of the image can be easily found by identifying the magnetically strongly coupled nano-magnetic disks and then finding the corresponding edge segments.

Sarkar *et al.* [93] were the first to propose this unconventional non-Boolean computation using quantum-dot cellular automata to solve quadratic optimization problems. In [94], Sarkar *et al.* have simulated a magnetic system to solve a quadratic optimization problem. The basic computing elements in the simulated magnetic system was nano-magnetic pillars with an out-of-plane magnetization. The edge segments in the edge image were represented with nano-magnetic pillars. The relative placements of the nano-magnetic pillars were based on the pairwise affinity values. Sarkar *et al.* have used a well-known information visualization technique in statistical analysis to convert the edge segments to nodes and the pairwise affinity values to distance between the nodes, which resulted in forming a distance map. Once the magnetic system was configured based on the distance map it was stimulated with an external magnetic field and relaxed allowing a magnetic computation to take place. When the system reached its energy minimum, magnetic measurements of the out-of-plane magnetic component were taken. The nano-magnetic pillars with the largest out-of-plane magnetic components were grouped and the respective edge segments were selected as perceptually most salient. Pulecio *et al.* [86] fabricated a magnetic system with nano-magnetic disks that had an in-plane magnetization to solve a quadratic optimization problem. The system had five nano-magnetic disks that represented five edge segments. Pulecio *et al.* also used the same mapping method as Sarkar *et al.* in [93] to map the edge segments to nano-magnetic disks. Once the magnetic system was fabricated, stimulated and relaxed magnetic measurements were taken by a magnetic force microscope (MFM) and coupling strength among the nano-magnetic disks was measured through the probe-sample interaction. The strongly coupled nano-magnetic disks were not easily influenced by the probe whereas the weakly coupled nano-magnetic disks were. This

mechanism enabled Pulecio *et al.* to identify a set of strongly coupled nano-magnetic disks that represented a group of edge segments that were perceptually most salient.

As it was evident from Pulecio *et al.* work in [86], it is difficult to experimentally obtain a quantitative value for the magnetic coupling energy between two nano-magnetic disks. In this research, we have used a qualitative method to experimentally identify the strongly coupled nano-magnetic disks in the magnetic system once it has been stimulated with an external magnetic field and then removed allowing the magnetic system to relax to an energy minimum. We have exploited the two stable magnetization states, that is, single domain state and vortex state of nano-magnetic disks, to identify the strongly coupled nano-magnetic disks in the magnetic system.

7.2 Magnetization States in a Nano-Magnetic Disk

Nano-magnetic disks with nanoscale dimensions exhibit two stable magnetization states depending on their internal magnetic energy. The stable magnetization states are the single domain state where all the magnetic spins are aligned in-plane in one direction and the vortex state where the magnetic spins have a curling configuration. Fig. 7.3 (a) and (b) shows a schematic of the spin alignment and an MFM image of a nano-magnetic disk in the single domain state. In an MFM image a nano-magnetic disk in the single domain state is recognized by the semicircular bright and dark contrasts [15, 102, 113] (see Fig. 7.3 (b)). Fig. 7.4 (a) and (b) shows a schematic of a the spin alignment and an MFM image of a nano-magnetic disk in the vortex state. In an MFM image a nano-magnetic disk in the vortex state is recognized by the bright or dark contrasted spot at the center of the disk [15, 102, 113] (see Fig. 7.4 (b)).

The single domain state energy for a nano-magnetic disk is determined by the magnetostatic demagnetizing energy [37, 43] and the vortex state energy is determined by the exchange energy, anisotropy energy and demagnetization energy [37, 43]. For an isolated nano-magnetic disk these energies are a function of its material properties and its dimensions. If the single domain state energy is greater than the vortex state energy then the preferred magnetization is vortex state, whereas if the

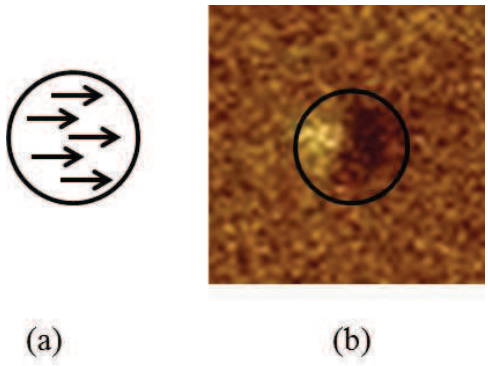

Figure 7.3: (a) Schematic diagram of a nano-magnetic disk in the single domain state. (b) MFM image of a nano-magnetic disk made from Permalloy with a diameter of 110 nm and thickness of 8 nm.

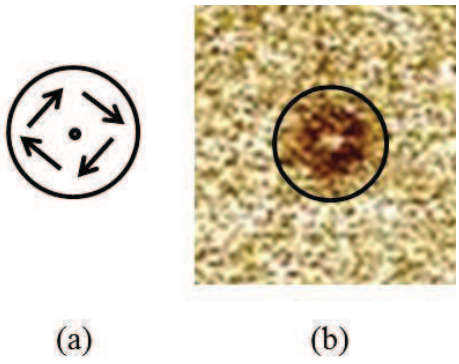

Figure 7.4: (a) Schematic diagram of a nano-magnetic disk in the vortex state. (b) MFM image of a nano-magnetic disk made from Permalloy with a diameter of 110 nm and thickness of 15 nm.

vortex state energy is greater than the single domain state energy then the preferred magnetization is single domain state. Cowburn *et al.* [16] have fabricated isolated nano-magnetic disks of diameters ranging from 55 *nm* to 500 *nm* and thickness ranging from 6 *nm* to 15 *nm*, and have experimentally identified a phase diagram between vortex state and single domain state. In [27, 37, 43, 51, 99] the authors have reported a phase diagrams as a function of the disk diameter and thickness between single domain state and vortex state for isolated nano-magnetic disks. At the boundary between the two phases the single domain state energy is equal to vortex state energy. For the magnetic system we have proposed and designed, we have chosen a diameter and thickness for the nano-magnetic disks towards the close vicinity of phase boundary in the vortex state region. If we apply an external magnetic field in the in-plane direction for the nano-magnetic disks in this region, then the magnetic spins in the nano-magnetic disk would align with the external magnetic field resulting in a single domain state. Once the external magnetic field is removed the magnetic spins would relax to their original curling configuration. This external magnetic field can be in the form of stray fields of neighboring nano-magnetic disks. If the magnetic stray fields are strong enough, then the nano-magnetic disk would remain in a single domain state whereas if the magnetic stray fields were weak, then the magnetization of the nano-magnetic disk would settle back to vortex state.

This phenomenon was validated by micromagnetic simulation experiments conducted by S. Rajaram. Next, the micromagnetic simulation experiments were extended to two nano-magnetic disks to observe a relationship between the magnetic coupling energy and the magnetization states of the nano-magnetic disks. A detailed description of the simulation experiments can be found in S. Rajaram′s Ph.D. dissertation. Analyzing the simulation data in [90], we have concluded that when both the nano-magnetic disks are in single domain state the coupling energy has a high value and when both the nano-magnetic disks are in vortex state the coupling energy has minimal value. To identify the strongly coupled nano-magnetic disks with critical dimensions in a magnetic system we have used this qualitative method.

To solve the perceptual organization problem with a magnetic system comprised with nano-magnetic disks that exhibit single domain state and vortex state magnetization states for the same geometry, it is important to find the correspondence between the magnetic hamiltonian (an energy

expression for the magnetic system) and the quadratic optimization process. To develop the magnetic Hamiltonian, we need to represent the multiple magnetization states of a nano-magnetic disk with single continuous variable. For this task, we have proposed a magnetization state vector model (a vector model) that represents the magnetization states of a nano-magnetic disk.

7.3 Magnetization State Vector Model

In the magnetization state vector model, the magnetization states of a nano-magnetic disk is represented with a vector. The magnetization inside a nano-magnetic disk is represented with a vector field. The vector field has a curling formation around its vortex center. As the vectors in the vector field approach closer to the vortex center they gradually change from the in-place direction to the out-of-plane direction. The disk center of a nano-magnetic disk could be on or in between the vortex center and a point that is at an infinite distance. If the disk center was at an infinite distance the vector field in the nano-magnetic disk would have a unidirectional in-plane formation whereas if the disk center was on the vortex center the vector field would have a curling formation around the nano-magnetic disk center. In the curling formation, while the vector field is spinning around the disk center, it also gradually changes from the in-plane direction to the out-of-plane direction as it gets closer to the disk center (vortex center) from the disk circumference. If the vortex center was at a point in between the disk center and an infinite point the vector field would have a C-formation. Thereby the magnetization state of a nano-magnetic disk could be represented by a vector that is pointing from the vortex center to the disk center.

In the magnetization state vector model, the nano-magnetic disk is segmented into magnetic elements and the magnetization of each magnetic element is represented with a single vector (magnetic vector - $\boldsymbol{M} = m_i\boldsymbol{i} + m_j\boldsymbol{j} + m_k\boldsymbol{k}$). We have assumed that as long as the size and the material of the magnetic elements in a nano-magnetic disk are similar, the magnitude of the magnetization will remain constant but the direction of the magnetic vector will vary along the normal plane to the line segment connecting the magnetic element and the vortex center. We have modeled a magnetic

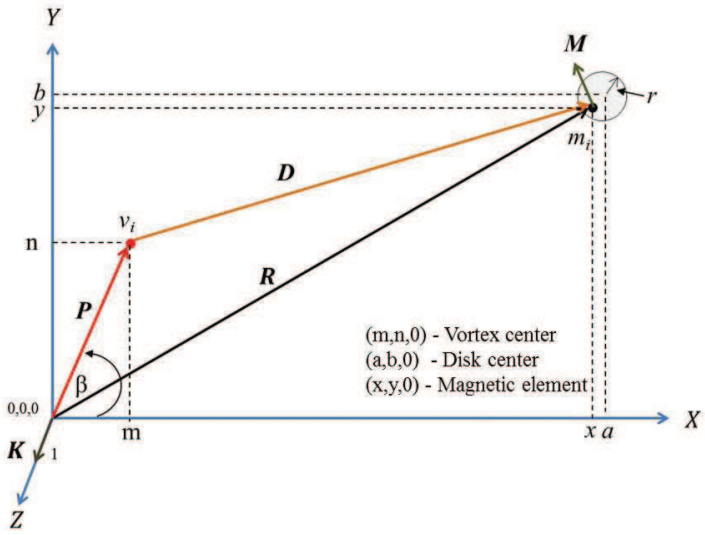

Figure 7.5: Vector diagram of a magnetic element m_1 and vortex center v_1 of the magnetic vector ***M***. The black dot represents the magnetic element and the red point represents the vortex center.

vector of a magnetic element that is at an infinite distance away from its vortex center to have an in-plane direction (the ***k***-component of the magnetic vector will be zero). As the magnetic element gets closer to the vortex center the ***k***-component of the magnetic vector exponentially increases. The magnetic element at vortex center will only have ***k***-component in the magnetic vector (***i***-component and ***j***-component are zero).

The vector diagram in Fig. 7.5 represents the vector notations used for and to derive the magnetization state vector model. The circle in gray in Fig. 7.5 signifies a nano-magnetic disk with its center at point $(a,b,0)$ and a radius of r. The black dot on the circle signifies a magnetic element, m_i, at the point $(x,y,0)$ and it is represented with the vector ***R***. The vector ***M*** represents the magnetization of the magnetic element. The vector ***M*** has its vortex center, v_i, at the point $(m,n,0)$ and it is represented with the vector ***P***. The vector from the vortex center v_i to the magnetic element m_i is represented by the vector ***D***. The vector ***K*** starts at point $(0,0,0)$ and is a unit vector in the Z-axis direction.

The vectors in Fig. 7.5 are expressed as:

$$\boldsymbol{R} = x\boldsymbol{i} + y\boldsymbol{j} + 0\boldsymbol{k} \tag{7.3}$$

$$\boldsymbol{P} = m\boldsymbol{i} + n\boldsymbol{j} + 0\boldsymbol{k} \tag{7.4}$$

where

$$m = |\boldsymbol{P}| cos\ \beta \text{ and } n = |\boldsymbol{P}| sin\ \beta$$

$$\boldsymbol{D} = \boldsymbol{R} - \boldsymbol{P} \tag{7.5}$$

$$\boldsymbol{D} = (x - (|\boldsymbol{P}| cos\ \beta))\ \boldsymbol{i} + (y - (|\boldsymbol{P}| sin\ \beta))\ \boldsymbol{j} + 0\boldsymbol{k} \tag{7.6}$$

$$\boldsymbol{K} = 0\ \boldsymbol{i} + 0\ \boldsymbol{j} + \boldsymbol{k} \tag{7.7}$$

The vector $\boldsymbol{m}$ is defined as the unit vector of $\boldsymbol{M}$.

$$\boldsymbol{m} = \frac{\boldsymbol{M}}{|\boldsymbol{M}|} \tag{7.8}$$

The unit magnetic vector $\boldsymbol{m}$ is expressed as:

$$\boldsymbol{m} = a\ \boldsymbol{K} + b\ \left(\frac{\boldsymbol{K} \times \boldsymbol{D}}{|\boldsymbol{K}||\boldsymbol{D}|}\right) \tag{7.9}$$

where

$$a^2 + b^2 = 1$$

We have modeled the amplitude a of the unit vector $\boldsymbol{m}$ to be an inverse exponential to the magnitude of vector $\boldsymbol{D}$. The amplitude a is then expressed as:

$$a = e^{\frac{-|\boldsymbol{D}|}{\tau}} \tag{7.10}$$

where τ is the distance along the vector $\boldsymbol{D}$ and it is a constant.

To keep the magnitude of the unit vector $\boldsymbol{m}$ unity, we have reduced the amplitude of the vector $\left(\frac{\boldsymbol{K}\times\boldsymbol{D}}{|\boldsymbol{K}||\boldsymbol{D}|}\right)$ by factor of b. The amplitude b is modeled as:

$$b = \sqrt{1 - e^{\frac{-2|\boldsymbol{D}|}{\tau}}} \tag{7.11}$$

Substituting the values of a and b to Eqn. 7.9, we have expressed the unit magnetic vector $\boldsymbol{m}$ as:

$$\boldsymbol{m} = e^{\frac{-|\boldsymbol{D}|}{\tau}}\ \boldsymbol{K} + (\sqrt{(1 - e^{\frac{-2|\boldsymbol{D}|}{\tau}})})\frac{\boldsymbol{K}\times\boldsymbol{D}}{|\boldsymbol{K}||\boldsymbol{D}|} \tag{7.12}$$

The magnetic vector $\boldsymbol{M}$ is expressed as:

$$\boldsymbol{M} = \lambda\boldsymbol{m} \tag{7.13}$$

where λ is based on the size and magnetic material of the magnetic element m_i.

$$\boldsymbol{M} = \lambda\left(e^{\frac{-|\boldsymbol{D}|}{\tau}}\ \boldsymbol{K} + (\sqrt{(1 - e^{\frac{-2|\boldsymbol{D}|}{\tau}})})\frac{\boldsymbol{K}\times\boldsymbol{D}}{|\boldsymbol{K}||\boldsymbol{D}|}\right) \tag{7.14}$$

It is evident from Eqn. 7.14 that the vector $\boldsymbol{M}$ is only dependent on the vector $\boldsymbol{D}$. Therefore, we can predict the magnetization state of a nano-magnetic disk with the magnitude and the direction of vector $\boldsymbol{D}$. (A vector can be expressed as a combination of its magnitude and the angle it makes with the X-axis.) If the magnitude of the vector $\boldsymbol{D}$ is $|\boldsymbol{D}|$ and the angle it makes with the X-axis is θ, then the magnetic vector $\boldsymbol{M}$ is dependent on $|\boldsymbol{D}|$ and θ and could be expressed as:

$$\boldsymbol{M}(|\boldsymbol{D}|,\theta) = \lambda\left(e^{\frac{-|\boldsymbol{D}|}{\tau}}\ \boldsymbol{K} + (\sqrt{(1 - e^{\frac{-2|\boldsymbol{D}|}{\tau}})})\frac{\boldsymbol{K}\times\boldsymbol{D}}{|\boldsymbol{K}||\boldsymbol{D}|}\right) \tag{7.15}$$

Figs. 7.6, 7.7, 7.8 shows the MATLAB simulations of the vector field $\boldsymbol{M}$, for a single domain state, C-state and a vortex state, respectively, in a nano-magnetic disk with its disk center at $(0,0,0)$. (A detailed description of the MATLAB code can be found in R. Panchumarthy′s Ph.D. dissertation.) As predicted when the $|\boldsymbol{D}|$ value was large the vector field was unidirectional and when it

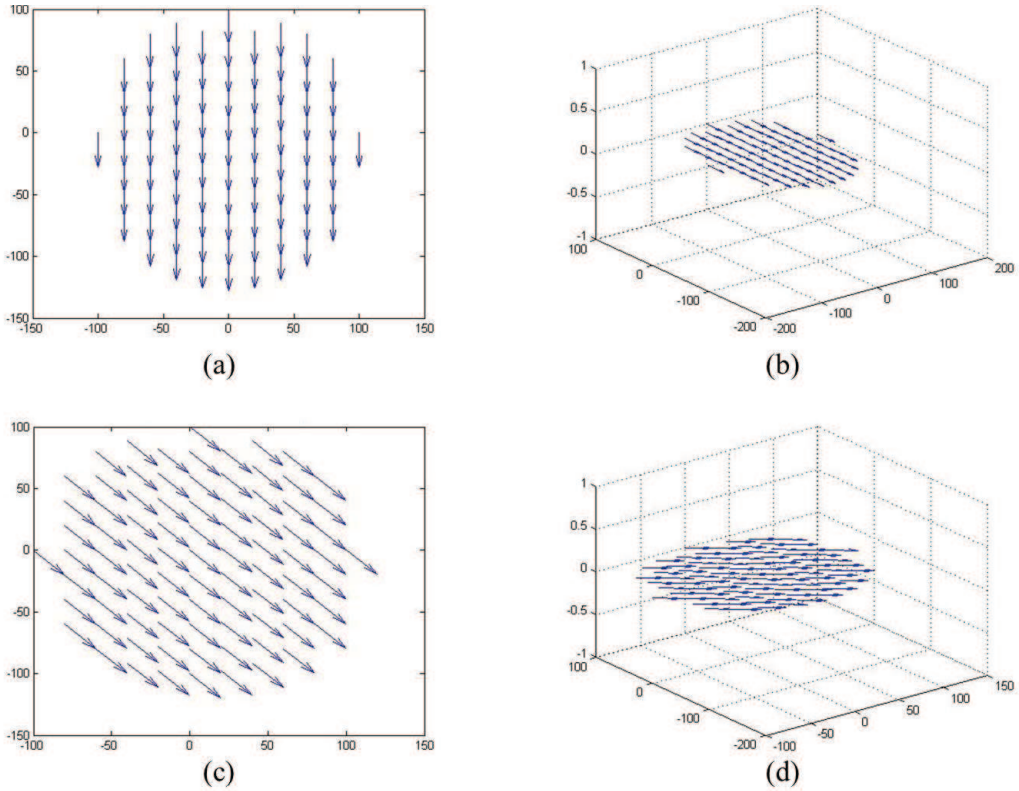

Figure 7.6: Magnetic vector fields of single domain state. (a) Single domain state, ($|\boldsymbol{D}| = \infty$, $\theta = 0$) - 2D plot. (b) Single domain state, ($|\boldsymbol{D}| = \infty$, $\theta = 0$) - 3D plot. (c) Single domain state, ($|\boldsymbol{D}| = \infty$, $\theta = 45$) - 2D plot. (d) Single domain state, ($|\boldsymbol{D}| = \infty$, $\theta = 45$) - 3D plot. (One unit represents 0.5 *nm*.)

was close to the disk center the vector field had a curling formation. Any intermediate value for $|\boldsymbol{D}|$ resulted in a vector field with a C shape formation.

7.4 Design of the Magnetic Layout

The special arrangement of the nano-magnetic disks in the magnetic system is dependent upon the correspondence between the quadratic optimization process and the magnetic hamiltonian of the magnetic system. The magnetic hamiltonian for a magnetic system of this nature, that is, having nano-magnetic disks (same dimensions) with multiple magnetization states depending on

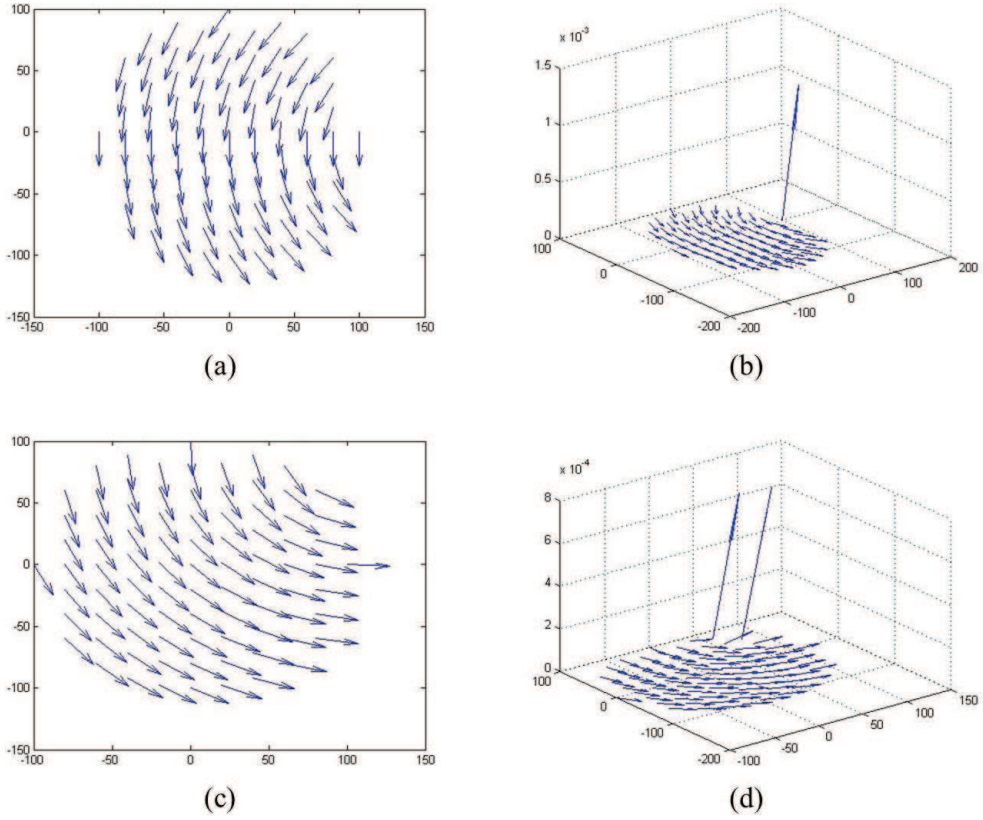

Figure 7.7: Magnetic vector fields of C- state. (a) C-State, ($|\boldsymbol{D}|$ = 150, $\theta = 0$) - 2D plot. (b) C-State, ($|\boldsymbol{D}|$ = 150, $\theta = 0$) - 3D plot. (c) C-State, ($|\boldsymbol{D}|$ = 150, $\theta = 45$) - 2D plot. (d) C-State, ($|\boldsymbol{D}|$ = 150, $\theta = 45$) - 3D plot. (One unit represents 0.5 *nm*.)

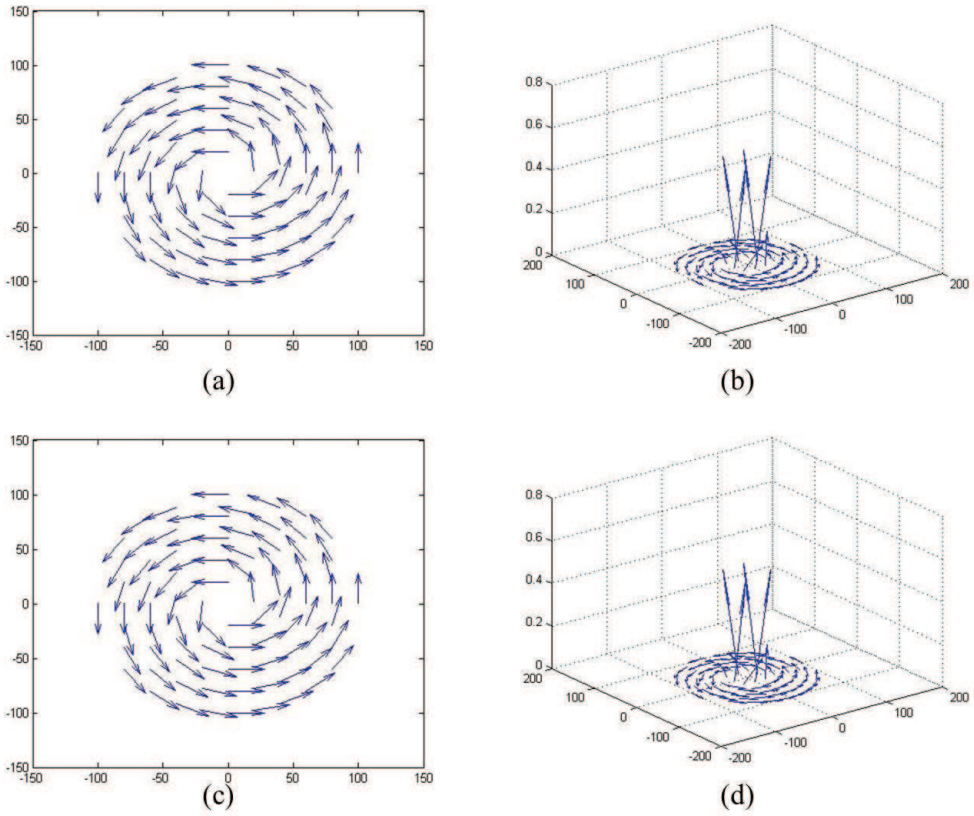

Figure 7.8: Magnetic vector fields of vortex state. (a) Vortex state, ($|\boldsymbol{D}|$ = 0, $\theta = 0$) - 2D plot. (b) Vortex state, ($|\boldsymbol{D}|$ = 0, $\theta = 0$) - 3D plot. (c) Vortex state, ($|\boldsymbol{D}|$ = 0, $\theta = 45$) - 2D plot. (d) Vortex state, ($|\boldsymbol{D}|$ = 0, $\theta = 45$) - 3D plot. (One unit represents 0.5 *nm*.)

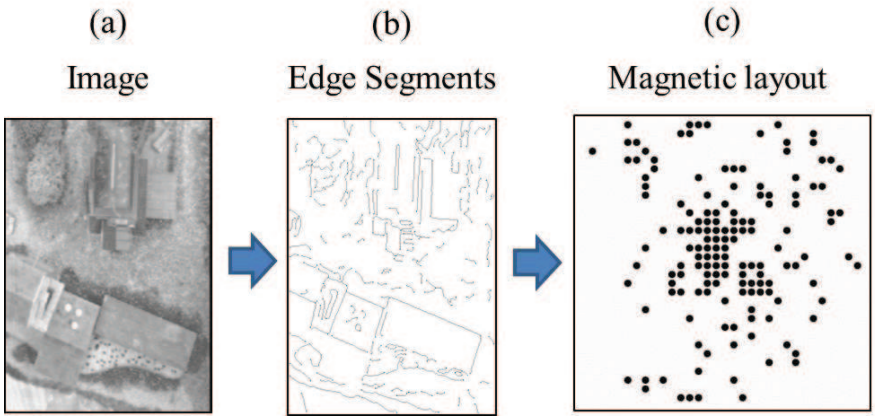

Figure 7.9: (a) Gray scale real world image. (b) Edge image of (a). (c) Distance map of the edge image in (b).

the magnetic coupling energy in the system, was developed by R. Panchumarthy. To develop the magnetic hamiltonian R. Panchumarthy used the concept of the magnetization state representation method from the magnetization state vector model in section 7.3, the simulation data from the simulation experiments carried out by S. Rajaram and the basic micromagnetic theory (dipole energy equation in [70, 119]). A detailed description of the magnetic hamiltonian can be found in R. Panchumarthy′s Ph.D. dissertation.

Based on the correspondence between the magnetic hamiltonian and the quadratic optimization process, Dr. S. Sarkar and Dr. S. Bhanja mapped the edge segments in Fig. 7.9(b) to a configuration of points in a 2D space (distance map). To arrange the nano-magnetic disks in a 2D space they used a well-established information visualization method known as multidimensional scaling (MDS) [1]. The distance map for the edge image in Fig. 7.9(b) can be seen in Fig. 7.9(c). By placing nano-magnetic disks on the 2D points generated by MDS (magnetic layout in Fig. 7.9(c)) and allowing a magnetic computation to take place we can find the solution for the perceptual organization problem. The solution is found by identifying the single domain state nano-magnetic disks in the magnetic system and then by grouping the corresponding edge segments as the salient edge segments.

7.5 Fabrication and Characterization Process

To experimentally validate the unconventional non-Boolean computing method proposed in this chapter, we fabricated magnetic systems that had a similar layout to Fig 7.9(c). Five layouts were designed based on Fig 7.9(c) using DesignCAD 2000NT. The layouts were varied by the disk diameter. The diameter was varied from 105 *nm* to 145 *nm* in steps of 10 *nm* and each layout has 149 disks. The magnetic systems were fabricated on a Silicon wafer. Initially the Silicon wafer was cleaned with an RCA cleaning procedure to remove all organic, ionic, oxide and heavy metal contaminants. The clean Silicon wafer was coated with a uniform layer of 950 Polymethyl methacrylate (PMMA) via a Laurell Technologies WS-400A-8NPP/Lite Spin Processor. The thickness of the PMMA was measured to be approximately 35 *nm*. To achieve this thickness the PMMA was dissolved with Anisole. To remove the unwanted residual solvents on the wafer, the wafer was baked in an oven at $170^{o}C$ for 30 minutes. Once the wafer was cooled down to room temperature the wafer was loaded into a Hitachi SU-70 scanning electron microscope retrofitted with a Nabity NPGS system to expose the patterns. An acceleration voltage of 30 *kV* and a beam current of 25 *pA* were used to expose the layouts of the magnetic systems. The exposed wafer was unloaded and submerged in a Methyl isobutyl ketone/Isopropanol (3:1) developer solution for 60 seconds. The wafer was aerated with Nitrogen and mounted in the chamber of a Varian Model 980-2462 electron beam evaporator to deposit a uniform layer of Permalloy. The evaporation took place in a 2 μTorr vacuum at a rate of 2 $Å s^{-1}$ for 55 seconds resulting with an 11 *nm* uniform film. Subsequently the wafer was removed from the chamber and submerged in a heated Acetone bath for 10 minutes to accomplish the liftoff procedure.

The samples were characterized with the combination of a scanning electron microscope (SEM) and an atomic force microscope (AFM) to identify the defect-free magnetic systems. A defect-free magnetic system was chosen from each layout. The SEM and AFM measurements were used to measure the average diameter and average thickness of the nano-magnetic disks in each magnetic system, respectively. The defect-free samples were then subjected to magnetic force microscopy (MFM) characterizations.

We also fabricated samples with thicknesses varying from 6 *nm* to 18 *nm* and diameters varying from 105 *nm* to 145 *nm*. We observed through MFM characterization the magnetization of the magnetic systems that had nano-magnetic disks with a thickness greater than 14 *nm* to be only in vortex state and nano-magnetic disks with a thickness less than 8 *nm* to be only in single domain state.

7.6 Experimental Setup

For the magnetic systems to compute information it requires stimulation and a relaxation process. To stimulate and relax the magnetic system we provided an external magnetic field in the form of a pulse. To provide the external magnetic field, we used a direct current (DC) electromagnet powered by a 300W DC power supply. To take measurements of the external magnetic field provided to the sample we used a National Institute of Standards and Technology (NIST) calibrated Gauss meter by AlphaLab. The sample was placed in between two opposite magnetic poles in the electromagnet to provide a uniform out-of-plane hard axis external magnetic field. The external magnetic field was ramped up to 80 mT in 0.1 seconds and kept constant for 0.5 seconds followed by a ramp down over 0.1 seconds.

Once the samples were stimulated and allowed to relax to their energy minimums, qualitative magnetic measurements of the magnetic systems were taken from a VEECO DI 300 scanning probe microscope in the MFM mode. A low moment (magnetic moment of $0.3e^{-13}$ EMU) MFM tip was used to take the measurements and to minimize distortion on the magnetic system.

7.7 Results and Discussion

Fig. 7.10 through Fig. 7.14 shows the SEM image, MFM image, magnetization layout and the perceptual organization of the five magnetic systems fabricated. Tables 7.1 through 7.5 shows the

Table 7.1: Performance evaluation of the first magnetic system.

Magnetic System	Avg. thickness of the nano-magnetic disks	Avg. diameter of the nano-magnetic disks	True positive %	False positive %
1	10.7 *nm*	145 *nm*	83	31

average thickness of the nano-magnetic disks in the respective magnetic system, average diameter of nano-magnetic disks in the respective magnetic system, and true positive percentage and false positive percentage of the perceptual organization. Each magnetic system has 149 nano-magnetic disks that corresponded to an edge segment in the edge image in Fig 7.9(b). The average thickness was calculated from the AFM measurements and the average diameter was calculated from the SEM measurements. It is clearly evident from the MFM images that some of the nano-magnetic disks in the magnetic systems have semicircular bright and dark contrast while the others have a bright or dark contrasted spot in the center of the disk. The semicircular bright and dark contrasts represent single domain state whereas the bright or dark contrasted spots represent vortex states [15, 102, 113]. The MFM images were analyzed and the nano-magnetic disks with a single domain state were marked with a red dot and vortex state were marked with a yellow dot on the magnetization layout. The true positive percentage and false positive percentage were computed by comparing the perceptual organizations computed from the magnetic systems and the perceptual organization computed with the traditional computing method in section 7.1 (Fig 7.2). The true positive percentages represent the number of salient edge segments that are correctly identified. The false positive percentages represent the non-salient edge segments identified as salient edges.

Fig. 7.10(a) shows the SEM image of the first magnetic system fabricated. The nano-magnetic disks in the fist magnetic system have an average diameter of 145 *nm* and an average thickness of 10.7 *nm*. Fig. 7.10(c) shows the marked single domain state and vortex state nano-magnetic disks based off the MFM image in Fig. 7.10(b). Fig. 7.10(d) shows the computed salient edge segments by the first magnetic system. The first magnetic system has identified salient features with more than 83% true positive rate. Summary of these results are given in Table 7.1.

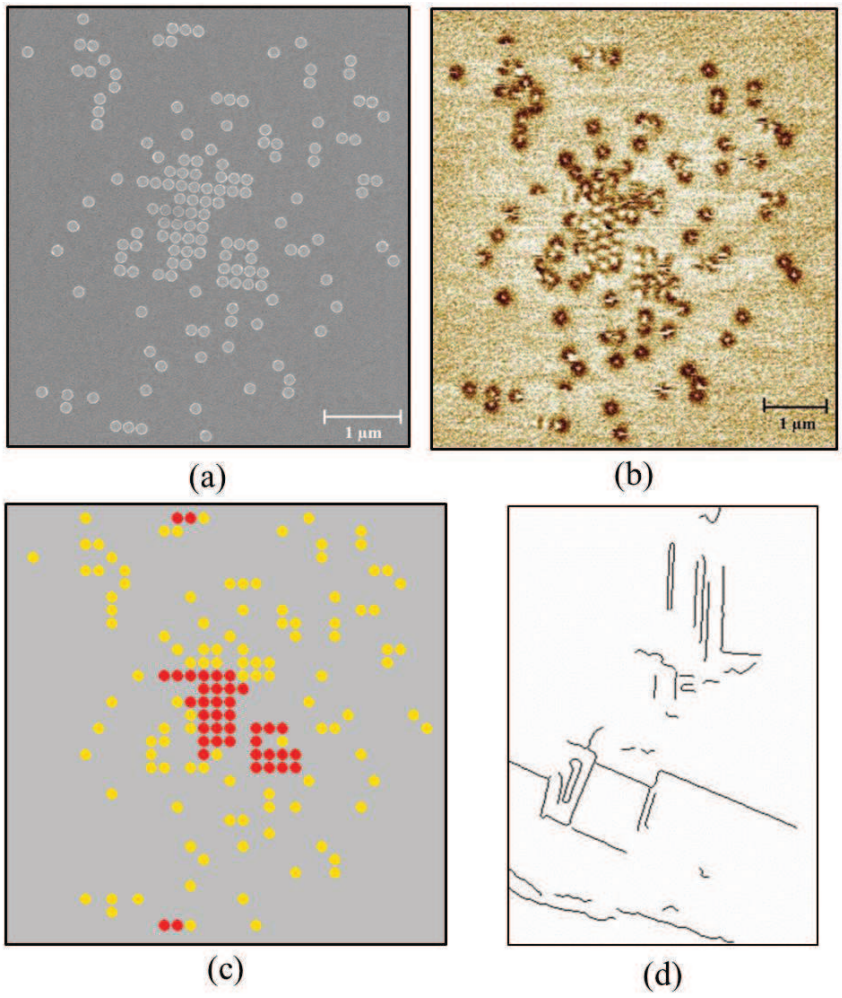

Figure 7.10: (a) SEM images of the first magnetic systems. (b) MFM images of the first magnetic systems. (c) Magnetization state layout (yellow - vortex state and red - single domain state) of (b). (d) Perceptual organization.

Table 7.2: Performance evaluation of the second magnetic system.

Magnetic System	Avg. thickness of the nano-magnetic disks	Avg. diameter of the nano-magnetic disks	True positive %	False positive %
2	11.7 *nm*	137.4 *nm*	86	35

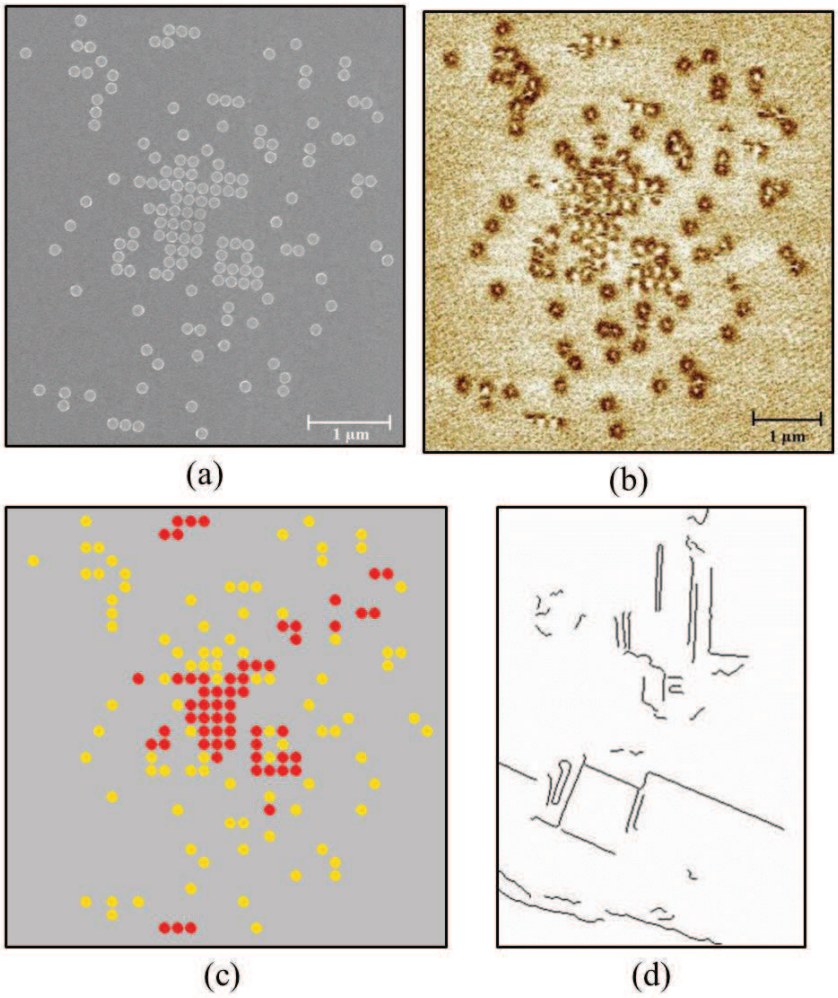

Figure 7.11: (a) SEM images of the second magnetic systems. (b) MFM images of the second magnetic systems. (c) Magnetization state layout (yellow - vortex state and red - single domain state) of (b). (d) Perceptual organization.

Table 7.3: Performance evaluation of the third magnetic system.

Magnetic System	Avg. thickness of the nano-magnetic disks	Avg. diameter of the nano-magnetic disks	True positive %	False positive %
3	11.6 *nm*	129 *nm*	83	39

Table 7.4: Performance evaluation of the fourth magnetic system.

Magnetic System	Avg. thickness of the nano-magnetic disks	Avg. diameter of the nano-magnetic disks	True positive %	False positive %
4	11.3 *nm*	112.2 *nm*	67	34

Fig. 7.11(a) shows the SEM image of the second magnetic system fabricated. The nano-magnetic disks in the second magnetic system have an average diameter of 137.4 *nm* and an average thickness of 11.7 *nm*. Fig. 7.11(c) shows the marked single domain state and vortex state nano-magnetic disks based off the MFM image in Fig. 7.11(b). Fig. 7.11(d) shows the computed salient edge segments by the second magnetic system. The second magnetic system was able recognize salient edge segments with a true positive rate more than 86%. Summary of these results are given in Table 7.2.

The SEM image in Fig. 7.12(a) shows the third magnetic system fabricated. The nano-magnetic disks in the third magnetic system have an average diameter of 129.0 *nm* and an average thickness of 11.6 *nm*. Fig. 7.12(c) shows the marked single domain state and vortex state nano-magnetic disks based off the MFM image in Fig. 7.12(b). Fig. 7.12(d) shows the computed salient edge segments by the third magnetic system. The third magnetic system was able recognize salient edge segments with a true positive rate more than 83%. Summary of these results are given in Table 7.3.

The SEM image in Fig. 7.13(a) shows the fourth magnetic system fabricated. The nano-magnetic disks in the fourth magnetic system have an average diameter of 112.2 *nm* and an average thickness of 11.3 *nm*. Fig. 7.13(c) shows the marked single domain state and vortex state nano-magnetic disks based off the MFM image in Fig. 7.13(b). Fig. 7.13(d) shows the computed salient edge segments by the fourth magnetic system. The fourth magnetic system was able recognize

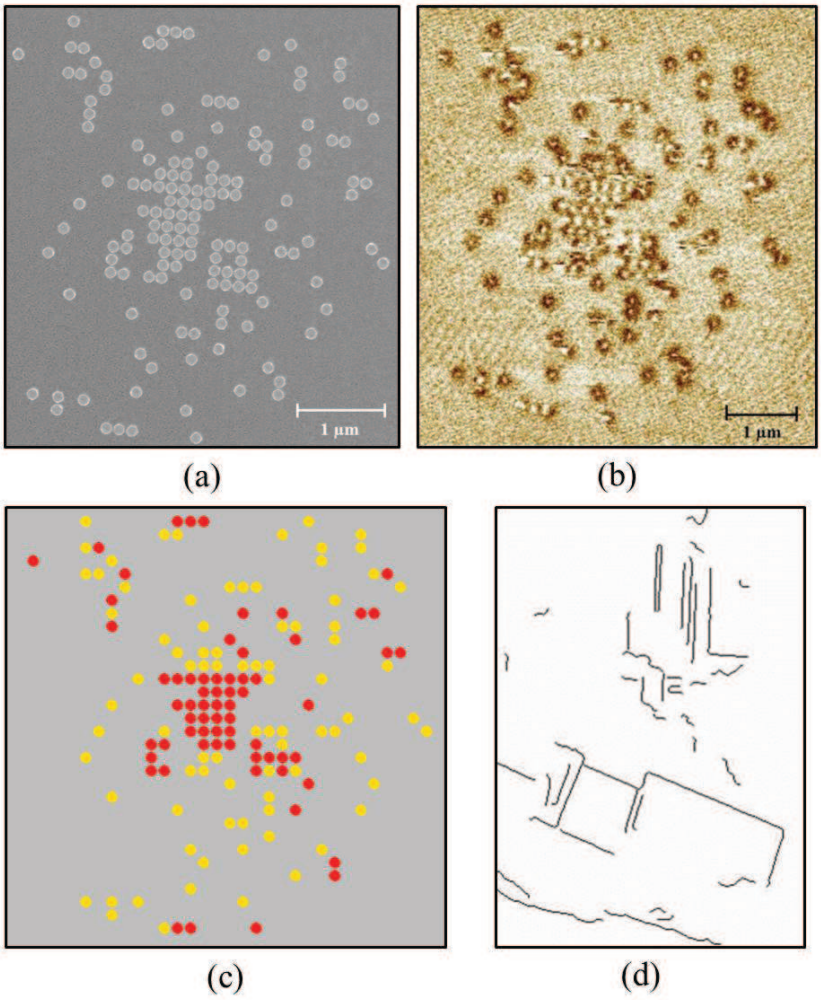

Figure 7.12: (a) SEM images of the third magnetic systems. (b) MFM images of the third magnetic systems. (c) Magnetization state layout (yellow - vortex state and red - single domain state) of (b). (d) Perceptual organization.

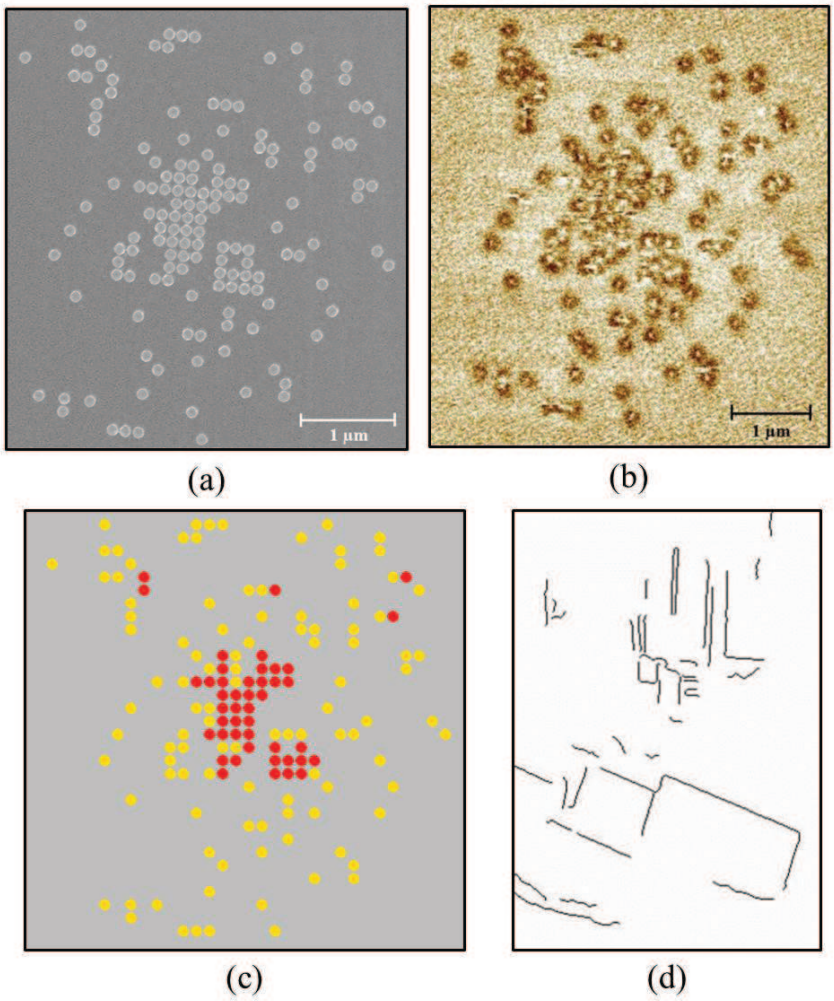

Figure 7.13: (a) SEM images of the fourth magnetic systems. (b) MFM images of the fourth magnetic systems. (c) Magnetization state layout (yellow - vortex state and red - single domain state) of (b). (d) Perceptual organization.

Table 7.5: Performance evaluation of the fifth magnetic system.

Magnetic System	Avg. thickness of the nano-magnetic disks	Avg. diameter of the nano-magnetic disks	True positive %	False positive %
5	10.8 *nm*	103.5 *nm*	83	39

salient edge segments with a true positive rate more than 67%. Summary of these results are given in Table 7.4.

Fig. 7.14(a) shows the SEM image of the fifth magnetic system fabricated. The nano-magnetic disks in the fifth magnetic system have an average diameter of 103.5 *nm* and an average thickness of 10.8 *nm*. Fig. 7.14(c) shows the marked single domain state and vortex state nano-magnetic disks based off the MFM image in Fig. 7.14(b). Fig. 7.14(d) shows the computed salient edge segments by the fifth magnetic system. The fifth magnetic system has identified salient features with more than 83% true positive rate. Summary of these results are given in Table 7.5.

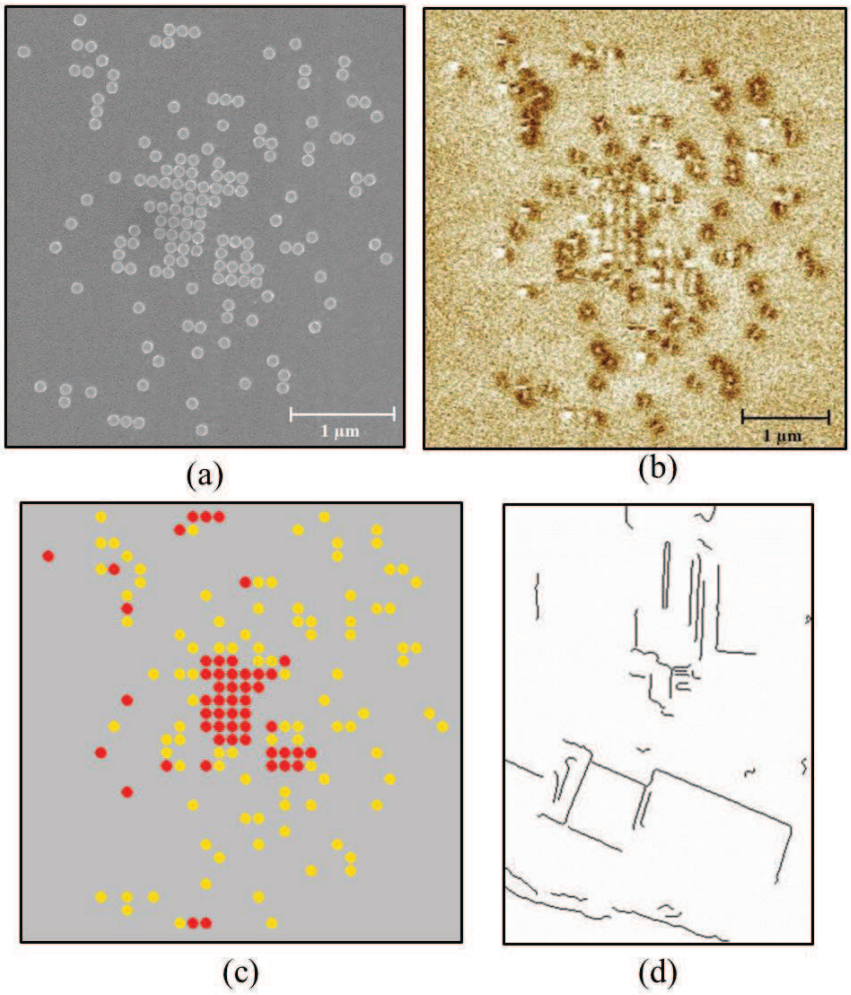

Figure 7.14: (a) SEM images of the fifth magnetic systems. (b) MFM images of the fifth magnetic systems. (c) Magnetization state layout (yellow - vortex state and red - single domain state) of (b). (d) Perceptual organization.

7.8 Conclusion

This research is a proof of concept for the viability of using a magnetic system to solve a quadratic optimization problem. It was evident that the variations in thickness and diameter within the critical dimensions did not affect the final output. This evidence supports the consistency of the magnetic system. Out of the five magnetic systems, four were able to identify 80% or more of the salient edge segments in the image. If the nano-magnetic disks have rough surfaces they will act stubbornly and not couple with the neighboring nano-magnetic disks. In general, the performance of the magnetic systems can be improved through the fabrication process.

We have only fabricated the selected (the node on the distance map) nano-magnetic disks. The actual magnetic processor would be a closely placed two dimensional array of nano-magnetic disks that are integrated with an underlying layer of MOSFET transistors to read/write/ clock each individual disk (see Fig. 7.1). To develop this magnetic processor we first need to fabricate multilayer nano-magnetic disks and observe the same phenomena as in the single layer nano-magnetic disks. Once that is accomplished we need to connect access transistor to write/clock/read the multilayer nano-magnetic disks. This hybrid device allows us to convert electrical signals to magnetic signals and vice versa. The compiler for this processor would process the image and identify all the edge segments and map each edge segment to a unique nano-magnetic disk in the two dimensional array of nano-magnetic disks. The magnetization of the unselected nano-magnetic disks in the two dimensional array would be driven into a non-computing state. This mechanism isolates a cluster of nano-magnetic disks that represent edge segments in an edge image. Finally, the computing nano-magnetic disks in the array would be clocked into a computing state and would allow the array to relax to an energy minimum. The final magnetization states of the nano-magnetic disks would be the solution for the quadratic optimization process (perceptual organization). With this unconventional computing mechanism we have simplified a complex vision computation problem to a single input/output clock cycle.

Chapter 8: Conclusion

Driven by the need for better electronic appliances we have studied nano-magnetic devices as a computational device which has the potential to replace metal-oxide-semiconductor field-effect transistor (MOSFET) technology. The fundamental computational unit of a nano-magnetic device is a single domain magnet that has dimensions in the nano regime. These devices process data by magnetic field interaction with their nearest neighbors and they store data in their magnetization state. Nano-magnetic devices have shown a promise in (i) ultra-low energy stand-by power (ii) room temperature operation (ii) stability over extreme environment (radiation-hardened) (iv) robustness towards thermal noise and (v) instant-on functionality (no booting time). Due to these attractive reasons we have focused the research in this dissertation for the development of nano-magnetic devices as a computation element.

In this work, we have taken an effort to reliably propagate data in a ferromagnetic wire architecture. We experimentally observed that if we need to propagate data from the input cell to the output cell the nano-magnetic device needs to be subjected to a clocking field. This validated the simulation observations by Csaba *et al.* [18]. Subjecting the fabricated ferromagnetic wire architecture to an out-of-plane clocking field allowed us to successfully propagate data from the input to the output.

Next, we interconnected three three-input majority logic gates with ferromagnetic and anti-ferromagnetic wire architectures to implement a seven-input majority logic architecture to realize the reliable computation ability of nano-magnetic devices. The nano-magnetic logic architecture was comprised of 38 single layer nano-magnetic devices that had dimensions of 100 *nm* x 50 *nm* x 10 *nm* and spaced 20 *nm* apart. We have captured MFM images of the seven-input majority

gate architecture computing the correct output. To this date this is the largest nano-magnetic logic architecture that has been fabricated and has no magnetic frustrations.

Even though we have observed error free operation in nano-magnetic logic architectures, it became evident that we needed better control over individual single layer nano-magnetic devices. To address this we have proposed a multilayer nano-magnetic device. The multilayer device has a bottom layer with perpendicular magnetization, a middle layer of non-magnetic conducting metal and top layer with in-plane magnetization. We have named this device a Spin Valve Based Nano-magnetic-logic (SVBN) device. MFM images of the top layers of the SVBN device reveal perfect magnetic alignment in the three-input majority logic gate and in the ferromagnetic and antiferro-magnetic wire architectures. Our future goal is to connect access transistors to the SVBN devices to convert magnetic signal to electrical signals and vice versa. With these hybrid devices, we achieved the possibility to use spin polarized current to write data on to the top layer and clock the top layer at the appropriate time to process information. By engineering the bottom layer of the output SVBN device to have a tilted magnetization, it allows us to read the device by giant magnetoresistance (GMR). With these hybrid devices we can achieve the final goal of reliable computation.

Finally, we have experimentally demonstrated a magnetic system that could be used to solve quadratic optimization problems that arise in computer vision applications. We fabricated a magnetic system that correspond to a real world image and demonstrated its computation capability. The magnetic system identified the salient features in the image with a true positive rate of 86%. This work was a proof of concept of the viability of using a magnetic system to solve a quadratic optimization problem. Our future goal is to use multilayer nano-magnetic devices that are connected to access transistors to implement a magnetic processor that could potentially solve any quadratic optimization problems.

List of References

[1] Multidimensional scaling. *Technometrics*, 45(2):182–182, 2003.

[2] International technology roadmap for semiconductor. 2012.

[3] M.T. Alam, S.J. Kurtz, M.A.J. Siddiq, M.T. Niemier, G.H. Bernstein, X.S. Hu, and W. Porod. On-chip clocking of nanomagnet logic lines and gates. *Nanotechnology, IEEE Transactions on*, 11(2):273 –286, march 2012.

[4] A. Amikam. *Introduction to Theory of Ferromagnetism*. Oxford Science Publication, 2000.

[5] B. Behin-Aein, A. Sarkar, and S. Datta. Modeling circuits with spins and magnets for all-spin logic. In *Solid-State Device Research Conference (ESSDERC), 2012 Proceedings of the European*, pages 36 –40, sept. 2012.

[6] G.H. Bernstein, A. Imre, V. Metlushko, A. Orlov, L. Zhou, L. Ji, G. Csaba, and W. Porod. Magnetic qca systems. *Microelectronics Journal*, 36(7):619 – 624, 2005.

[7] George I. Bourianoff, Paolo A. Gargini, and Dmitri E. Nikonov. Research directions in beyond cmos computing. *Solid-State Electronics*, 51:1426 – 1431, 2007.

[8] Y. Boykov, O. Veksler, and R. Zabih. Fast approximate energy minimization via graph cuts. *Pattern Analysis and Machine Intelligence, IEEE Transactions on*, 23(11):1222–1239, 2001.

[9] J. L. Bubendorff, E. Beaurepaire, C. Mény, P. Panissod, and J. P. Bucher. Perpendicular magnetization in ultrathin electrodeposited cobalt films. *Phys. Rev. B*, 56:R7120–R7128, Sep 1997.

[10] J. Canny. A computational approach to edge detection. *Pattern Analysis and Machine Intelligence, IEEE Transactions on*, (6):679–698, 1986.

[11] David B. Carlton, Nathan C. Emley, Eduard Tuchfeld, and Jeffrey Bokor. Simulation studies of nanomagnet-based logic architecture. *Nano Letters*, 8(12):4173–4178, 2008.

[12] R. Chau, J. Brask, S. Datta, G. Dewey, M. Doczy, B. Doyle, J. Kavalieros, B. Jin, M. Metz, A. Majumdar, and M. Radosavljevic. Emerging silicon and nonsilicon nanoelectronic devices: opportunities and challenges for future high-performance and low-power computational applications. In *VLSI Technology, 2005. (VLSI-TSA-Tech). 2005 IEEE VLSI-TSA International Symposium on*, pages 13 – 16, april 2005.

[13] R. Chau, S. Datta, M. Doczy, B. Doyle, B. Jin, J. Kavalieros, A. Majumdar, M. Metz, and M. Radosavljevic. Benchmarking nanotechnology for high-performance and low-power logic transistor applications. *Nanotechnology, IEEE Transactions on*, 4(2):153 – 158, march 2005.

[14] Yong Chen, Gun-Young Jung, Douglas A A Ohlberg, Xuema Li, Duncan R Stewart, Jan O Jeppesen, Kent A Nielsen, J Fraser Stoddart, and R Stanley Williams. Nanoscale molecular-switch crossbar circuits. *Nanotechnology*, 14(4):462, 2003.

[15] S.-B. Choe, Y. Acremann, A. Scholl, A. Bauer, A. Doran, J. Stahr, and H. A. Padmore. Vortex core-driven magnetization dynamics. *Science*, 304(5669):420–422, 2004.

[16] R. P. Cowburn, D. K. Koltsov, A. O. Adeyeye, M. E. Welland, and D. M. Tricker. Single-domain circular nanomagnets. *Phys. Rev. Lett.*, 83:1042–1045, Aug 1999.

[17] R. P. Cowburn and M. E. Welland. Room temperature magnetic quantum cellular automata. *Science*, 287(5457):1466–1468, 2000.

[18] G. Csaba. *Computing With Field-Coupled Nanomagnets*. PhD thesis, University of Notre Dame, 2003.

[19] G. H. O. Daalderop, P. J. Kelly, and F. J. A. den Broeder. Prediction and confirmation of perpendicular magnetic anisotropy in co/ni multilayers. *Phys. Rev. Lett.*, 68:682–685, Feb 1992.

[20] J. Das, S.M. Alam, and S. Bhanja. Ultra-low power hybrid cmos-magnetic logic architecture. *Circuits and Systems I: Regular Papers, IEEE Transactions on*, 59(9):2008 –2016, sept. 2012.

[21] K. Degawa, T. Aoki, T. Higuchi, H. Inokawa, and A. Takahashi. A single-electron-transistor logic gate family and its application - part i: basic components for binary, multiple-valued and mixed-mode logic. In *Multiple-Valued Logic, 2004. Proceedings. 34th International Symposium on*, pages 262 – 268, may 2004.

[22] B. Dieny. Giant magnetoresistance in spin-valve multilayers. *Journal of Magnetism and Magnetic Materials*, 136(3):335 – 359, 1994.

[23] M.E. Flatte. Spintronics. *Electron Devices, IEEE Transactions on*, 54(5):907 –920, may 2007.

[24] A. Forestier and M.R. Stan. Limits to voltage scaling from the low power perspective. In *Integrated Circuits and Systems Design, 2000. Proceedings. 13th Symposium on*, pages 365 –370, 2000.

[25] D.J. Frank, R.H. Dennard, E. Nowak, P.M. Solomon, Y. Taur, and Hon-Sum Philip Wong. Device scaling limits of si mosfets and their application dependencies. *Proceedings of the IEEE*, 89(3):259 –288, mar 2001.

[26] K. Galatsis, A. Khitun, R. Ostroumov, K.L. Wang, W.R. Dichtel, E. Plummer, J.F. Stoddart, J.I. Zink, Jae Young Lee, Ya-Hong Xie, and Ki Wook Kim. Alternate state variables for emerging nanoelectronic devices. *Nanotechnology, IEEE Transactions on*, 8(1):66 –75, jan. 2009.

[27] K.Yu. Guslienko. Magnetic anisotropy in two-dimensional dot arrays induced by magnetostatic interdot coupling. *Physics Letters A*, 278(5):293 – 298, 2001.

[28] M. Hanggi and L.O. Chua. A deterministic nonlinear-capacitor model for single-electron tunneling junctions. *Circuits and Systems I: Fundamental Theory and Applications, IEEE Transactions on*, 48(8):1019 –1022, aug 2001.

[29] N.Z. Haron and S. Hamdioui. Why is cmos scaling coming to an end? In *Design and Test Workshop, 2008. IDT 2008. 3rd International*, pages 98 –103, dec. 2008.

[30] N.Z. Haron, S. Hamdioui, and S. Cotofana. Emerging non-cmos nanoelectronic devices - what are they? In *Nano/Micro Engineered and Molecular Systems, 2009. NEMS 2009. 4th IEEE International Conference on*, pages 63 –68, jan. 2009.

[31] M. Haselman and S. Hauck. The future of integrated circuits: A survey of nanoelectronics. *Proceedings of the IEEE*, 98(1):11 –38, jan. 2010.

[32] James R. Heath. Molecular electronics. *Annual Review of Materials Research*, 39(1):1–23, 2009.

[33] James R. Heath, J. Fraser Stoddart, and R. Stanley Williams. More on molecular electronics. *Science*, 303(5661):1136–1137, 2004.

[34] K. Hess and G.J. Iafrate. Theory and applications of near ballistic transport in semiconductors. *Proceedings of the IEEE*, 76(5):519 –532, may 1988.

[35] A. Heuberger. X - ray lithography. *Journal of Vacuum Science Technology B: Microelectronics and Nanometer Structures*, 6(1):107 –121, jan 1988.

[36] J. Hoekstra. Towards a circuit theory for metallic single-electron tunnelling devices. *International Journal of Circuit Theory and Applications*, 35(3):213–238, 2007.

[37] H. Hoffmann and F. Steinbauer. Single domain and vortex state in ferromagnetic circular nanodots. *Journal of Applied Physics*, 92(9):5463–5467, 2002.

[38] Yu Huang, Xiangfeng Duan, Yi Cui, Lincoln J. Lauhon, Kyoung-Ha Kim, and Charles M. Lieber. Logic gates and computation from assembled nanowire building blocks. *Science*, 294(5545):1313–1317, 2001.

[39] J.A. Hutchby, G.I. Bourianoff, V.V. Zhirnov, and J.E. Brewer. Extending the road beyond cmos. *Circuits and Devices Magazine, IEEE*, 18(2):28 –41, mar 2002.

[40] A. Imre, G. Csaba, L. Ji, A. Orlov, G. H. Bernstein, and W. Porod. Majority logic gate for magnetic quantum-dot cellular automata. *Science*, 311(5758):205–208, 2006.

[41] Alexandra Imre, Csaba, Gary H Bernstein, Wolfgang Porod, and Vitali Metlushko. Investigation of shape-dependent switching of coupled nanomagnets. *Superlattices and Microstructures*, 34:513 – 518, 2003.

[42] Takashi Ito and Shinji Okazaki. Pushing the limits of lithography. *Nature*, 406(6799):1027–1031, 2000.

[43] P.-O. Jubert and R. Allenspach. Analytical approach to the single-domain-to-vortex transition in small magnetic disks. *Phys. Rev. B*, 70:144402, Oct 2004.

[44] D. K. Karunaratne and Sanjukta Bhanja. Study of single layer and multilayer nano-magnetic logic architectures. *Journal of Applied Physics*, 111(7):07A928, 2012.

[45] D. K. Karunaratne, J.F. Pulecio, and S. Bhanja. Driving magnetic cells for information storage and propagation. In *Nanotechnology Materials and Devices Conference (NMDC), 2010 IEEE*, pages 360–363, Oct.

[46] Cheol-Joo Kim, Jee-Eun Yang, Hyun-Seung Lee, Hyun M. Jang, Moon-Ho Jo, Won-Hwa Park, Zee Hwan Kim, and Sunglyul Maeng. Fabrication of si1-xgex alloy nanowire field-effect transistors. *Applied Physics Letters*, 91(3):033104 –033104–3, jul 2007.

[47] S.-J. Kim, Yu.I. Latyshev, and T. Yamashita. Single electron tunneling junctions using high-t/sub c/ superconducting materials. In *Magnetics Conference, 1999. Digest of INTERMAG 99. 1999 IEEE International*, page AP11, may 1999.

[48] S. Kirkpatrick, C. D. Gelatt, and M. P. Vecchi. Optimization by simulated annealing. *Science*, 220(4598):671–680, 1983.

[49] R.H. Klunder and J. Hoekstra. Programmable logic using a set electron box. In *Electronics, Circuits and Systems, 2001. ICECS 2001. The 8th IEEE International Conference on*, volume 1, pages 185 –188 vol.1, 2001.

[50] A. Kumari. *Design Issues in Magnetic Field Coupled Array: Clock Structure, Fabrication Defects and Dipolar Coupling*. PhD thesis, University of South Florida, 2010.

[51] Anita Kumari, Sudeep Sarkar, Javier F. Pulecio, D. K. Karunaratne, and Sanjukta Bhanja. Study of magnetization state transition in closely spaced nanomagnet two-dimensional array for computation. *Journal of Applied Physics*, 109(7):07E513, 2011.

[52] C. Lageweg, S. Cotofana, and S. Vassiliadis. Single electron encoded logic memory elements. In *Nanotechnology, 2003. IEEE-NANO 2003. 2003 Third IEEE Conference on*, volume 1, pages 449 – 452 vol.2, aug. 2003.

[53] C. Lageweg, S. Cotofana, and S. Vassiliadis. Single electron encoded latches and flip-flops. *Nanotechnology, IEEE Transactions on*, 3(2):237 – 248, june 2004.

[54] Brian Lambson, Zheng Gu, David Carlton, Scott Dhuey, Andreas Scholl, Andrew Doran, Anthony Young, and Jeffrey Bokor. Cascade-like signal propagation in chains of concave nanomagnets. *Applied Physics Letters*, 100(15):152406 –152406–4, apr 2012.

[55] J.A. Leavitt, P. Stoss, C.R. Edelman, R.E. Davis, S. Gutierrez, N.J. Jubb, and T.M. Reith. Permalloy stoichiometry by nuclear backscattering. *Nuclear Instruments and Methods in Physics Research Section B: Beam Interactions with Materials and Atoms*, (0):719 – 721, 1985.

[56] Larkhoon Leem and James S. Harris. Magnetic coupled spin-torque devices for nonvolatile logic applications. *Journal of Applied Physics*, 105(7):07D102, 2009.

[57] C S Lent, P D Tougaw, W Porod, and G H Bernstein. Quantum cellular automata. *Nanotechnology*, 4(1):49, 1993.

[58] A. Levin, A. Rav Acha, and D. Lischinski. Spectral matting. *Pattern Analysis and Machine Intelligence, IEEE Transactions on*, 30(10):1699 –1712, oct. 2008.

[59] Z. Li and S. Zhang. Magnetization dynamics with a spin-transfer torque. *Phys. Rev. B*, 68:024404, Jul 2003.

[60] M. Liu, M. Cai, and Y. Taur. Scaling limit of cmos supply voltage from noise margin considerations. In *Simulation of Semiconductor Processes and Devices, 2006 International Conference on*, pages 287 –289, sept. 2006.

[61] S. Liu, X. Hu, M. Niemier, J. NAHAS, G. Csaba, G. Bernstein, and W. Porod. Exploring the design of the magnetic-electrical interface for nanomagnet logic. *Nanotechnology, IEEE Transactions on*, PP(99):1, 2013.

[62] Shiliang Liu, X.S. Hu, J.J. Nahas, M.T. Niemier, W. Porod, and G.H. Bernstein. Electrical interface for nanomagnet logic. *Nanotechnology, IEEE Transactions on*, 10(4):757 –763, july 2011.

[63] A. Lyle, Xiaofeng Yao, F. Ebrahimi, J. Harms, and Jian-Ping Wang. Communication between magnetic tunnel junctions using spin-polarized current for logic applications. *Magnetics, IEEE Transactions on*, 46(6):2216 –2219, june 2010.

[64] Andrew Lyle, Jonathan Harms, Todd Klein, August Lentsch, Daniel Martens, Angeline Klemm, and Jian-Ping Wang. Spin transfer torque programming dipole coupled nanomagnet arrays. *Applied Physics Letters*, 100(1):012402 –012402–3, jan 2012.

[65] Andrew Lyle, Angeline Klemm, Jonathan Harms, Yisong Zhang, Hui Zhao, and Jian-Ping Wang. Probing dipole coupled nanomagnets using magnetoresistance read. *Applied Physics Letters*, 98(9):092502 –092502–3, feb 2011.

[66] J. Maciel and J.P. Costeira. A global solution to sparse correspondence problems. *Pattern Analysis and Machine Intelligence, IEEE Transactions on*, 25(2):187 – 199, feb 2003.

[67] J.I Mart, J Nogu, Kai Liu, J.L Vicent, and Ivan K Schuller. Ordered magnetic nanostructures: fabrication and properties. *Journal of Magnetism and Magnetic Materials*, 256:449 – 501, 2003.

[68] R. Martel, H.-S.P. Wong, K. Chan, and P. Avouris. Carbon nanotube field effect transistors for logic applications. In *Electron Devices Meeting, 2001. IEDM '01. Technical Digest. International*, pages 7.5.1 –7.5.4, 2001.

[69] Harden M. McConnell. Intramolecular charge transfer in aromatic free radicals. *The Journal of Chemical Physics*, 35(2):508–515, 1961.

[70] J. Mejia-Lopez, D. Altbir, A. H. Romero, X. Batlle, Igor V. Roshchin, Chang-Peng Li, and Ivan K. Schuller. Vortex state and effect of anisotropy in sub-100-nm magnetic nanodots. *Journal of Applied Physics*, 100(10):104319, 2006.

[71] N.N. Mojumder and K. Roy. Proposal for switching current reduction using reference layer with tilted magnetic anisotropy in magnetic tunnel junctions for spin-transfer torque (stt) mram. *Electron Devices, IEEE Transactions on*, 59(11):3054 –3060, nov. 2012.

[72] Wayne M. Moreau. *Semiconductor Lithography: Principles, Practices, and Materials (Microdevices)*. MICRODEVICES. Plenum Press, New York and London, August 1989.

[73] Ryoichi Nakatani, Hikaru Nomura, and Yasushi Endo. Magnetic logic devices composed of permalloy dots. *Journal of Physics: Conference Series*, 165(1):012030, 2009.

[74] R. Negishi, T. Hasegawa, K. Terabe, M. Aono, H. Tanaka, T. Ogawa, and H. Ozawa. I-v characteristics of single electron tunneling from symmetric and asymmetric double-barrier tunneling junctions. *Applied Physics Letters*, 90(22):223112 –223112–3, may 2007.

[75] A. Ng, M. Jordan, and Y. Weiss. On spectral clustering: Analysis and an algorithm, 2001.

[76] M. Niemier, X.S. Hu, A. Dingler, M.T. Alam, G. Bernstein, and W. Porod. Bridging the gap between nanomagnetic devices and circuits. In *Computer Design, 2008. ICCD 2008. IEEE International Conference on*, pages 506 –513, oct. 2008.

[77] M.T. Niemier and P.M. Kogge. Logic in wire: using quantum dots to implement a microprocessor. In *VLSI, 1999. Proceedings. Ninth Great Lakes Symposium on*, pages 118 –121, mar 1999.

[78] Hikaru Nomura and Ryoichi Nakatani. Nand/nor logical operation of a magnetic logic gate with canted clock-field. *Applied Physics Express*, 4(1):013004, 2011.

[79] E. J. Nowak. Maintaining the benefits of cmos scaling when scaling bogs down. *IBM Journal of Research and Development*, 46(2.3):169 –180, march 2002.

[80] Chan-Hoon Park, Sang-Hyun Lee, Ye-Ram Kim, Chang-Ki Baek, and Yoon-Ha Jeong. Fabrication and characterization of gate-all-around silicon nanowire field effect transistors. In *Nanotechnology (IEEE-NANO), 2011 11th IEEE Conference on*, pages 255 –259, aug. 2011.

[81] JinHyeong Park, Hongyuan Zha, and Rangachar Kasturi. Spectral clustering for robust motion segmentation, 2004.

[82] Stuart SP Parkin. Applications of magnetic nanostructures. *Spin Dependent Transport in Magnetic Nanostructures (Advances in Condensed Matter Science, vol. 3), London: Taylor & Francis*, pages 237–271, 2002.

[83] Scott Thompson Portland. Mos scaling: Transistor challenges for the 21st century, 1998.

[84] I L Prejbeanu, M Kerekes, R C Sousa, H Sibuet, O Redon, B Dieny, and J P Nozieres. Thermally assisted mram. *Journal of Physics: Condensed Matter*, 19(16):165218, 2007.

[85] J. Pulecio. *Field-Coupled Nano-Magnetic Logic Systems*. PhD thesis, University of South Florida, 2010.

[86] J. Pulecio, S. Bhanja, and S. Sarkar. An experimental demonstration of the viability of energy minimizing computing using nano-magnets. In *Nanotechnology (IEEE-NANO), 2011 11th IEEE Conference on*, pages 1038 –1042, aug. 2011.

[87] Javier F. Pulecio and Sanjukta Bhanja. Magnetic cellular automata coplanar cross wire systems. *Journal of Applied Physics*, 107(3):034308 –034308–5, feb 2010.

[88] J.F. Pulecio, P.K. Pendru, A. Kumari, and S. Bhanja. Magnetic cellular automata wire architectures. *Nanotechnology, IEEE Transactions on*, 10(6):1243 –1248, nov. 2011.

[89] H. Rahaman, B.K. Sikdar, and D.K. Das. Synthesis of symmetric functions using quantum cellular automata. In *Design and Test of Integrated Systems in Nanoscale Technology, 2006. DTIS 2006. International Conference on*, pages 119 –124, sept. 2006.

[90] S. Rajaram, D. K. Karunaratne, S. Sarkar, and S. Bhanja. Study of dipolar neighbor interaction on magnetization states of nano-magnetic disks.

[91] M. A. Reed, J. Chen, A. M. Rawlett, D. W. Price, and J. M. Tour. Molecular random access memory cell. *Applied Physics Letters*, 78(23):3735–3737, 2001.

[92] P. Santosh Kumar Karre, P.L. Bergstrom, M. Govind, and S.P. Karna. Single electron transistor fabrication using focused ion beam direct write technique. In *Advanced Semiconductor Manufacturing Conference, 2006. ASMC 2006. The 17th Annual SEMI/IEEE*, pages 221 – 224, may 2006.

[93] S. Sarkar and S. Bhanja. Synthesizing energy minimizing quantum-dot cellular automata circuits for vision computing. In *Nanotechnology, 2005. 5th IEEE Conference on*, pages 541 – 544 vol. 2, july 2005.

[94] S. Sarkar and S. Bhanja. Direct quadratic minimization using magnetic field-based computing. In *Design and Test of Nano Devices, Circuits and Systems, 2008 IEEE International Workshop on*, pages 31 –34, sept. 2008.

[95] S. Sarkar and K.L. Boyer. Perceptual organization in computer vision: A review and a proposal for a classificatory structure. *Systems, Man and Cybernetics, IEEE Transactions on*, 23(2):382–399, 1993.

[96] S. Sarkar and K.L. Boyer. *Computer perceptual organization in computer vision*, volume 12. World Scientific Pub Co Inc, 1994.

[97] S. Sarkar and P. Soundararajan. Supervised learning of large perceptual organization: graph spectral partitioning and learning automata. *Pattern Analysis and Machine Intelligence, IEEE Transactions on*, 22(5):504 –525, may 2000.

[98] Sudeep Sarkar. An introduction to perceptual organization. In *Integration of Knowledge Intensive Multi-Agent Systems, 2003. International Conference on*, pages 330 – 335, sept.-4 oct. 2003.

[99] W Scholz, K.Yu Guslienko, V Novosad, D Suess, T Schrefl, R.W Chantrell, and J Fidler. Transition from single-domain to vortex state in soft magnetic cylindrical nanodots. *Journal of Magnetism and Magnetic Materials*, 266, 2003.

[100] Robert F. Service. Next-generation technology hits an early midlife crisis. *Science*, 302(5645):556–559, 2003.

[101] Jianbo Shi and J. Malik. Normalized cuts and image segmentation. *Pattern Analysis and Machine Intelligence, IEEE Transactions on*, 22(8):888 –905, aug 2000.

[102] T. Shinjo, T. Okuno, R. Hassdorf, K. Shigeto, and T. Ono. Magnetic vortex core observation in circular dots of permalloy. *Science*, 289(5481):930–932, 2000.

[103] Gregory Snider, Alexei Orlov, Islamshah Amlani, Gary Bernstein, Craig Lent, James Merz, and Wolfgang Porod. Quantum-dot cellular automata: Line and majority logic gate. *Jpn J Appl Phys*, 38(12):7227–7229, dec 1999.

[104] N. Spaldin. *Magnetic Materials : Fundamentals and Applications*. Cambridge University Press, 2010.

[105] J. Stöhr and H. C. Siegmann. *Magnetism: From Fundamentals to Nanoscale Dynamics*, volume 152 of *Springer Series in Solid-State Physics*. Berlin: Springer, 2006.

[106] S.G. Tan, M.B.A. Jalil, Thomas Liew, K.L. Teo, G.H. Lai, and T.C. Chong. Magnetoelectric spin-fet for memory, logic, and amplifier applications. *Journal of Superconductivity*, 18:357–365, 2005.

[107] D. Thuau, V. Koutsos, and R. Cheung. Electrical and mechanical properties of carbon nanotube-polyimide composites. *Journal of Vacuum Science Technology B: Microelectronics and Nanometer Structures*, 27(6):3139 –3144, nov 2009.

[108] Ching Tsang, R.E. Fontana, Tsann Lin, D.E. Heim, V.S. Speriosu, B.A. Gurney, and M.L. Williams. Design, fabrication and testing of spin-valve read heads for high density recording. *Magnetics, IEEE Transactions on*, 30(6):3801 –3806, nov 1994.

[109] S. Tyagi. Moore's law: A cmos scaling perspective. In *Physical and Failure Analysis of Integrated Circuits, 2007. IPFA 2007. 14th International Symposium on the*, pages 10 –15, july 2007.

[110] S. Umeyama. An eigendecomposition approach to weighted graph matching problems. *Pattern Analysis and Machine Intelligence, IEEE Transactions on*, 10(5):695 –703, sep 1988.

[111] E. Varga, A. Orlov, M.T. Niemier, X.S. Hu, G.H. Bernstein, and W. Porod. Experimental demonstration of fanout for nanomagnetic logic. *Nanotechnology, IEEE Transactions on*, 9(6):668 –670, nov. 2010.

[112] C. Vieu, F. Carcenac, A. Pepin, Y. Chen, M. Mejias, A. Lebib, L. Manin-Ferlazzo, L. Couraud, and H. Launois. Electron beam lithography: resolution limits and applications. *Applied Surface Science*, 164(1-4):111 – 117, 2000.

[113] A. Wachowiak, J. Wiebe, M. Bode, O. Pietzsch, M. Morgenstern, and R. Wiesendanger. Direct observation of internal spin structure of magnetic vortex cores. *Science*, 298(5593):577–580, 2002.

[114] Xiaobin Wang, Yiran Chen, Hai Li, D. Dimitrov, and H. Liu. Spin torque random access memory down to 22 nm technology. *Magnetics, IEEE Transactions on*, 44(11):2479 –2482, nov. 2008.

[115] Yangyuan Wang, Ruqi Han, Xiaoyan Liu, and Jinfeng Kang. The challenges for physical limitations in si microelectronics. In *Solid-State and Integrated Circuit Technology, 1998. Proceedings. 1998 5th International Conference on*, pages 25 –30, 1998.

[116] F. Watt, A. Bettiol, J Vankan, A Teo, and M Breese. Ion beam lithography and nanofabrication: A review. *Journal of Vacuum Science Technology B: Microelectronics and Nanometer Structures*, 4(3):269 –286, june 2004.

[117] B. Q. Wei, R. Vajtai, and P. M. Ajayan. Reliability and current carrying capacity of carbon nanotubes. *Applied Physics Letters*, 79(8):1172 –1174, aug 2001.

[118] D. Weller, H. Brandle, G. Gorman, C.J. Lin, and H. Notarys. Magnetic and magneto x2010;optical properties of cobalt x2010;platinum alloys with perpendicular magnetic anisotropy. *Applied Physics Letters*, 61(22):2726 –2728, nov 1992.

[119] Robert M. White. The magnetic hamiltonian. In *Quantum Theory of Magnetism*, volume 32 of *Springer Series in Solid-State Sciences*, pages 33–83. Springer Berlin Heidelberg, 2007.

[120] H.-S.P. Wong, J. Appenzeller, V. Derycke, R. Martel, S. Wind, and P. Avouris. Carbon nanotube field effect transistors - fabrication, device physics, and circuit implications. In *Solid-State Circuits Conference, 2003. Digest of Technical Papers. ISSCC. 2003 IEEE International*, pages 370 – 500 vol.1, 2003.

[121] Shazia Yasin, D. G. Hasko, and H. Ahmed. Fabrication of [less-than] 5 nm width lines in poly(methylmethacrylate) resist using a water:isopropyl alcohol developer and ultrasonically-assisted development. *Applied Physics Letters*, 78(18):2760–2762, 2001.

[122] Shazia Yasin, D.G. Hasko, and H. Ahmed. Comparison of mibk/ipa and water/ipa as pmma developers for electron beam nanolithography. *Microelectronic Engineering*, (0):745 – 753, 2002.

[123] B. Yu and M. Meyyappan. Nanotechnology: Role in emerging nanoelectronics. *Solid-State Electronics*, 50(4):536 – 544, 2006.

[124] V.V. Zhirnov, J.A. Hutchby, G.I. Bourianoffls, and J.E. Brewer. Emerging research logic devices. *Circuits and Devices Magazine, IEEE*, 21(3):37 – 46, may-june 2005.

[125] Zhaohui Zhong, Nathaniel M Gabor, Jay E Sharping, Alexander L Gaeta, and Paul L McEuen. Terahertz time-domain measurement of ballistic electron resonance in a single-walled carbon nanotube. *Nature Nanotechnology*, 3(4):201–205, 2008.

[126] Xiaobin Zhu. *Magnetic Fource Microscopy Studies of Submicon and Nanoscale Magnet Arrays*. PhD thesis, University of McGill, 2002.

Appendices

Appendix A: Copyright and Permissions

Title:	Driving magnetic cells for information storage and propagation
Conference Proceedings:	Nanotechnology Materials and Devices Conference (NMDC), 2010 IEEE
Author:	Karunaratne, D. K.; Pulecio, Javier F.; Bhanja, Sanjukta
Publisher:	IEEE
Date:	12-15 Oct. 2010

Logged in as:
Dinuka Karunaratne
Account #:
3000505609

LOGOUT

Thesis / Dissertation Reuse

The IEEE does not require individuals working on a thesis to obtain a formal reuse license, however, you may print out this statement to be used as a permission grant:

Requirements to be followed when using any portion (e.g., figure, graph, table, or textual material) of an IEEE copyrighted paper in a thesis:

1) In the case of textual material (e.g., using short quotes or referring to the work within these papers) users must give full credit to the original source (author, paper, publication) followed by the IEEE copyright line © 2011 IEEE.
2) In the case of illustrations or tabular material, we require that the copyright line © [Year of original publication] IEEE appear prominently with each reprinted figure and/or table.
3) If a substantial portion of the original paper is to be used, and if you are not the senior author, also obtain the senior author's approval.

Requirements to be followed when using an entire IEEE copyrighted paper in a thesis:

1) The following IEEE copyright/ credit notice should be placed prominently in the references: © [year of original publication] IEEE. Reprinted, with permission, from [author names, paper title, IEEE publication title, and month/year of publication]
2) Only the accepted version of an IEEE copyrighted paper can be used when posting the paper or your thesis on-line.
3) In placing the thesis on the author's university website, please display the following message in a prominent place on the website: In reference to IEEE copyrighted material which is used with permission in this thesis, the IEEE does not endorse any of [university/educational entity's name goes here]'s products or services. Internal or personal use of this material is permitted. If interested in reprinting/republishing IEEE copyrighted material for advertising or promotional purposes or for creating new collective works for resale or redistribution, please go to http://www.ieee.org/publications_standards/publications/rights/rights_link.html to learn how to obtain a License from RightsLink.

If applicable, University Microfilms and/or ProQuest Library, or the Archives of Canada may supply single copies of the dissertation.

BACK CLOSE WINDOW

Appendix A: (continued)

AMERICAN INSTITUTE OF PHYSICS LICENSE TERMS AND CONDITIONS

Mar 15, 2013

All payments must be made in full to CCC. For payment instructions, please see information listed at the bottom of this form.

License Number	3110290838747
Order Date	Mar 15, 2013
Publisher	American Institute of Physics
Publication	Journal of Applied Physics
Article Title	Study of single layer and multilayer nano-magnetic logic architectures
Author	D. K. Karunaratne, Sanjukta Bhanja
Online Publication Date	Mar 2, 2012
Volume number	111
Issue number	7
Type of Use	Thesis/Dissertation
Requestor type	Author (original article)
Format	Print and electronic
Portion	Figure/Table
Number of figures/tables	4
Title of your thesis / dissertation	NANO-MAGNETIC DEVICES FOR COMPUTATION
Expected completion date	May 2013
Estimated size (number of pages)	130
Total	0.00 USD
Terms and Conditions	

American Institute of Physics -- Terms and Conditions: Permissions Uses

American Institute of Physics ("AIP") hereby grants to you the non-exclusive right and license to use and/or distribute the Material according to the use specified in your order, on a one-time basis, for the specified term, with a maximum distribution equal to the number that you have ordered. Any links or other content accompanying the Material are not the subject of this license.

1. You agree to include the following copyright and permission notice with the reproduction of the Material: "Reprinted with permission from [FULL CITATION]. Copyright [PUBLICATION YEAR], American Institute of Physics." For an article, the copyright and permission notice must be printed on the first page of the article or book chapter. For photographs, covers, or tables, the copyright and permission notice may appear with the Material, in a footnote, or in the reference list.
2. If you have licensed reuse of a figure, photograph, cover, or table, it is your responsibility to ensure that the material is original to AIP and does not contain the copyright of another entity, and that the copyright notice of the figure, photograph, cover, or table does not indicate that it was reprinted by AIP, with permission, from another source. Under no circumstances does AIP, purport or intend to grant permission to reuse material to which it does not hold copyright.
3. You may not alter or modify the Material in any manner. You may translate the

Appendix A: (continued)

Material into another language only if you have licensed translation rights. You may not use the Material for promotional purposes. AIP reserves all rights not specifically granted herein.

4. The foregoing license shall not take effect unless and until AIP or its agent, Copyright Clearance Center, receives the Payment in accordance with Copyright Clearance Center Billing and Payment Terms and Conditions, which are incorporated herein by reference.
5. AIP or the Copyright Clearance Center may, within two business days of granting this license, revoke the license for any reason whatsoever, with a full refund payable to you. Should you violate the terms of this license at any time, AIP, American Institute of Physics, or Copyright Clearance Center may revoke the license with no refund to you. Notice of such revocation will be made using the contact information provided by you. Failure to receive such notice will not nullify the revocation.
6. AIP makes no representations or warranties with respect to the Material. You agree to indemnify and hold harmless AIP, American Institute of Physics, and their officers, directors, employees or agents from and against any and all claims arising out of your use of the Material other than as specifically authorized herein.
7. The permission granted herein is personal to you and is not transferable or assignable without the prior written permission of AIP. This license may not be amended except in a writing signed by the party to be charged.
8. If purchase orders, acknowledgments or check endorsements are issued on any forms containing terms and conditions which are inconsistent with these provisions, such inconsistent terms and conditions shall be of no force and effect. This document, including the CCC Billing and Payment Terms and Conditions, shall be the entire agreement between the parties relating to the subject matter hereof.

This Agreement shall be governed by and construed in accordance with the laws of the State of New York. Both parties hereby submit to the jurisdiction of the courts of New York County for purposes of resolving any disputes that may arise hereunder.

If you would like to pay for this license now, please remit this license along with your payment made payable to "COPYRIGHT CLEARANCE CENTER" otherwise you will be invoiced within 48 hours of the license date. Payment should be in the form of a check or money order referencing your account number and this invoice number RLNK500978348.
Once you receive your invoice for this order, you may pay your invoice by credit card. Please follow instructions provided at that time.

Make Payment To:
Copyright Clearance Center
Dept 001
P.O. Box 843006
Boston, MA 02284-3006

For suggestions or comments regarding this order, contact RightsLink Customer Support: customercare@copyright.com or +1-877-622-5543 (toll free in the US) or +1-978-646-2777.

Gratis licenses (referencing $0 in the Total field) are free. Please retain this printable license for your reference. No payment is required.

About the Author

D. K. Karunaratne received his Bachelor of the Science of Engineering in Electrical and Electronic Engineering from University of Peradeniya, Sri Lanka, in 2007. He received his Master of Science in Electrical Engineering from University of South Florida, USA, in 2012. Currently he is pursuing his Ph.D. degree in Electrical Engineering at University of South Florida, U.S.A. His research interests are in emerging computational devices.